POLYTECHNIC UNIVERSITY OF TURIN

Master's Degree in Aerospace Engineering

Politecnico di Torino

LUND UNIVERSITY

Master's Degree Thesis

Numerical Investigation of the HIFiRE 2 Combustion Chamber

Supervisors

Prof. Christer FUREBY

Prof. Nicole VIOLA

Dr. Thommie NILSSON

Candidate

Alessandro ERCOLE

July 2022

Politecnico di Torino

LUND UNIVERSITY

Master's Thesis
Master's Degree Program in Aerospace Engineering

Numerical Investigation of the HIFiRE 2 Combustion Chamber

By

Alessandro Ercole
******

Supervisor(s):
Prof. Christer Fureby, Supervisor
Prof. Nicole Viola, Supervisor
Dr. Thommie Nilsson, Co-Supervisor

Politecnico di Torino
2022

Declaration

I hereby declare that, the contents and organization of this thesis constitute my own original work and does not compromise in any way the rights of third parties, including those relating to the security of personal data.

Alessandro Ercole
2022

* This thesis is presented in partial fulfillment of the requirements for **M.Sc. Degree** in Aerospace Engineering at Politecnico di Torino.

I would like to dedicate this thesis to all my friends and family, for all the support and encouragement they gave me during this fascinating journey of life.

Acknowledgements

I want to sincerely thank my supervisor, Prof. Christer Fureby, for guiding me through this work; I am extremely grateful for the insightful and inspiring discussions, which are mostly reflected in the content. I am also extremely grateful for all the computational resources that were provided to me through the Swedish National Infrastructure for Computing, without which this work would not have seen the light.

I also want to thank everyone at the Department of Energy Sciences of Lund University for setting the ideal work environment for me. I was welcomed with a warmth that surpassed my most optimistic expectations, and I've got to know many wonderful people there. It has been an unforgettable experience.

I am much obliged to Prof. Nicole Viola for the exciting opportunity she gave me in working on my Master's Thesis abroad. Without her, none of this would have been possible.

Last but not least, a big "Thank You!" to my friends and family for supporting me unconditionally.

Abstract

The study focuses on high-fidelity numerical simulations of several operating modes of the HIFiRE 2 Direct Connect Rig (HDCR) facility experiment. Wall Modeled Large Eddy Simulations of supersonic combustion have been performed to analyze the main flow features and compare wall pressure distributions with the experimental data. The combustion model is based upon finite-rate chemistry, with the Arrhenius-based closure provided by an ethylene-air skeletal reaction mechanism. A monotonicity-preserving flux reconstruction scheme based on central differencing and flux limiters was implemented in the solver, which has been previously written using the open-source CFD toolbox OpenFOAM®. The governing equations were discretized and solved on a hexahedral structured grid, using explicit time integration and parallel computing. The modeling strategy has been carefully validated in many other studies. Results from the simulations are compared with the experimental results, showing poor agreement. Insufficient burning, delayed combustion, and different flow features have been observed. This fact is supposed to be related to the very large experimental uncertainties about key features of the experimental setup, such as the wind tunnel supersonic nozzle geometry, the target mass flow rate, and the air composition of the Arc-Heated Scramjet Test Facility. However, the flowfield data have been qualitatively analyzed to elucidate the complexity of the physical phenomena involved.

Contents

List of Figures

List of Tables

Nomenclature

Roman Symbols

$\Delta h_{f,k}^{0,m}$ Molar enthalpy of formation of specie k, with reference to the standard conditions

$\dot{\omega}_k$ Net rate of production/consumption of specie k

$\dot{m}_f$ Fuel mass flow rate

$\dot{Q}_c$ Volumetric heat release due to chemical reactions.

$\dot{q}_{kj}$ Rate of change of specie k in reaction j

$\mathbf{b_E}$ Subgrid energy flux

$\mathbf{b_k}$ Subgrid mass flux of specie k

$\mathbf{B}$ Subgrid stress tensor

$\mathbf{D}$ Deviatoric component of the strain tensor

$\mathbf{E}$ Strain tensor

$\mathbf{f_e}$ External, specific forces acting on the fluid element

$\mathbf{J_k}$ Mass diffusion vector field

$\mathbf{q}$ Thermal flux vector

$\mathbf{q}_\alpha$ Thermal flux due to molecular diffusion (Fourier)

$\mathbf{q}_{rad}$ Radiative thermal flux

$\mathscr{M}_k$ Molecular weight of specie k

$\mathbf{S}$	Stress tensor
τ_{ig}	Time of ignition delay
$\mathbf{u}$	Velocity vector
A_s,T_s	Sutherland's coefficients
C	Progress variable
c_p	Constant pressure specific heat
c_v	Constant volume specific heat
C_{M_k}	Molar concentration of chemical specie k
Co	Courant number
D_k	Diffusion coefficient of specie k
Da	Damkhöler number
e	Specific internal energy
F	Thrust force
g	Gravity of Earth at sea level
G_{FO}	Takeno flame index
H	Specific total enthalpy
h	Specific enthalpy
I_{sp}	Specific impulse
k	Thermal conductivity
k	Turbulent kinetic energy
k_f	Specific reaction rate constant
k_v	Bulk viscosity coefficient
Ka	Karlovitz number

Kn Knudsen number

L Macroscopic scale, combustion chamber characteristic length

Le Lewis number

M Mach number

Pr Prandtl number

R_u Universal gas constant

S_u Laminar flame speed

Sc Schmidt number

T Temperature

T_a Temperature of activation

V Control volume

W_j Atomic weight of element j

Y_k Mass fraction of specie k

Z Mixture fraction

N Mesh refinement parameter

Greek Symbols

α Thermal diffusivity

χ Scalar dissipation rate

Δ Finite volume characteristic length

γ Ratio of the specific heats

Γ_ϕ Generic diffusion coefficient of quantity ϕ

λ Free mean molecular path

μ Dynamic viscosity

ν Kinematic viscosity (momentum diffusivity)

ν_k Eddy kinematic viscosity

ν_{kj} Stoichiometric coefficient of specie k in reaction j

ρ Density

Υ Takeno indexed heat release

Subscripts

0 Reference conditions

k Relative to the k-th specie

st Stoichiometric condition

t Turbulent, related to turbulence modeling

Other Symbols

$\otimes$ Tensor product

Acronyms / Abbreviations

AFRL Air Force Research Laboratory

AFT Adiabatic Flame Temperature

CCP Combined Cycle Propulsion

DAE Discretized Algebraic Equations

DMR Dual Mode Ramjet

DNS Direct Numerical Simulations

DSTO Defence Science and Technology Organization

FVM Finite Volume Method

HAP Hypersonic Airbreathing Propulsion

HIFiRE Hypersonic International Flight Research Experiment

ISA International Standard Atmosphere

JANNAF Joint Army Navy NASA Air Force

LES Large Eddies Simulations

MUSCL Monotonic Upstream-Centered Scheme for Conservation Laws

PDE Partial Differential Equation

RANS Reynolds-Averaged Navier-Stokes

RBCC Rocket-Based Combined Cycles

TBCC Turbine-Based Combined Cycles

TPS Thermal Protection System

TVD Total Variation Diminishing

Chapter 1

Introduction to the Thesis Topic

The content of this chapter is intended to briefly introduce the topic of hypersonic flight and the related challenges, focusing in particular on hypersonic airbreathing propulsion. The chapter then ends with the declaration of the scope of the work.

1.1 The First Steps

The history of aviation - and science and technology in general - has been characterized by two, inherently human words: *dream* and *challenge*. The atavistic dream of flying, of getting closer to whatever our ancestors used to believe was up there, has been part of *us* since the beginning of civilization. A clear clue about this is the Greek myth of Icarus, the son of Daedalus. The latter, an outstandingly ingenious inventor, was condemned, along with his son, to live the rest of his life in the maze he had created at the request of Minos, king of Crete; he and his son got trapped in the abstraction of his mind, unable to escape. However, the dream of freedom always finds a way: if they could not find their way out with their feet on the ground, they could fly away. This is where the challenge is: build a pair of wings made of wax and feathers and be aware of how likely the sky is to become a hostile environment. The challenge ultimately overwhelmed Icarus, unable to control his desire to fly higher, closer to the Sun: this is probably the first structural failure related to an inadequate TPS to ever be reported. What this story can teach us in the context of hypersonic flight is a question whose answer is left open. Nevertheless, one thing is for sure: the challenges of hypersonic flight are many and, unfortunately, the technological level

of our society is by far insufficient to achieve most of them. On the other hand, the interest in this flight regime is going through a new wave of reinforcement, with new opportunities for space access, civil aviation, and defense applications.

Metaphorically speaking, the day designers began to become interested in the hypersonic regime represented a step into completely new lands; lands that used to be, and still are, home of many unknowns. A systematic, and potentially beneficial, way of dealing with such uncertainty in the context of hypersonic flight has been described by John J. Bertin (author of *Hypersonic Aerothermodynamics*, 1994, AIAA) and Russel M. Cummings, in a 2003 review article about the latest fifty years of hypersonic disciplines and their prospects [2]. This framework, developed by Matsch and McMasters, identifies four main domains of science and technology using two parameters: *knowledge* and *awareness*. Figure 1.1 summarizes the different opportunities for research teams and designers moving their steps into hypersonic research.

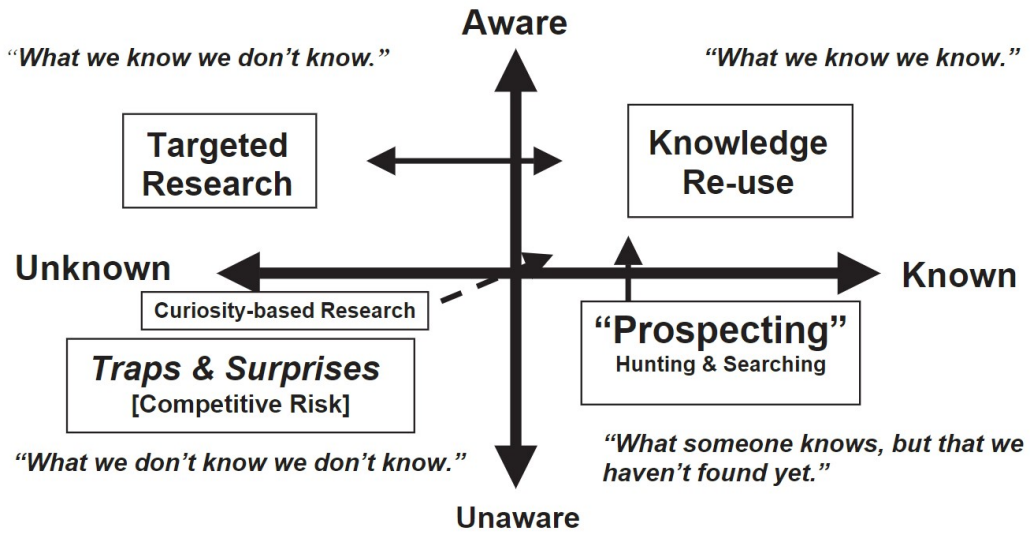

Fig. 1.1 Knowledge Management Domain, reported in [2]. Most of the challenges related to hypersonic flight, from external aerothermodynamics to hypersonic airbreathing propulsion, involve the two upper quadrants of the domain.

Since the times of the first conceptual designs of Winged Re-entry Vehicles (WRV), Hypersonic Cruise Vehicles (HCV), and air-breathing Single-Stage-To-Orbit (SSTO) vehicles, designers have had crystal clear that there were, and still, there are many things "we know we don't know". This kind of uncertainty, lying

in the upper-left quadrant of Figure 1.1, is typically faced with targeted research programs once the key technology concept has emerged. As an example, we can think about the problem of hypersonic airbreathing propulsion: once the ramjet-based engine has been identified as a key technology, research programs like NASA's HRE (Hypersonic Ramjet Experiment, see [3] for further details) were born in the mid-1960s.

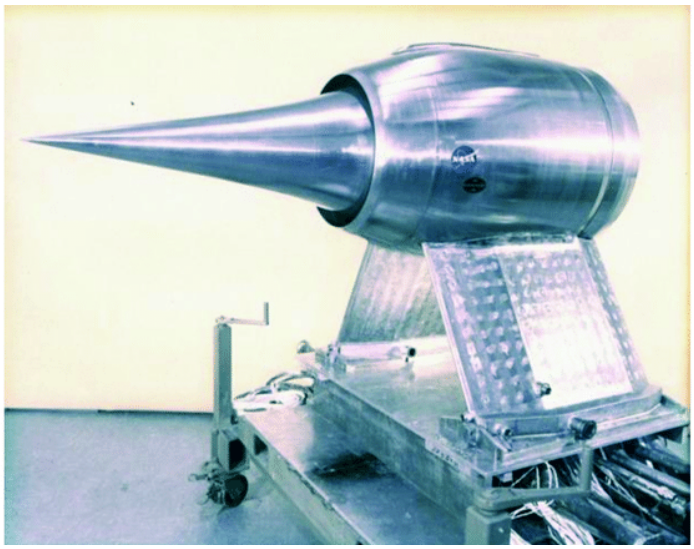

Fig. 1.2 Pre-test model of the Hypersonic Ramjet Experiment, reported in reference [3]. The goal of the project was to explore the concept of the scramjet propulsive system, using wind-tunnel as well as flight tests with the engine mounted on a modified version of the X-15 vehicle.

The HRE project started with the aim of providing useful insights into the physics of combustion in subsonic-supersonic flows using both wind-tunnel and flight testing and focusing on multiple research areas such as aerothermodynamics, and structures and materials. Although the program partially fulfilled some of the objectives and many lessons were learned, the cancellation of the X-15 program in 1968 didn't make it possible to effectively test-fly the engine. In addition to that, an unexpected shock-shock interaction - resulting in severe damage to the vehicle's structure - had been observed during an X-15A2 flight, when carrying a dummy model of the HRE in podded configuration. This was interpreted as a "warning" that things would have been even more difficult than initially thought. About the program, whose technical memorandum is available online [4], Richard P. Hallion wrote:

> "This project, the hypersonic ramjet experiment, cost $50 million, and generated only one noteworthy accomplishment: 'the illumination of critical unknowns', as author John V. Becker writes."

Adding then:

> "It is a graphic example of what happens when an immature technology is pushed too fast too soon, in the absence of comprehensive thought and planning and with zeal replacing insight."

In Hallion's point of view, the HRE program had been insidiously undermined by "unknown unknowns" (the lower-left quadrant of Figure 1.1), and this led to a fate similar to Icarus' one in the popular myth. However, research on hypersonic flight and hypersonic airbreathing propulsion kept going both inside and outside the United States, although with alternate waves of excitement and program cancellations.

During the 1980s, the motivation of focusing all the previously acquired knowledge on the novel National Aerospace Plane Program (NASP) grew stronger. The X-30, a demonstrator concept born under the NASP's aegis during the Reagan presidency, was expected to adopt both scramjet and rocket propulsion to access space with a reusable SSTO vehicle; the horizontal take-off and landing capabilities would have increased operational flexibility beyond the limits of the newborn Space Shuttle STS, giving the USA a giant strategic advantage in space access over the USSR. Figure 1.3 represents the vehicle in an artist's conception. Although the vehicle never reached the prototype stage and funding stopped in 1994, the program's output turned out to be a remarkable step ahead in many areas of research and proved itself crucial in the success of later projects. Among such areas of research, ranging from materials and structures to new concepts of combined-cycle propulsion systems, Corin Segal in [5] reports that, perhaps, the most significant achievements were those in the development of effective predictive tools in the area of **computational fluid dynamics**, with applications to both external aerodynamics and internal flows with chemical reactions. Nowadays, with the increasing availability of computational power, design teams have the opportunity to efficiently take advantage of those tools from the very first phases of the multidisciplinary design process.

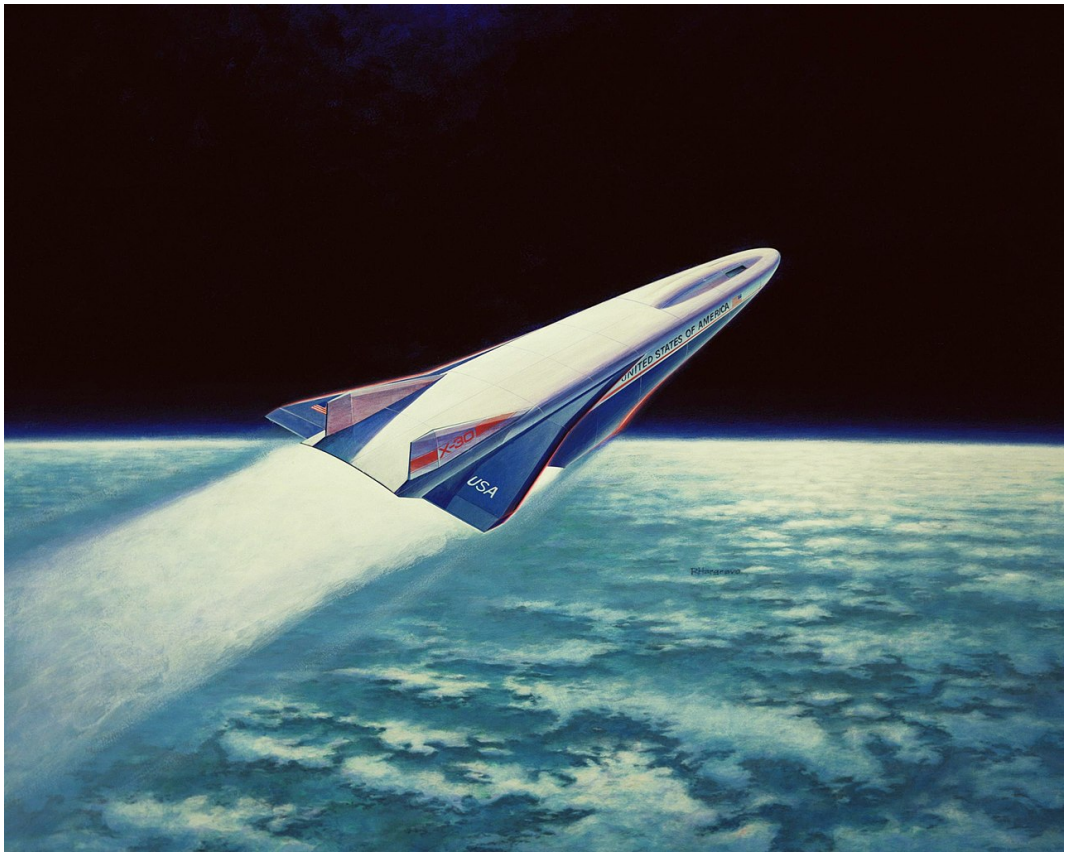

Fig. 1.3 Artist's concept of the Rockwell X-30 aerospace plane flying through Earth's atmosphere on its way to low-Earth orbit. Credits: James Schultz, 75th Anniversary NASA publication.

Since the cancellation of the National Aero-Space Plane program in 1994, interest and progress in hypersonic flight and propulsion have, nonetheless, never stopped. Several programs, even outside the United States, have achieved remarkable results in the field of HAP and other key technologies. Corin Segal in the introduction of his book *The Scramjet Engine: Processes and Characteristics* [5], reports the most important ones, along with several additional references.

From a different point of view, an indicator of how much stake the research community has in the issue is given by the trend of Figure 1.4. It shows the number of results containing the keyword "scramjet engine", from the Google Scholar search engine, up to the year 2020. The inflationary trend, with the number of publications almost doubling every decade, is reminiscent of the ones observed in many other key areas of research, e.g. Artificial Intelligence. Although the comparison between areas of research so far in context and width of applicability is far from being legit,

the writer hopes that projecting this trend in the future, the increasing collective effort will lead to the necessary technological maturity of these propulsive systems, ultimately bringing space closer, and making the world a smaller place.

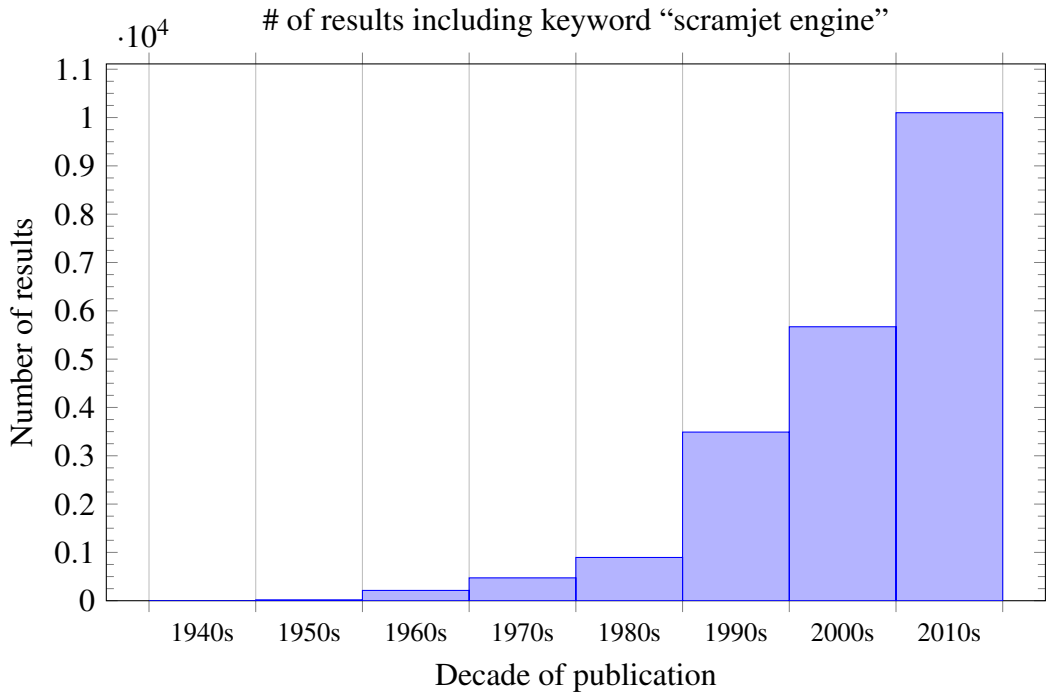

Fig. 1.4 Publications including keyword “scramjet engine”, grouped per decade. The increasing interest in the topic of hypersonic airbreathing propulsion, and in particular about the scramjet technology, is unmistakable. Data collected April 2022.

1.2 Challenges of Hypersonic Flight

Before we focus on hypersonic vehicles and their propulsive systems, it is useful to identify the framework in which these vehicles have been conceptualized, designed, and, in some rare cases, built. The so-called *hypersonic regime* eludes a universal definition, and there is not a conventional demarcation line between supersonic and hypersonic like the one, for instance, delimiting the subsonic and the supersonic regime. We can state, however, that in a flow characterized by a Mach number around five, the emergence of some peculiar flow features requires a completely different approach to the design problem. For instance, in the external flow, some examples of these peculiarities are: the shockwave coming close to the surface (*thin shock layer*);

the presence of regions of strong entropy gradients and vorticity (*entropy layer*) in the boundary layer region, interacting and complicating the analysis; *viscous interaction* between the kinematic and thermal boundary layers; other effects of high temperature flows such as *extreme thermal loads and heat transfer*, *chemical activity*, *vibrational non-equilibrium*, *dissociation*. An overview of these effects is given in Figure 1.5. A far-reaching point: although the aforementioned physical phenomena mainly influence external aerodynamics, the remarkable engine-airframe integration of hypersonic vehicles - an *unicum* among all the classes of aircraft - makes them relevant and minding-worth also in the context of propulsion system design. For the interested reader, reference [6] reports a quick, didactic introduction to the features of hypersonic flows, still keeping a readable and top-level approach. The same author, John D. Anderson, dedicated another work, reference [7], entirely to the topic of hypersonic flow and high-temperature gas dynamics. There, the peculiar features introduced in the first reference are investigated in deeper detail.

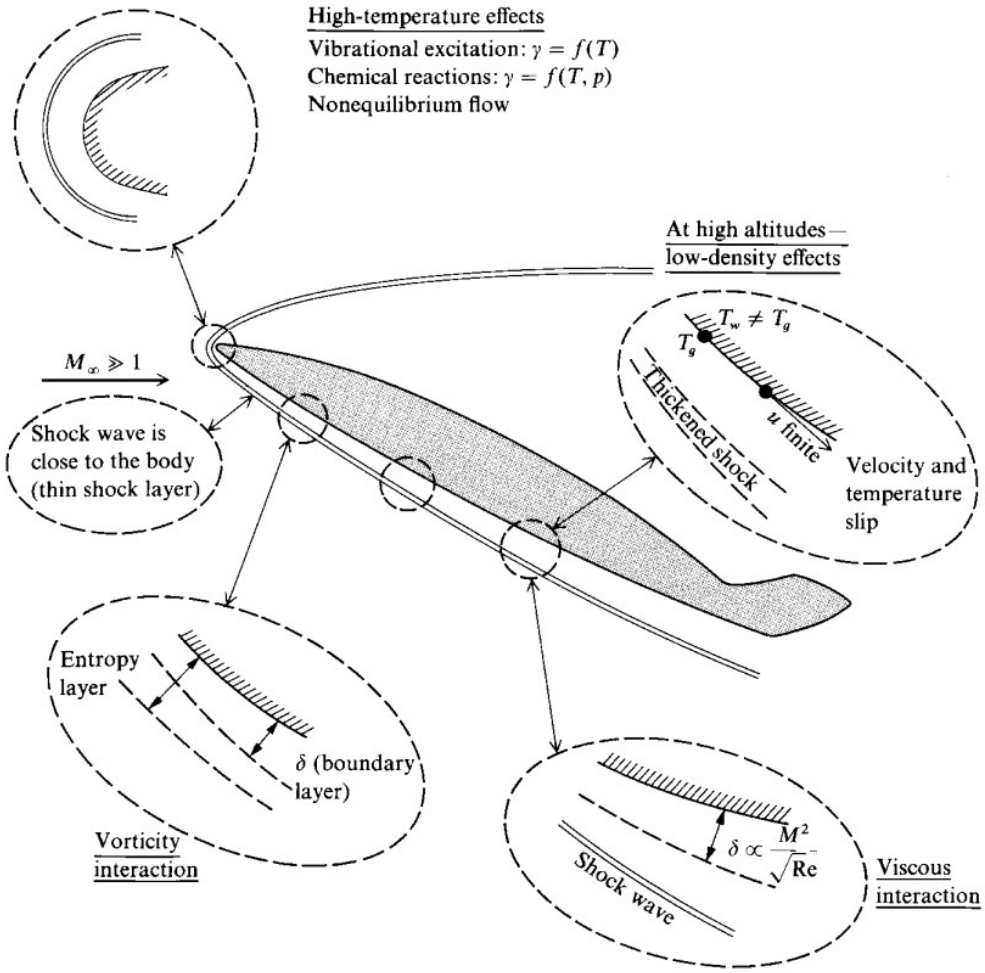

Fig. 1.5 Some of the physical phenomena which characterize the hypersonic regime. Image from [7].

1.2.1 The STRATOFLY MR3 Hypersonic Cruiser Concept

To seek a better understanding of how flying in the hypersonic regime thoroughly influences the vehicle's design, we can look at Figure 1.6. There represented is the STRATOFLY MR3 Hypersonic Cruiser, the outcome of an EU-funded research project whose primary objective was to elaborate the conceptual design of a civil transport aircraft expected to reach TRL 6 [1] by 2035; a further output of the project

[1] Technology Readiness Level 6: models (full scale) demonstration in a relevant environment. See [8] for the complete scale.

was the establishment of a design framework capable of accounting for the wide spectrum of requisites from multiple disciplines.

Fig. 1.6 Conceptual representation of the STRATOFLY MR3 Hypersonic Cruiser, the outcome of the H2020 STRATOFLY Project funded by the European Commission. Credits: [9]

The MR3 is a good example of how high-speed aerothermodynamics and the distinctive operational landscape produce a remarkable "design paradigm shift" when dealing with hypersonic vehicles. By looking at the picture, the eye is caught by how supersonic design criteria (e.g. sharp leading edges, highly loaded wing, Whitcomb constant area rule) do not seem to hold for this vehicle - and for the X-30 of Figure 1.3, neither. Moreover, it would be difficult to identify a boundary (physical or functional) between different canonical elements of the transonic/supersonic aircraft, such as the main wing, the fuselage, or the engine. This leads to a crucial consideration: there is not such a net distinction. No element of the hypersonic vehicle is functionally independent of the others, and strong coupling between components is the rule rather than the exception.

Consider, for example, how a conventional aircraft generates the lift force required for sustained flight. In this case, the top-level function is satisfied by the main wing, designed keeping into consideration the requirements and constraints of the case. Other functions, such as the storage of payload and subsystems, or providing adequate thrust, are assigned to other elements and subsystems, namely the fuselage and the under-wing engines in the case of the canonical civil transport aircraft. On

the other hand, the MR3 exploits what is called a *waverider* configuration, in which the wing and fuselage are "blended" into the same structure, and the air intake, engines, and nozzle are integrated with the airframe as well.

When the vehicle is flying, a shockwave system forms around the vehicle starting from the nose. As discernible from Figure 1.5, there exists a remarkable pressure difference between the lower-facing and the upper-facing sides of the vehicle at a positive angle of attack; this is due to the locally variable "strength" of the complex three-dimensional shock system in different regions. The resultant of the integrated pressure forces can be decomposed into a lifting component, L, and a drag force, D. The common approach is, therefore, to exploit the gas dynamics involved and make the entire vehicle - and not the wing alone - sustain its weight, hence the name *waverider*. This configuration was chosen as the best compromise between aerodynamic efficiency (typically, $L/D > 6$), internal layout optimization, and flight qualities (e.g. longitudinal stability) along the whole mission spectrum.

Speaking about the propulsion system, the MR3 utilizes a peculiar layout with all the *combined cycle* engine modules (six air turbo rockets and a dual-mode ramjet) positioned on the top of the vehicle. In such a fashion, the entire propulsion system flow path - from the inlet to the nozzle - is embedded in the airframe, as visible in Figure 1.6. As reported in [9], this helps in getting the maximum planform available for lift generation and allows for reduced drag penalties. Another advantage of having both the air intake and exhaust nozzle embedded in the airframe is that the body itself becomes part of these elements. Indeed, the air intake can take advantage of the shockwave originating in the foremost portion of the vehicle (external compression air intake), while the exhaust nozzle expansion ratio can be pushed near the optimal value for a stratospheric flight using a semi-guided expansion involving the aircraft's afterbody and without the need of a big, heavy nozzle. A third, but far from irrelevant merit of this configuration is that it allows the biggest characteristic length of the combustion chamber possible, compared with the scale of the aircraft. This fact is crucial: one of the main difficulties in high-speed propulsion is maintaining a proper mixing and combustion efficiency when the characteristic time of mixing (τ_m) becomes comparable with the characteristic time of occurring chemical reactions (τ_c). A higher residence time in the reactor (i.e. adequate combustor length) is favorable since it enhances mixing and consequently combustion efficiency.

So far, we mainly discussed how the far-reaching coupling between external geometrical features and engine operation implies a broad-spectrum, multi-disciplinary approach. The problem, however, is way more complex than that. For example, the vehicle should be able to store a sufficient amount of fuel and payload, necessities that can occupy a considerable fraction in volume. This fact makes the arrangement of the internal layout a particularly challenging task. In addition to that, the empty mass fraction of the vehicle should be as low as possible, while of course satisfying resistance and fatigue criteria in a demanding flight environment. Storage of cryogenic liquids in the tanks, flight stability issues, trajectory optimization: the list of areas that need to be mastered to achieve practical hypersonic flight is quite long, and we could dive into every subsystem and its interactions to highlight a striking degree of complexity. This, however, is not the scope of this work, which indeed will focus on the combustion chamber of the HIFiRE 2 vehicle. In the next section, the reader will find a more detailed, but still concise, explanation of the working principles of the most established propulsion system concepts for hypersonic vehicles.

1.2.2 Propulsion System Concepts for Hypersonic Vehicles

In the opening of Section 1.2, it was implicitly stated that one possible definition of a hypersonic vehicle could be that of "a vehicle flying in the hypersonic regime, i.e. at a speed approximately five-fold the free-stream speed of sound". This definition, however, lacks some details of paramount importance when talking about propulsion technologies. In fact, despite the fact that both the Apollo capsule, the Space Shuttle, and STRATOFLY MR3 are hypersonic vehicles, they show completely different propulsion system requirements. The range of configurations spans from no propulsion at all, to rocket propulsion via hypersonic airbreathing propulsion. The bottom line here is that propulsion, as well the vehicle design in general, is intimately linked to the *mission* and the *concept of operations* of the system.

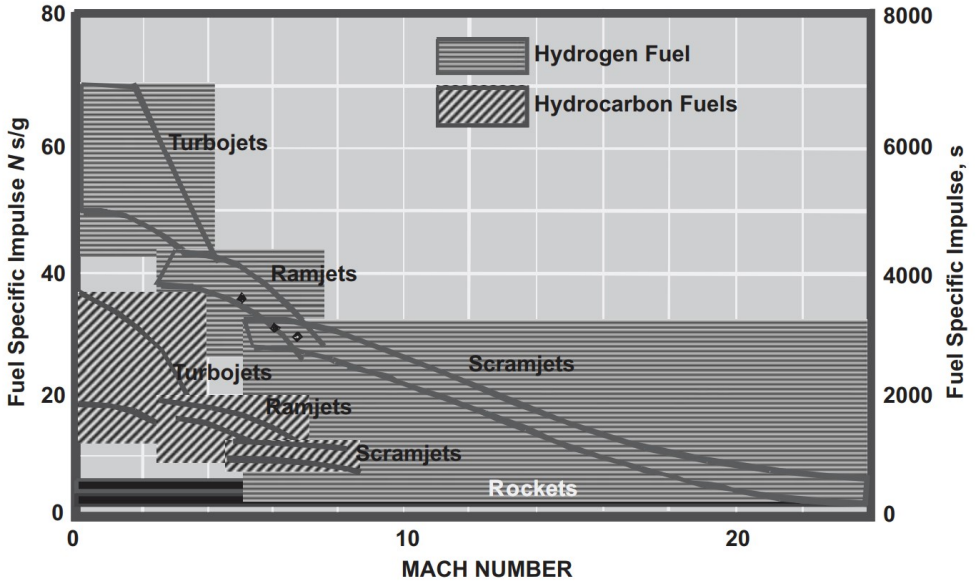

Fig. 1.7 Fuel-specific impulse trends over a wide range of the Mach number. Air-breathing engines relying on rotating turbomachinery increasingly lose their efficiency for $M > 3$, and ramjets become unsuitable for high M operation as well. Reaching orbital insertion velocities would require the system to operate in the higher-end of the Mach range in a rarefied atmosphere, and transition to a rocket engine would most probably be required. Image from [5].

Trends for the specific impulse over a wide range of Mach number M are compared in Figure 1.7 for disparate propulsion technologies and different fuel choices. The definition of specific impulse as thrust-to-mass-flow ratio is expressed as:

$$I_{sp} = \frac{\text{thrust force}}{\text{gravimetric fuel mass flow}} = \frac{F}{\dot{m}_f g}$$

The equation above is, in words, a way of quantifying how many N of thrust force are produced when fuel is consumed at a certain rate, measured in N/s. This parameter is often used as a global indicator of the efficiency of a propulsion system; as one of the terms of Breguet's range equation, it is also useful in the estimation of the overall performance of the vehicle. From a broader perspective, it gives a top-level clue on how "chemical enthalpy" (i.e. the energy contained in the fuel's molecular bonds) is *transformed* into the work of the thrust force, incorporating a variety of factors like fuel energy density, thermodynamics, combustion, efficiencies of components (e.g. inlet and nozzle).

Figure 1.7 emphasizes how deeply the choice among different technologies is driven by the mission, and by the Mach number window in which the vehicle is supposed to operate. Aircraft designed to operate up to the supersonic regime perform the best when equipped with turbine-based engines; nevertheless, when the Mach number increases, turbomachinery reaches its operational limit due to fluid-dynamics losses, thermal loads, and related structural issues. Getting rid of moving parts, and achieving the prescribed pressure and temperature utilizing changes in the cross-sectional area alone, make the ramjet perform better than the turbine-based engine in the high supersonic window. Increasing the flight M further, however, would make ramjets inadequate as well. Slowing down air to a subsonic speed in the combustion chamber would become tremendously inefficient, and keeping I_{sp} at acceptable levels would then require combustion to occur in a supersonic flow in what is called a supersonic combustion ramjet, or *scramjet* for short. A brief explanation of the thermodynamic cycle and working principles of the ramjet-based engine[2] will be given in Section 1.2.3.

1.2.3 The Ideal Ramjet/Scramjet Thermodynamic Cycle

Generally speaking, propulsion is the science - or the art - of *transforming energy* from a "reservoir" form, e.g. chemical enthalpy of the fuel, into heat and kinetic energy: it is, therefore, clear that understanding how a propulsive system works passes through the analysis of its thermodynamic cycle.

Figure 1.8 clarifies the standard station designation used for scramjet engines introduced in the book *Hypersonic Airbreathing Propulsion* by Heiser and Pratt [10]. The engine stations' designation follows the same standardized enumeration used for turbine engines, although the ramjet engine involves a lower number of elements. Following the flow path in its streamwise evolution, the working fluid experiences a sequence of transformations between thermodynamic states:

- **State 0**: it is representative of the free-stream, undisturbed thermodynamic state of atmospheric air. Adopting the ISA model, the flow properties are known once the altitude z and the Mach number M are defined;

[2]The ram pressure, or dynamic pressure, is a macroscopic, intensive property measure of the large-scale linear momentum of a flow. Since both the ramjet and scramjet work through conversion of ram pressure into thermodynamic pressure they are, ultimately, part of the same family of engines.

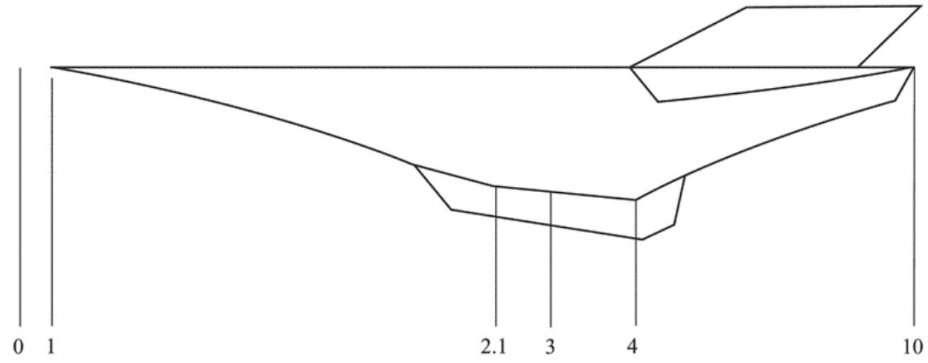

Fig. 1.8 Schematic representation and station numbering of an airframe-integrated scramjet engine. Notice how the designation follows the one used in gas-turbine engines. Flow path from left to right. Image from [5].

- **Transformation 0 → 1**: this transformation is representative of the discontinuity in thermodynamic properties across the shockwave originating from the nose of the vehicle and it is part of the compression transformation;
- **Transformation 1 → 2.1**: after going through the nose-attached shock, the flow experiences further compression in the forebody of the vehicle (external compression) and in the intake duct (internal compression). State 2.1 represents the flow conditions at the exit of the main compression element, i.e. the air intake;
- **Transformation 2.1 → 3**: this change brings the working fluid from the air intake exit station to the combustion chamber entrance and occurs through the *isolator*, an element whose function is to uncouple the air intake from what is happening in the combustion chamber;
- **Transformation 3 → 4**: between these two stations, heat is released by means of a combustion reaction. Chemical energy is transformed into thermal energy (sensible enthalpy). The one-dimensional Mach number at which the heat is released is what differentiates the ramjet from the scramjet engine;
- **Transformation 4 → 10**: the high-enthalpy exhaust products are expanded through a nozzle, the element in charge of converting thermal energy into kinetic energy and achieving thrust;
- **Transformation 10 → 0**: the exhaust products are released into the atmosphere, where equilibrium is ultimately reached and the cycle is closed.

The ideal thermodynamic cycle on the enthalpy-entropy diagram is represented in Figure 1.9.

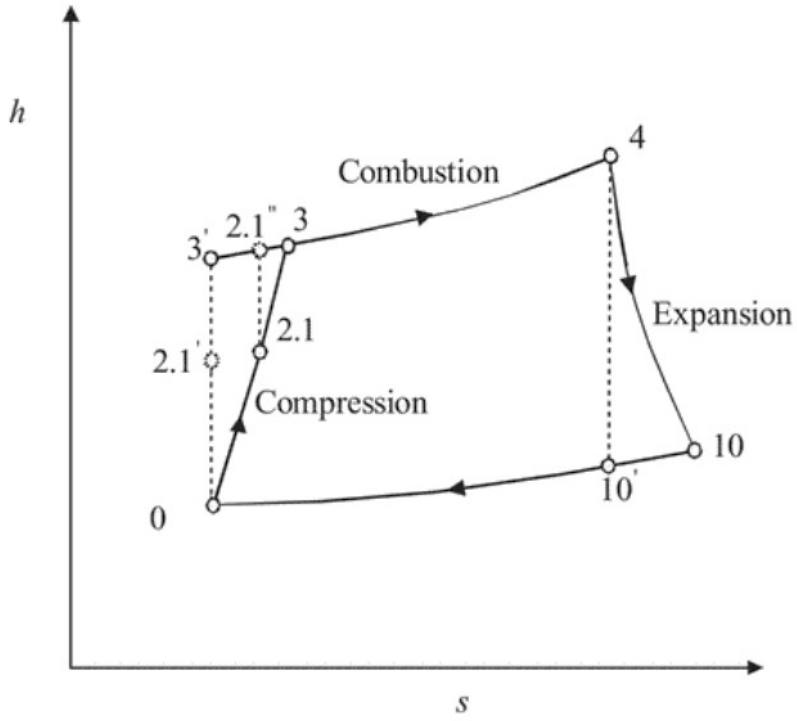

Fig. 1.9 Ideal thermodynamic cycle of a ramjet/scramjet, reported by [5]. The engine stations' designation is the same reported in Figure 1.8.

Under a set of simplifying assumptions - which will be discussed soon - the thermodynamic efficiency of the cycle can be evaluated by modeling it with a Brayton-Joule cycle, where two isentropic (i.e. adiabatic and reversible) compression and expansion transformations are linked by two isobaric transformations with heat addition (combustion) and subtraction.

At this level of analysis it is general practice to assume that both air and the exhaust products remain of the same composition during the transformations (their chemistry is said to be *frozen*); the combustion mechanism - which by definition would violate this assumption - is substituted with constant-pressure heat addition. Another further simplification, particularly useful in the analysis of the propulsive performance, is that the fuel mass-flow is negligible if compared to the air mass-flow and that all the captured mass-flow participate in the cycle and the propulsion energy conversion process.

Many of the phenomena involved in a scramjet engine flow path - e.g. shockwaves, boundary layers, and flames - are inherently local: this weakens the assumption of thermodynamic equilibrium, i.e. that the thermodynamic cycle represented on the $h-s$ diagram is a sequence of equilibrium states. However, at this level of analysis, those non-idealities and non-equilibrium phenomena - which influence the performance of the real engine - are modeled with the aid of global descriptive parameters. As an example, consider the two compression and expansion transformations of Figure 1.9. The assumption of isentropic evolution is as far from reality as possible. Compression occurs across a system of shockwaves, which always cause a discontinue increase in entropy, and dissipative phenomena also occur during the expansion through the nozzle. In addition to that, viscous losses and heat transfer - i.e. non-adiabaticity, sometimes desired in regenerative cycles - will participate in making the real evolution of the gas even more different than the one represented in the ideal cycle. Nevertheless, these effects are usually introduced by "lumping" these effects into component efficiencies.

As far as heat addition is concerned, it is well-known from thermodynamics that such a transformation could never happen without an increase in entropy (Rayleigh flow - see section 2.1.3), and therefore losses in total pressure associated with heat addition would be unavoidable. As a further matter, in reality, combustion could not happen without mixing: this adds irreversibility to the process. Moreover, dissociation reactions could increase even further the losses associated with the combustion process.

Finally, the assumption of negligible fuel mass-flow is, in some cases, limiting: further performance analysis of the propulsive system would probably require relaxing it. Besides this, in presence of active boundary layer control systems, it would also be necessary to take into account bleed and blowing mass flows, for the seek of a more precise investigation.

1.2.4 Combined Cycle Propulsion systems

Turbine-based and ramjet-based airbreathing engines cover a wide range of flight conditions. However, from an operational perspective, none of these concepts alone could practically propel an aircraft from take-off to hyper-velocities, as it would be required in the case of SSTO vehicles, or even in the case of a hypersonic

cruiser like the STRATOFLY MR3. In this context, the system should be designed to operate various propulsion technologies according to the phase of the mission; different scenarios exist, in which distinct kinds of engine might work in *sequence*, in *combination*, or in *synergy*.

Examples of sequential and combined operation are found in many concepts and vehicles from the past, e.g. the multi-staged hypersonic vehicle X-43A (see reference [11]) or the Pratt & Whitney J58 engine, which was equipped on the SR-71 Blackbird. Clearly, a reduction in the system's efficiency is traded-off in favor of lower overall complexity. Future designs, however, will be expected to be flexible, operable, and cost-effective in order to be competitive with other transportation systems. The role of the propulsion system optimization in reaching this goal is essential, and *combined-cycle propulsion systems* (CCP) offer a promising approach to the problem.

Based on the principle of synergistic enhancement of advantages and limitations of different cycles, they can be broadly classified into *turbine-based combined cycles* (TBCC) and *rocket-based combined cycles* (RBCC) . In both cases, these innovative concepts may include a ramjet, a scramjet, or a dual-mode combustion ramjet operating in synergy and sharing functions with turbine engines or rockets, and are therefore worth mentioning in this context. Given their complexity, a detailed description of these systems is off the topic of the present work. Reference [5] includes some issues about CCP systems relevant to the scramjet engine technology, while [9] reports the top-level features of the STRATOFLY MR3 propulsion system. The latter, in particular, involves the aforementioned *dual-mode combustion ramjet* (DMR) , providing thrust during hypersonic, sustained, stratospheric flight.

Generally speaking the DMR configuration, similar to the one used in the HIFiRE 2 experiment and that will be described later as the object of study of this work, consists of a combustion chamber capable of hosting a stable flame (and providing a net positive thrust) in a wide range of flight Mach number, operating as a ramjet at "low" speed and transitioning to a pure scramjet operational mode once the nominal cruise velocity is reached. Combining two ramjet-based cycles into the same physical flow path, the DMR can be regarded as one of the less complex - at least on paper - combined cycle propulsion systems.

Finally, it is worth mentioning another technology that is steadily gaining attention for hypersonic applications: *detonative propulsion*. Here, the thermodynamic

efficiency of the cycle can benefit from combustion occurring at high temperature and pressure across a detonation wave, i.e. a strong discontinuity sustained by the energy liberated by chemical reactions. Piotr Wolański in his survey article [12] gives an overview of the issue, presenting interesting concepts like the Standing Detonation Engine, the Pulse Detonation Engine, and the Rotating Detonation Engine.

1.3 Scope of the Work

In this first introductory chapter, it has been emphasized how practical hypersonic flight requires an effort that is mostly beyond the technological limit of our times. Many of the physical phenomena involved in external aerothermodynamics and supersonic combustion are not completely well understood, leaving great degrees of uncertainty about models and experimental results. Moreover, the intrinsic complexity of the aircraft and the level of integration of subsystems require a holistic design method that is extremely challenging and charming.

We could state that technological advancement, in almost all its branches, is essentially about taking a "big problem" that would not be manageable as a whole, reducing it to many "small problems", handling them most effectively and combining the results to - with some hope - provide a solution to the initial, humongous problem. This work, intended to focus on a particular engine component rather than to attempt the characterization of the whole propulsion system, has been conducted with this mind frame. The *object* of the investigation is the combustion chamber used in the HIFiRE 2 program; the *aim*, to characterize the phenomena related to supersonic combustion in cavity-stabilized combustors by applying models and predictive tools that will be described in the following chapters. Constraints of various nature have led to a somehow restricted analysis. However, assumptions and omissions will be listed and commented on a case by case.

Chapter 2

Background Information and Theory

Now that the introduction to the thesis topic has been made and the context has been created, it is time for some additional background information. First, Section 2.1 will be devoted to a brief presentation of the most important physical phenomena involved and how they are, from first principles or observation, put into elegant mathematical models. In Section 2.2, we will make an effort and try, in a concise way, to understand how the mathematical representation of reality is "translated" into a discrete mathematical structure that approximates well enough the "continuum" while being suitable for digital computing. After that, the reader will find some pertinent information and references about the HIFiRE 2 program, the HDCR ground experiment, and their output.

2.1 Mathematical Models

The close connection between mathematics and physical phenomena is something philosophers of science have been discussing for thousands of years, from the Pythagoreans to Galileo and more recent insights. In the popular article *The Unreasonable Effectiveness of Mathematics in the Natural Sciences*, published in 1960, physicist Eugene Wigner states:

> "The miracle of the appropriateness of the language of mathematics for the formulation of the laws of physics is a wonderful gift which we neither understand nor deserve. We should be grateful for it and hope

> that it will remain valid in future research and that it will extend, for better or for worse, to our pleasure even though perhaps also to our bafflement, to wide branches of learning."

Letting deep epistemological discussions apart - but remembering how powerful the language of mathematics is in describing real-world phenomena - the following section will focus on exploring the mathematical framework for *supersonic turbulent reacting flows*, with its assumptions and limitations.

The Continuum Hypothesis

In Section 1.2.3, attention was posed to presenting the generic ramjet/scramjet thermodynamic cycle, and, following the evolution of a fluid volume along the flow path, how transformations are achieved in different regions of the engine. One of the limits of this classical thermodynamics approach is the assumption of equilibrium states: therefore, a deeper level of detail is needed to include models of local and non-equilibrium phenomena like *boundary layers*, *turbulence*, *unsteadiness*, *finite-rate chemical reactions* and so on.

As a starting point, a basic concept used in classical thermodynamics persists: the *thermodynamic system*[1], composed by a certain number of elementary units (molecules or atoms), is assumed to be describable in its macrostate (i.e. thermodynamic properties) by looking - from a statistical point of view - at the distribution of microstates in the elementary units' population. This *statistical* approach, which is the foundation of statistical thermodynamic theories like the kinetic theory of gases, is viable if and only if the thermodynamic system actually contains a *statistically relevant* number of units, i.e. molecules.

Fortunately enough, observation tells that fluids, like air and water, exhibit rich and complex dynamics at a generic macroscopic scale (L), which is usually separated from the molecular scale (λ, free molecular mean path) by several orders of magnitude. The dimensionless parameter comparing these two scales is the Knudsen number Kn, named after the Danish physicist Martin Knudsen and which is defined as:

[1] The definition of *thermodynamic system* is deliberately broad: it can be regarded as the spatially unresolved region in which a classical thermodynamic cycle takes place, or a control volume in the context of fluid mechanics.

$$Kn = \frac{\lambda}{L}$$

In most cases relevant for engineering applications:

$$\lambda \approx 1 \times 10^{-2}\,\mu\text{m} \longrightarrow Kn \ll 1$$

This means that the *continuum approximation* is legit and the flowfield can be rigorously described by means of *fields* describing its kinematic, thermodynamic, and chemical state. Mathematically speaking, those fields are scalar-valued or vector-valued functions in the domain of the three spatial coordinates and time:

$$\phi = \phi(\mathbf{x}, t)$$

where ϕ is here used to describe an arbitrary intensive quantity.

Putting everything together: what the continuum hypothesis implies is that, due to the separation between the microscopic and the macroscopic scales ($Kn \ll 1$), at every position $\mathbf{x}$ belonging to the domain of interest, it is possible to represent with a mathematical object (a field) the macrostate of a statistically relevant number of molecules. This, however, is not always the case. A pertinent example is that of an Hypersonic Reentry Vehicle (HRV) on its way back to Earth. Up in the external layers (i.e. the exosphere), the atmosphere is so rarefied that λ can be compared with the characteristic length of the vehicle: adopting the continuum hypothesis for this kind of problem would therefore lead to wrong results and fallacious design choices.

2.1.1 Field Equations for Fluids

The field equations for fluids are a set of partial differential equations (PDEs) which mathematically describe how certain properties of a fluid vary in space and time, given the proper initial and boundary conditions. Built upon the continuum hypothesis, they are derived using fields to express, by means of transport equations, the conservation principles on which classical physics is founded: the conservation of *mass*, *momentum*, and *energy*, hence their alias *conservation laws*.

It is important to point out that since the conservation laws are derived from fundamental principles of nature which ultimately differentiate what *can occur* from what *can not occur*, they are exact and fundamental. Certain phenomena - like the ones related to molecular transport or turbulence - need to be modeled in a less absolute way; they are usually described using so-called *constitutive equations*, which allow the same conservation laws to deal with different classes of problems.

The General Transport Equation

As a starting point, let us consider the fundamental structure of the notional transport equation for a specific (i.e. per unit mass) property of a fluid. In general, this equation expresses the balance between different contributions in a certain region of space, called *control volume*. In words:

$$\boxed{\text{rate of change in time}} + \boxed{\text{convective term}} = \boxed{\text{diffusive term}} + \boxed{\text{source terms}}$$

- $\boxed{\text{rate of change in time}}$: this term represents how the specific quantity, integrated over the control volume, is changing over time;

$$\frac{\partial}{\partial t}\int_V \rho\phi \, \mathrm{d}V \tag{2.1}$$

- $\boxed{\text{convective term}}$: this term quantifies the contribution to the global balance given by convective phenomena, i.e. *motion* of fluid which may be driven by differences in the flow properties[2]. The net flow of a quantity through the surface or curve is usually expressed as *flux integral*.

$$\oint_{\partial V} \rho\phi\mathbf{u}\cdot\hat{\mathbf{n}} \, \mathrm{d}S \tag{2.2}$$

  where ∂V represents the control volume's boundary, $\mathbf{u}$ the velocity vector, $\hat{\mathbf{n}}$ the unit vector normal to the infinitesimal surface element dS;

[2]In the present work, *convection* and *advection* are used as synonyms, although convection involves fluid motion driven by differences in properties (like natural convection in heat transfer) while advection is related to the concept of "transport" by fluid motion (like ink in a stream).

- diffusive term : terms of the form of 2.3 quantify the net change caused by diffusive phenomena, i.e. processes resulting from the random motion of molecules that transport conserved quantities across ∂V. Molecular in their nature, diffusive phenomena are driven by local non-homogeneity - namely, gradients - in the field of the specific property the conservation law is dealing with.

$$\oint_{\partial V} \rho \Gamma_\phi (\nabla \phi) \cdot \hat{\mathbf{n}} \, \mathrm{d}S \tag{2.3}$$

  where Γ_ϕ is the diffusion coefficient of the quantity ϕ;

- source terms : model the presence of sources or sinks of the transported quantity inside the control volume. Examples are volumetric forces acting on the fluid (momentum equations) or heat release due to chemical reactions (energy equation), generically expressed in 2.4 with the symbol S_ϕ .

$$\int_V S_\phi(\phi) \, \mathrm{d}V \tag{2.4}$$

If we put all the terms from 2.1 to 2.4 together, what we get is the general transport equation in its *integral, conservative* form:

$$\frac{\partial}{\partial t} \int_V \rho \phi \, \mathrm{d}V + \oint_{\partial V} \rho \phi \mathbf{u} \cdot \hat{\mathbf{n}} \, \mathrm{d}S = \oint_{\partial V} \rho \Gamma_\phi (\boldsymbol{\nabla} \phi) \cdot \hat{\mathbf{n}} \, \mathrm{d}S + \int_V S_\phi(\phi) \, \mathrm{d}V \tag{2.5}$$

The standard derivation then proceeds by applying the Gauss theorem, a powerful theorem in calculus that states the equivalence of flux integrals with integral over the volume V of the divergence of the scalar or vector field of interest. Simultaneously assuming - without loss of generality - that the control volume has an arbitrary and time-independent shape, and given the linearity of integral and differential operators, we get to the *local, conservative, weak* form of the conservation equations:

$$\frac{\partial \rho \phi}{\partial t} + \boldsymbol{\nabla} \cdot (\rho \phi \mathbf{u}) = \boldsymbol{\nabla} \cdot (\rho \Gamma_\phi \boldsymbol{\nabla} \phi) + S_\phi(\phi) \tag{2.6}$$

which can be easily transformed into the *local, conservative, strong* form bringing all differential operators to the left hand term:

$$\frac{\partial \rho \phi}{\partial t} + \boldsymbol{\nabla} \cdot (\rho \phi \mathbf{u} - \rho \Gamma_\phi \boldsymbol{\nabla} \phi) = S_\phi(\phi) \tag{2.7}$$

If we then introduce the definition of the *material derivative*:

$$\frac{D}{Dt} = \frac{\partial}{\partial t} + \mathbf{u} \cdot \boldsymbol{\nabla}$$

we can, from 2.6, obtain the *local, non-conservative form*[3] of the transport equation:

$$\rho \frac{D\phi}{Dt} + \phi \frac{D\rho}{Dt} = -\rho\phi \boldsymbol{\nabla} \cdot \mathbf{u} + \boldsymbol{\nabla} \cdot (\rho \Gamma_\phi \boldsymbol{\nabla} \phi) + S_\phi(\phi) \tag{2.8}$$

It is important to point out that equations 2.5, 2.6, 2.7, 2.8 are all the same equation: they are only different points of view of the same fundamental principles. In particular, conservative forms focus on a fixed volume in space; this point of view, known as *Eulerian*, deals with the flow by looking at how the fields change in the region of interest. On the other hand, non-conservative forms are derived by following a fixed mass of fluid in its evolution. This viewpoint, known as *Lagrangian*, is linked to the Eulerian one by the concept of material derivative.

Both integral forms such as 2.5 and local forms like the one reported in 2.7 are used in the domain of Computational Fluid Dynamics. Integral forms, however, have a greater generality since they don't necessarily require the fields to be defined as a smooth function of the space coordinates. This has some interesting applications in the modeling of certain classes of flows, where discontinuities in the fields are mathematically allowed by the PDEs governing them.

[3]The adjective *non-conservative* comes from the fact that, due to the splitting of the differential operator, the argument of the differentiation is *not* the conserved quantity anymore; as a consequence, the expanded derivative is not a telescopic series.

2.1.1.1 The Mass Equation

The equation of the conservation mass reflects one of the fundamental principles of classical physics: in a system, mass is neither created nor destroyed, therefore it is conserved over time. From equation 2.5 and 2.6, if we defined the specific property of "mass per unit mass" as the unity ($\phi := 1$), we get, in integral (2.9) and local (2.10) conservative form:

$$\frac{\partial}{\partial t}\int_V \rho \, \mathrm{d}V + \oint_{\partial V} \rho \mathbf{u} \cdot \hat{\mathbf{n}} \, \mathrm{d}S = 0 \tag{2.9}$$

$$\frac{\partial \rho}{\partial t} + \boldsymbol{\nabla} \cdot (\rho \mathbf{u}) = 0 \tag{2.10}$$

These equations tell the same thing: “in fixed region in space (i.e. the unchanging control volume) the rate of change of the mass contained in it is equal to the net mass flux across its boundary”. Equation 2.10 , as well as all the conservation equations in their local form, can be regarded as a limit case of the integral form in which the measure of the control volume tends to zero.

2.1.1.2 The Momentum Equations

Some of the most popular and everyday-experienced physical principles are the three Newton’s laws of motion. The second one, in particular, relates the motion of a body to the resultant of the forces acting on it, reflecting the fundamental law of conservation of *linear momentum*:

$$\mathbf{F} = m\mathbf{a}$$

In a continuum, the property of specific linear momentum is simply the velocity field, therefore $\phi := \mathbf{u}$. Substituting in 2.5 and 2.6, we obtain the vector equation of momentum in integral and local conservative forms, respectively:

$$\frac{\partial}{\partial t}\int_V \rho \, \mathbf{u} \, \mathrm{d}V + \oint_{\partial V} \rho \, \mathbf{u} \otimes \mathbf{u} \cdot \hat{\mathbf{n}} \, \mathrm{d}S = \oint_{\partial V} \mathbf{S} \cdot \hat{\mathbf{n}} \, \mathrm{d}S + \int_V \rho \mathbf{f_e} \, \mathrm{d}V \tag{2.11}$$

$$\frac{\partial \rho \, \mathbf{u}}{\partial t} + \boldsymbol{\nabla} \cdot (\rho \, \mathbf{u} \otimes \mathbf{u}) = \boldsymbol{\nabla} \cdot \mathbf{S} + \rho \mathbf{f_e} \tag{2.12}$$

in which $\mathbf{S}$ is the stress tensor and $\mathbf{f_e}$ are external, specific forces acting on the fluid element. A more intuitive insight in the physical meaning of the momentum vector equation is given by its local, non-conservative form. From 2.8, and after some re-elaboration of the terms:

$$\rho \frac{D\mathbf{u}}{Dt} = \boldsymbol{\nabla} \cdot \mathbf{S} + \rho \mathbf{f_e} \tag{2.13}$$

Translated in plain English, what equation 2.13 is telling us is that acceleration of fluid elements (in the continuum meaning) is caused by two contributions: forces acting on the surface of the control volume and forces acting "per unit volume", like gravitational and electromagnetic forces.

Moving a step further, the total stress tensor $\mathbf{S}$ can be decomposed into its *hydrostatic* and *deviatoric* components, which in the case of a fluid means:

$$\mathbf{S} = -p\mathbf{I} + \boldsymbol{\tau} \tag{2.14}$$

The hydrostatic tensor contains the isotropic pressure stresses, which have compressive nature. On the other hand, the deviatoric component contains *viscous stresses*, which originate in presence of non-homogeneity and molecular diffusion. The constitutive equations modeling the viscous stress tensor will be reported and commented in Section 2.1.2.3.

After 2.14, equations 2.11, 2.12 and 2.13 can be rewritten getting pressure forces - a quantity of interest in fluid dynamics - to show up explicitly. For example, 2.12 becomes:

$$\frac{\partial \rho \mathbf{u}}{\partial t} + \boldsymbol{\nabla} \cdot (\rho \mathbf{u} \otimes \mathbf{u}) = -\boldsymbol{\nabla} p + \boldsymbol{\nabla} \cdot \boldsymbol{\tau} + \rho \mathbf{f_e} \tag{2.15}$$

2.1.1.3 The Energy Equation

The third, inviolable principle on which physics - and thus fluid dynamics - is based is that of the conservation of energy. In this context, thermodynamic potentials like the internal energy e and enthalpy h are used as dependent variables in different formulations. From a theoretical standpoint, there is no difference between these equations; moreover, it is always possible to consistently move from one form to

the other. For brevity, only the equation written in terms of total internal energy (non-chemical) will be here reported, in the local conservative form:

$$\frac{\partial \rho E}{\partial t} + \boldsymbol{\nabla} \cdot (\rho \, \mathbf{u} E) = -\boldsymbol{\nabla} \cdot (p \, \mathbf{u}) + \boldsymbol{\nabla} \cdot (\boldsymbol{\tau} \cdot \mathbf{u}) + \rho \mathbf{f_e} \cdot \mathbf{u} - \boldsymbol{\nabla} \cdot \mathbf{q} + \dot{Q}_c + \dot{Q}_e \quad (2.16)$$

Equation 2.16 tells that, from a Eulerian point of view, the total enthalpy rate of change in time is a balance of the convective term and:

- $-\boldsymbol{\nabla} \cdot (p \, \mathbf{u}) = -(\boldsymbol{\nabla} p \cdot \mathbf{u} + p \boldsymbol{\nabla} \cdot \mathbf{u})$: term including both the mechanical and thermodynamic effects of pressure;
- $\boldsymbol{\nabla} \cdot (\boldsymbol{\tau} \cdot \mathbf{u})$: often referred to as *mechanical viscous source*, it models the transfer of energy from the macroscopic scale ($\mathbf{u}$) to the microscopic one via molecular diffusion ($\boldsymbol{\tau}$);
- $\rho \mathbf{f_e} \cdot \mathbf{u}$: how the work of volumetric forces contributes in the energy balance over time;
- $\boldsymbol{\nabla} \cdot \mathbf{q}$: all those heat transfer phenomena interesting the boundary of the control volume. The heat flux vector field $\mathbf{q}$ includes both *conductive* and *radiative* heat transfer; extra constitutive equations are required to define it;
- $\dot{Q}_c$: chemical bulk heat release, which in the more specific context of reactive flows emerges from the the conversion of a chemical form of energy into a sensible one;
- $\dot{Q}_e$: bulk heat release due to other external sources.

For a more detailed treating of the energy equation in the combustion landscape the reader is invited to consult specialized textbooks like [13].

2.1.1.4 The Species Conservation Equation

Multi-species reacting flows involve a variety of chemical compounds, each formed by a combination of atoms of different elements. Roughly speaking, a chemical reaction is a process in which reactant molecules interact via molecular collisions and *rearrange* their constituent atoms to create different substances as reaction products. Under normal laboratory conditions, the law of the conservation of matter states that

elements cannot be transformed into other elements and chemical reactions should be balanced: therefore, there emerges the need for some extra equations describing the evolution of *species mass fraction* fields. Focusing on the generic mass fraction Y_k and adopting the general form of 2.6, we obtain:

$$\frac{\partial \rho Y_k}{\partial t} + \boldsymbol{\nabla} \cdot (\rho \, \mathbf{u} Y_k) = -\boldsymbol{\nabla} \cdot \mathbf{j_k} + \dot{\omega}_k \tag{2.17}$$

The terms appearing on the right hand term represent respectively the diffusion of mass ($\mathbf{j_k}$) and the net rate of production-consumption of the k-th compound in all the chemical reactions involved ($\dot{\omega}_k$).

2.1.2 Constitutive Equations

To get the motion of fluids to obey the laws of physics, the governing equations reported in Section 2.1.1 need to be simultaneously satisfied. The equations are here reported in their local, conservative form for reference. Terms like body forces, radiative heat transfer, and external heat sources are often neglected; therefore, the equations have been purged of those terms.

$$\begin{cases} \dfrac{\partial \rho}{\partial t} + \boldsymbol{\nabla} \cdot (\rho \mathbf{u}) = 0 & (2.10) \\ \dfrac{\partial \rho \, \mathbf{u}}{\partial t} + \boldsymbol{\nabla} \cdot (\rho \, \mathbf{u} \otimes \mathbf{u}) = -\boldsymbol{\nabla} p + \boldsymbol{\nabla} \cdot \boldsymbol{\tau} & (2.15) \\ \dfrac{\partial \rho E}{\partial t} + \boldsymbol{\nabla} \cdot (\rho \, \mathbf{u} E) = -\boldsymbol{\nabla} \cdot (p \, \mathbf{u}) + \boldsymbol{\nabla} \cdot (\boldsymbol{\tau} \cdot \mathbf{u}) - \boldsymbol{\nabla} \cdot \mathbf{q} + \dot{Q}_c & (2.16) \\ \dfrac{\partial \rho Y_k}{\partial t} + \boldsymbol{\nabla} \cdot (\rho \, \mathbf{u} Y_k) = -\boldsymbol{\nabla} \cdot \mathbf{j_k} + \dot{\omega}_k & (2.17) \end{cases}$$

The system of equations hereby reported needs to be closed with additional equations for it to be *determined*. In the following, we will discuss the constitutive equations relevant to the case of the present work.

2.1.2.1 Equation of State

Observing the governing equations closer, we can notice that three thermodynamic variables appear: pressure, density, and total internal energy. Experience with thermodynamic systems tells that these three parameters are *not* independent; moreover, the thermodynamic properties of multi-specie, reacting systems are coupled with their composition. The equation constraining those variables and giving the right number of degrees of freedom is the so-called *equation of state*. Assuming a mixture of ideal gases, enthalpy is a function of temperature and composition only (see Section 2.1.2.2), and we can write the relation as:

$$p = p(\rho, T, Y_k) = \rho R_u T \sum_{k=1}^{N_s} \frac{Y_k}{\mathscr{M}_k} \tag{2.18}$$

where R_u indicates the universal gas constant and $\mathscr{M}_k$ represents the molecular weight of the k-th specie. An alternative writing of equation 2.18 defines the molecular weight of the mixture as in the following, with the consequent rearrangement of the terms:

$$\frac{1}{\mathscr{M}_{mix}} = \sum_{k=1}^{N_s} \frac{Y_k}{\mathscr{M}_k} \longrightarrow p = \rho R_{mix} T$$

2.1.2.2 Enthalpy-Temperature Equation

Under the hypothesis of a mixture of thermally perfect gases the enthalpy of each specie is a function of temperature only, which means:

$$\mathrm{d}h_k = c_{p_k}(T)\,\mathrm{d}T \longrightarrow h_k - h_{0_k} = \int_{T_0}^{T} c_{p_k}(T)\,\mathrm{d}T$$

in which the subscript "0" represents the reference state, and $c_{p_k}(T)$ is usually a polynomial approximation of the real gas behavior. In this work, the JANNAF (Joint Army Navy NASA Air Force) polynomials, as implemented in the OpenFOAM library, have been adopted. Reference [14] shows their implementation. They are particularly practical since their coefficients also incorporate, for each specie, information about the enthalpy of formation, entropy, and other quantities of interest.

Defining now the constant pressure heat capacity of the mixture as $c_p = \sum_k c_{p_k}$ and taking $\overline{c}_p$ as the integral average of the polynomial approximation:

$$\overline{c}_p = \frac{1}{T - T_0} \int_{T_0}^{T} c_p(T)\,\mathrm{d}T$$

we can express temperature in terms of the static enthalpy via 2.19:

$$T = \frac{h - \sum_{k=1}^{Ns} Y_k h_{f,k}^0}{\overline{c}_p} \tag{2.19}$$

The straightforward relation between static and total enthalpy, appearing in equation 2.16, is then reported:

$$H = h + \frac{1}{2}\|\mathbf{u}\|^2$$

2.1.2.3 Viscous Stress Tensor

As touched in Section 2.1.1.2, the viscous stress tensor contains terms originating from non-homogeneity in the velocity field and molecular diffusion. In many practical applications and with a broad range of fluids (e.g. air, water) the viscous stress tensor depends linearly on the *rate of strain* tensor. In such a case, the fluid belongs to the class of *Newtonian fluids*, described by equation 2.20:

$$\boldsymbol{\tau} = k_v(\boldsymbol{\nabla} \cdot \mathbf{u})\mathbf{I} + 2\mu\mathbf{D} \tag{2.20}$$

where k_v represents the *bulk viscosity coefficient*, μ is the dynamic viscosity (see 2.1.2.6) and $\mathbf{D}$ is the rate of strain tensor deprived of its isotropic component and defined as $D_{ij} = \frac{1}{2}(\frac{\partial u_i}{\partial x_j} + \frac{\partial u_j}{\partial x_i}) - \frac{1}{3}\boldsymbol{\nabla} \cdot \mathbf{u}\delta_{ij}$.

Stokes, in what has become known as the *Stokes' hypothesis*, proposed that the bulk viscosity coefficient is, in fact, negligible. In such a case:

$$\boldsymbol{\tau} = 2\mu\mathbf{D} \longrightarrow \tau_{ij} = \mu\left(\frac{\partial u_i}{\partial x_j} + \frac{\partial u_j}{\partial x_i}\right) - \frac{2}{3}\mu\boldsymbol{\nabla} \cdot \mathbf{u}\delta_{ij} \tag{2.21}$$

This has some important consequences: remembering the decomposition of 2.14, to assume the validity of Stokes' hypothesis implies that mechanical and thermodynamic pressure are, in fact, the same - something that was implicitly

considered true in Section 2.1.2.1 when dealing with the equation of state. The reason is that $\boldsymbol{\tau}$ is purely deviatoric, and volumetric dilatations of the fluid element don't cause - under the aforementioned assumption - normal stresses. For a deeper treatise on the topic, see reference [15].

In the present work, the viscous stress term is calculated assuming a Newtonian fluid modeled under the validity of Stokes' hypothesis.

2.1.2.4 Thermal Flux Vector

The symbol $\mathbf{q}$ appearing in equation 2.16 represents, in principle, every flux of energy per unit time through the surface of the fluid element. In the specific case of high enthalpy flows, like the one interesting scramjet engines, two main forms of thermal flux are usually considered: *conductive* and *radiative*.

The former reflects how molecular transport of energy is experienced at the macroscopic level through heat conduction. Since it involves gradients-driven transport processes, a reasonable approximation is to relate heat conduction to the gradient of the temperature field, adopting the so-called Fourier's law for heat transfer:

$$\mathbf{q}_\alpha = -k\boldsymbol{\nabla}T \tag{2.22}$$

in which $k = [\mathrm{W}/(\mathrm{mK})]$ is the thermal conductivity of the gas mixture. Notice that in multispecies mixtures heat transfer can also be driven by mass diffusion along species concentration gradients.

Including the effects of thermal radiation in the governing equations for fluids adds remarkable complications both from the analytical and numerical standpoints, given the inherent non-linearity of the radiative flux vector term on the temperature and other uncertainties about how thermal radiation influences the boundary conditions. The interested reader could find a useful reference in the closing chapter of [16]. In the present work, the latter of the forms of thermal flux listed above, namely heat transfer due to thermal radiation, is not modeled.

2.1.2.5 Mass Diffusion of Species

Closing equation 2.17 with an adequate description of the mass diffusion mechanism is extremely important in the modeling of non-premixed diffusion flames; such a scenario includes combustion reactions in scramjet engines, where the process is dominated by transport properties and closely coupled with other physical phenomena associated with mixing, e.g. turbulence.

As a compromise between theoretical rigor and ease in the numerical implementation, Fick's law for mass diffusion is, in most cases, adopted:

$$\mathbf{j_k} = -\rho D_k \nabla Y_k \tag{2.23}$$

where D_k is the diffusion coefficient of specie k into the mixture. This simple gradient model, despite the approximation of neglecting mass diffusion driven by other phenomena, e.g. strong pressure gradients and body forces, is accurate enough for most practical engineering applications. The description of more detailed diffusion mechanisms and their physical justification is beyond the scope of this work. A detailed treatise of the topic can be found in [17] after J.O. Hirschfelder and C.F. Curtis, and is left here for reference.

2.1.2.6 Transport Coefficients

In the definition of the viscous term under the Stokes' hypothesis (equation 2.21) the dynamic viscosity μ appears as the proportionality factor between the viscous stress tensor and the deviatoric component of the strain tensor. In the cases of interest, temperature and mixture composition variations are not small; therefore viscosity is modeled using *Sutherland's formula*:

$$\mu = \frac{A_s \sqrt{T}}{1 + \frac{T_s}{T}} \tag{2.24}$$

in which A_s and T_s are provided constants relative to each specie (subscript k omitted). At this point, following [18], the individual thermal conductivity factors can be calculated using the *Eucken's approximation* via:

$$k = \alpha \rho c_p = \mu c_v \left(1.32 + 1.77 \frac{R_u}{c_v}\right) \tag{2.25}$$

The properties of the mixture are than calculated once its composition is known.

In Section 2.1.2.3, 2.1.2.4 and 2.1.2.5 it was pointed out that mass diffusion, viscosity and thermal conduction are all the macroscopic expression of molecular collisions. Thanks to such a shared physical understanding, it is a common approach to relate the *diffusivity coefficients* - which all have the same measurement unit of m^2/s in the SI system - with non-dimensional numbers that reflect the molecular nature of different fluids; those non-dimensional numbers are useful when analyzing classes of similar phenomena or in the derivation of the non-dimensional equations of motion. Among them, we here report:

- The Prandtl number, defined as:

$$Pr = \frac{\nu}{\alpha} = \frac{\text{momentum diffusion}}{\text{energy diffusion}}$$

- The Schmidt number, defined as:

$$Sc = \frac{\nu}{D} = \frac{\text{momentum diffusion}}{\text{mass diffusion}}$$

- The Lewis number, defined as:

$$Le = \frac{\alpha}{D} = \frac{\text{energy diffusion}}{\text{mass diffusion}}$$

Finally going back to Section 2.1.2.5, it is worth noting how the diffusion coefficients D_k reflects how, in a multispecies mixture, each specie is diffused into the mixture, interacting with all the other components differently; that given, it is reasonable to expect D_k to be approximated by a function of the binary diffusion coefficients between specie k and all the other $N_s - 1$ species. Describing all the mechanisms beyond those phenomena adds some remarkable complexity to the CFD modeling of combustion. However, in this work, the values of D_k were obtained providing, for each specie, the value of the Schmidt number Sc_k that related the mass diffusivity to the momentum diffusivity $\nu = \mu/\rho$, obtained after 2.24.

2.1.3 One Dimensional Flow with Heat Addition

Before addressing the modeling of more intricate phenomena such as finite-rate chemistry and turbulence, it is useful to spend a few lines reasoning about the thermodynamics of a flow with heat addition using a simple - but yet insightful - one-dimensional model also known as *Rayleigh flow*.

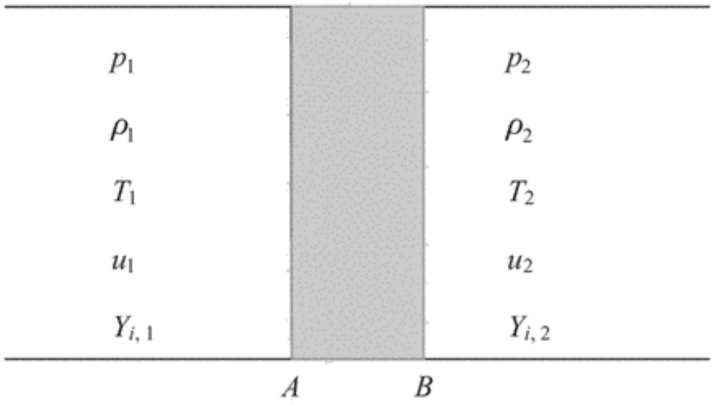

Fig. 2.1 Schematic of one-dimensional flow between uniform regions 1 and 2, with real flow phenomena (e.g. heat addition, viscosity, shockwaves) allowed inside the control volume from A to B. Image credits to [5].

Under the assumption of one-dimensional, inviscid, steady, flow of a perfect gas, the governing equations integrated along the finite control volume from 1 to 2 (see Figure 2.1) transform into simple algebraic equations:

$$\begin{cases} \rho_1 u_1 = \rho_2 u_2 \\ p_1 + \rho_1 u_1^2 = p_2 + \rho_2 u_2^2 \\ H_1 + q = H_2 \\ Y_{k,1} = Y_{k,2} \end{cases} \tag{2.26}$$

where q represents the heat addition/subtraction in region A→B. It is clear that the conservation of energy imposes a change in total temperature across the control volume. Following [6], after some passages we obtain:

$$\frac{T_0}{T_0^*} = \frac{(\gamma+1)M^2}{(1+\gamma M^2)^2}[2+(\gamma-1)M^2] \tag{2.27}$$

which is translated in graphical terms into Figure 2.2 and Figure 2.3. Equation 2.27 relates the flow total temperature T_0 at a Mach number M to the total temperature of the *thermally choked* flow; it is particularly useful to determine the one-dimensional thermophysical properties of the gas after a certain amount of heat has been added or subtracted.

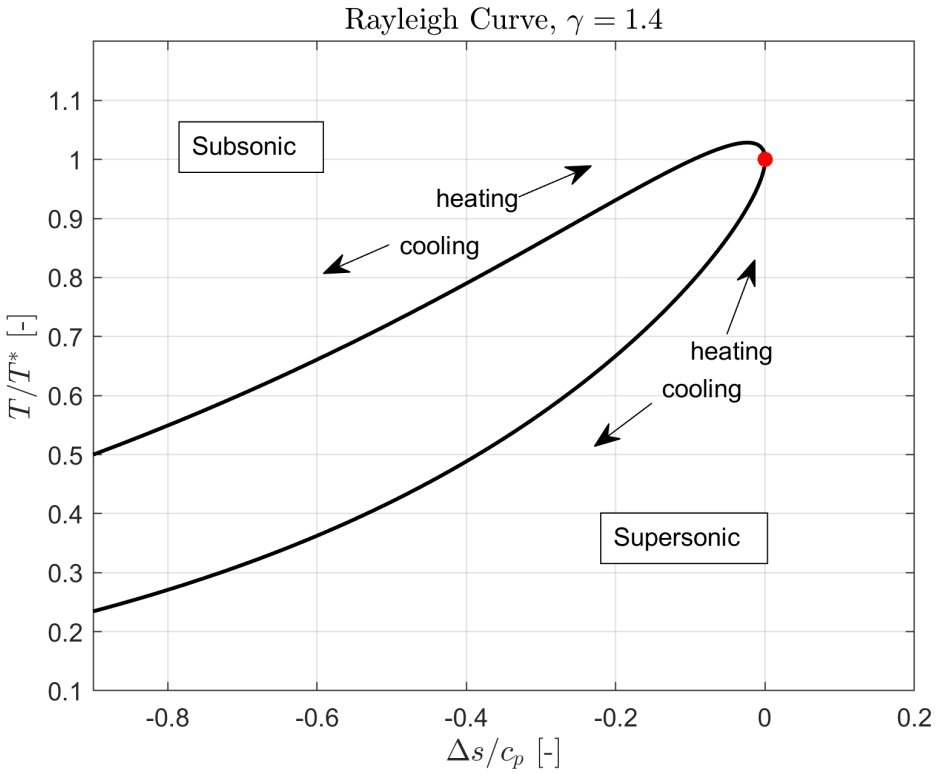

Fig. 2.2 Rayleigh curve for one-dimensional flow with heat addition, represented in the $h-s$ plane.

It is important to point out that heat addition always leads the flow to the sonic state, with a much faster slope on the supersonic side (Figure 2.3). This is because energy is spread differently between kinetic energy and enthalpy in the subsonic and supersonic regimes. In the subsonic regime, $M = 1$ is approached through the kinematic velocity and the speed of sound increasing, with the first effect prevailing on the second. On the other hand, heat addition in the supersonic regime mainly changes the speed of sound, and this makes the Mach number drop quite fast.

When the heat addition approaches the critical one, the flow is said to be *thermally chocked*: no further heat addition would be possible without some change in the

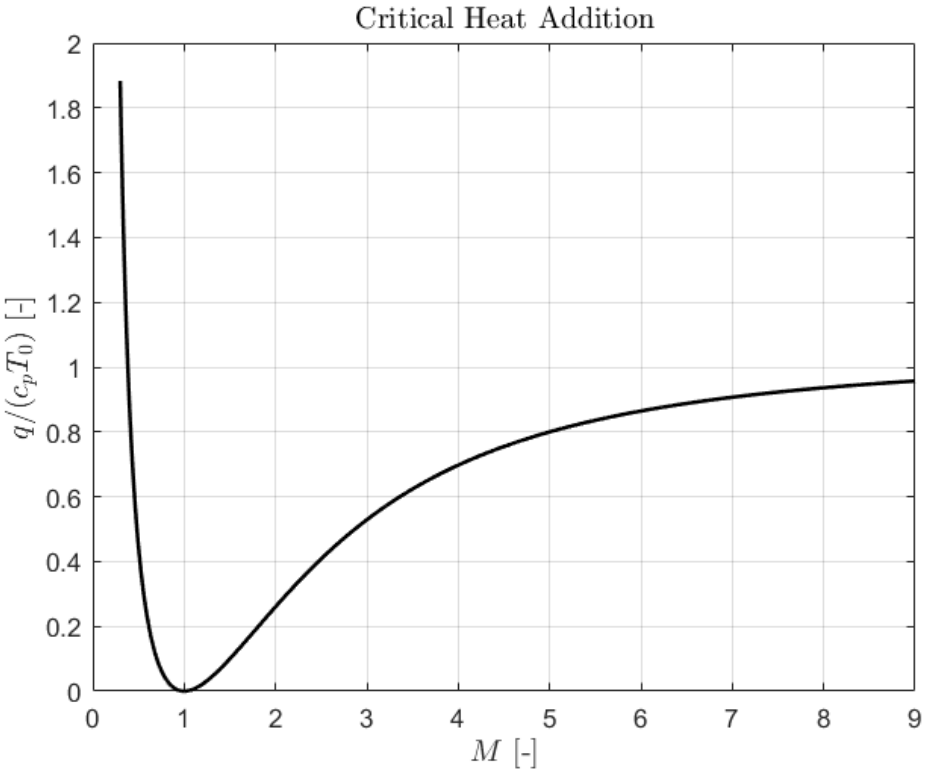

Fig. 2.3 Critical heat addition versus flow Mach number.

boundary conditions, which usually manifests itself through strong discontinuities (shockwaves) in the flowfield.

2.1.4 Chemically Reacting Flows

The reactive version of the Navier-Stokes equations and the constitutive relations of Section 2.1.2 are not sufficient to describe the physical complexity of chemically reacting flows. During chemical reactions, the composition of the mixture changes over time and this fact appears in the term $\dot{\omega}_k$ in equation 2.17. In the case of combustion reactions, those changes in composition are associated with a positive *heat release*, hence the source[4] term $\dot{Q}_c$ in the energy equation. In the following, a

[4]It is important to point out that chemical reactions do not violate the conservation of energy: the source term reflects the **conversion of chemical energy** (enthalpy of formation, not included in the sum of sensible enthalpy and kinetic energy) **into total enthalpy**. Indeed, writing the energy equation in terms of the sum of total enthalpy and enthalpy of formation would make the source term $\dot{Q}_c$ vanish.

summary of the models adopted, along with the basic concepts needed to interpret the results, will be presented.

Scales Comparison

Generally speaking, we could state that, in nature, observable phenomena cover a wide variety of *scales*, separated by several orders of magnitude. This variety and complexity could be so dramatic that they could even overwhelm any attempt at a comprehensive multiscale model; this is, in fact, the rule rather than the exception. In such cases, a fruitful approach is to *compare the scales* at which different phenomena occur and, if possible, to find a way to describe them separately.

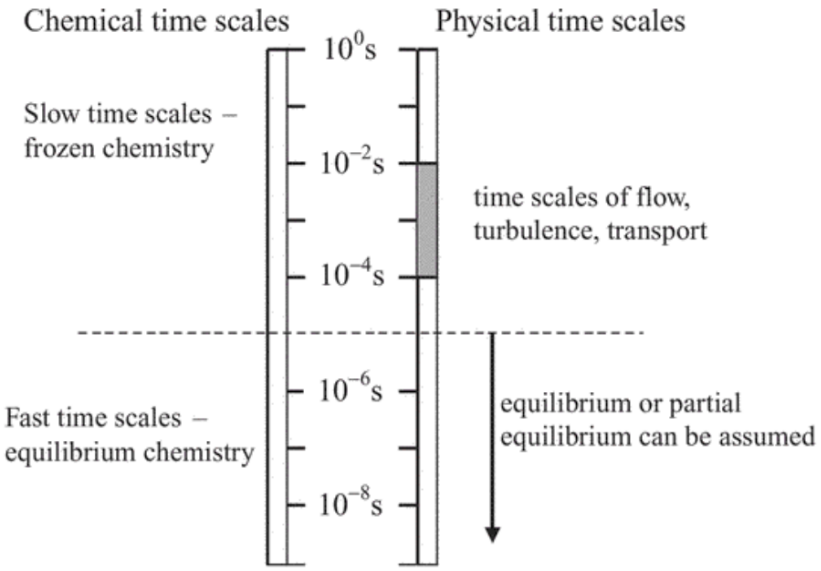

Fig. 2.4 Graphical comparison between the usual range of timescales found in both chemics and fluid dynamics, reported by [5].

Figure 2.4 offers a graphical representation of this method when applied to reacting flows. By looking closely at the left side of the picture, we encounter two different viable approaches, each governed by its simplifying assumption. First, imagine a contingent situation in which chemical reactions are evolving extremely fast if compared to the scales of the flow: in such a case, the two phenomena can be uncoupled and studied using different tools. Notice that assuming infinitely fast chemical reactions - a synonym to “equilibrium chemistry” - does not imply that the

composition does not change in time: many combustion reactions and flames are, in practical applications, modeled under the assumption of *local* chemical equilibrium.

On the other hand, consider a phenomenon in which chemical reactions are orders of magnitude slower than the physical time scale: in such a case, we could easily analyze the fluid-dynamic behavior without caring about the evolution of the chemical composition, which becomes a "constant property" of the fluid volume (from a Lagrangian point of view). This last framework is referred to as "frozen chemistry".

It is interesting to point out that in some applications those assumptions - though both inherently wrong - can be used in synergy to produce useful results. For instance, during the preliminary analysis of a rocket engine, it is common practice to assume equilibrium chemistry in the combustion chamber, and then perform a double equilibrium-frozen analysis of the thermodynamic and chemical state of the exhaust products as they expand in the nozzle. This gives insight into two extreme cases, narrowing down the uncertainty about the actual engine's performance. The NASA Glenn Research Center provides means to run such simple analysis with their web tool CEA (Chemical Equilibrium with Applications, see [19]).

The scale comparison is usually carried on with the help of two non-dimensional numbers: the Damkhöler number and the Karlovitz number. The former is hereby defined as:

$$Da_0 = \frac{\text{timescale of integral turbulence scale}}{\text{timescale of chemical reactions}} = \frac{\tau_0}{\tau_c}$$

whilst the latter is outlined by:

$$Ka = \frac{\text{timescale of chemical reactions}}{\text{timescale of the Kolmogorov scale}} = \frac{\tau_c}{\tau_k}$$

There are, in general, several ways of defining mixing and chemical time scales. For instance, a local mixing time scale can be defined using the definition of the filtered *scalar dissipation rate* proposed by De Bruyn Kops et al. in [20]:

$$\frac{1}{\tau_{mix}} = \widetilde{\chi} = \left(\frac{\widetilde{\nu}}{Pe} + \frac{\nu_t}{Sc_t}\right) \left|\boldsymbol{\nabla}\widetilde{Z}\right|^2 \tag{2.28}$$

This quantity implicitly incorporates the effects of diffusion and convection, and it can be considered a measure of departure from chemical equilibrium. Large values

of scalar dissipation rates are a synonym for strong mixture fraction gradient and enhanced mass and energy transfer through the stoichiometric contour. In most cases, the scalar dissipation rate is used as a parameter in the development of flamelet libraries for CFD computations, along with the mixture fraction Z. The interested reader is referred to [16] for a summary of the topic and further references.

In the present work, chemical reactions were not modeled using a flamelet-based approach; however, equation 2.28 was used in the post-processing of the results to estimate the local mixing timescale. Filtered momentum diffusivity of the mixture $\widetilde{\nu}$ was obtained after a mass-fraction weighted average of species viscosity (Sutherland's model), while the Peclet number was defined as $Pe = ReSc$. As pointed out by Saghafian et al. [21], the filtered scalar dissipation rate is rather insensitive to the choice of the reference length scale, due to the dominance of the turbulent term in ν_t/Sc_t with $Sc_t = 0.7$.

The filtered mixture fraction $\widetilde{Z}$ was computed using Bilger's definition found in [16], which is based on the fundamental fact that elements (C, O, H) are conserved during chemical reactions. With filtered species mass fraction fields available, mass fractions $\widetilde{Z}_j$ of chemical elements can be obtained using:

$$\widetilde{Z}_j = \sum_{i=1}^{N_s} \frac{a_{ij} W_j}{\mathscr{M}_i} \widetilde{Y}_i$$

where a_{ij} is an integer index quantifying the atoms of element j in specie i (e.g. $a_{H_2O,H} = 2$), W_j is the atomic weight of element j and $\mathscr{M}_i$ is the molecular weight of specie i. The mixture fraction is then computed with:

$$\widetilde{Z} = \frac{2\widetilde{Z}_C/W_C + \widetilde{Z}_H/2W_H - 2(\widetilde{Z}_O - Z_{O,ox})/W_O}{2Z_{C,fu}/W_C + Z_{H,fu}/2W_H + 2Z_{O,ox}/W_O} \tag{2.29}$$

Notice that the value of $\widetilde{Z}$ varies between 1 (pure fuel) and 0 (pure oxidizer).

2.1.4.1 Finite Rate Chemistry

In the previous section, it emerged how, sometimes, caring about the chemical equilibrium state without paying attention to the *kinetics* can be sufficient. This is true when the time scales of convection and diffusion are widely separated from that

of reaction, and the chemical kinetics parameters can be uncoupled and eliminated from the analysis.

However, there are cases in which this uncoupling is not possible. Consider a scenario in which the scales of the flow, turbulence, and transport are in the same ballpark as the scales of reaction, e.g. turbulent combustion in a scramjet engine. Here, not accounting for *how* equilibrium is pursued in the chemical space leads to errors that are not negligible. In fact, this becomes even more important when phenomena associated with the chemical reactions, e.g. exothermicity in combustion, prove themselves to have a strong influence on the fluid dynamics. An attempt to capture those non-trivial, coupled, time-dependent phenomena is to use *finite-rate chemistry*.

Using a similar notation to the one found in [16], consider a number N_s of species, denoted as M_k, involved simultaneously in m reversible chemical reactions:

$$\sum_{k=1}^{N_s} \nu'_{kj} M_k \rightleftharpoons \sum_{k=1}^{N_s} \nu''_{kj} M_k \quad \text{with} \quad j = 1, ..., m$$

For such a *reaction mechanism*, the rate of change in time of the molar concentration of specie k when involved reaction j, denoted with $\dot{q}_{kj}$, is given by:

$$\dot{q}_{kj} = \left(\frac{\mathrm{d}C_{M_k}}{\mathrm{d}t} \right)_j = (\nu''_{kj} - \nu'_{kj}) \left[k_f \prod_{k=1}^{N_s} (C_{M_k})^{\nu'_{kj}} - k_b \prod_{k=1}^{N_s} (C_{M_k})^{\nu''_{kj}} \right] \tag{2.30}$$

The meaning of equation 2.30 is the following: in a chemical reaction, how "fast" the concentration of a given specie changes depends on:

- $(\nu''_{kj} - \nu'_{kj})$: the difference between the stoichiometric coefficients of the specie in products and reactants, i.e. to which extent the specie is involved in the reaction. For example, if the specie is inert and $\nu''_{kj} = \nu'_{kj}$, then $\dot{q}_{kj} = 0$;
- C_{M_k} : the molar concentrations of the species involved in the reaction. Stemming from this term is the nonlinear dependence of the derivative of the variable on the variable itself: the chemical dynamic system is therefore modeled with a system of non-linear ODEs;

- k_f and k_b : the modified Arrhenius specific reaction rate constants for the forward and backward directions respectively, expressed as:

$$k_f = AT^{\beta} \exp\left\{ -\frac{T}{T_a} \right\} \tag{2.31}$$

where A is called *pre-exponential factor*, β is a semi-empirical coefficient and T_a is the temperature of activation, defined as $T_a = E_a/R_u$. Once k_f is known, k_b can be calculated if another parameter, the equilibrium constant, is given.

If we "look at the whole picture", the rate of change of C_k is obtained after combining the effects of the m reactions:

$$\dot{q}_k = \frac{\mathrm{d}C_{M_k}}{\mathrm{d}t} = \sum_{j=1}^{m} \dot{q}_{kj}$$

and the source terms of equations 2.16 and 2.17 are then obtained using:

$$\dot{Q}_c = \sum_{k=1}^{N_s} \Delta h_{f,k}^{0,m} \dot{q}_k \qquad \longrightarrow \tag{2.16}$$

$$\dot{\omega}_k = \mathscr{M}_k \dot{q}_k \qquad \longrightarrow \tag{2.17}$$

Before moving on, there are two aspects worth noting, without entering too much into the details. The former has to do with the non-linearity of the system of ODEs. When analyzing the terms appearing in equation 2.30, we noticed how non-linearity was introduced with the exponentiation of the molar concentrations with the stoichiometric factors on the left-hand side of the equation. This is not, however, the only source of non-linearity: the specific reaction rate constants, calculated with 2.31, clearly show a non-linear temperature dependence, and temperature itself is dependent on the chemical state via the energy equation 2.16. This, as it is intuitively clear, strongly couples the mass fraction fields and the thermodynamic variables fields, making the dynamics even richer.

The latter aspect - somehow linked to the former - is that the chemical dynamic system covers, in general, different timescales: in other words, not all reactions

happen at the same speed, causing the system to be a *stiff* one [22]. Integrating a dynamic system of this kind requires purposely designed numerical instruments, and it is something worth being aware of.

2.1.5 Fundamental Properties of Flammable Mixtures

The definitions of some of the fundamental properties of flammable mixtures will be briefly reported. Although not completely inherent to the mathematical modeling, those properties play a useful role in "compressing information" about the rich and complex dynamics of combustion reactions into intuitive and experimentally available values and are here reported as a reference.

Theoretical Adiabatic Flame Temperature

The definition of the theoretical adiabatic flame temperature is extremely simple: it is the maximum temperature reached by the combustion products in the ideal case of complete combustion, i.e. no thermal dissociation, and no heat loss across the boundaries of the reactor. It is important to point out that the *maximum* temperature is achieved with a nearly stoichiometric equivalence ratio ($\phi \approx 1$), and different values can be obtained depending on the constrained thermodynamic variable in the process (constant pressure, constant volume).

Knowledge of the AFT has the practical utility of providing a ceiling temperature value in constant pressure processes: this is extremely useful in the design phase.

Time of Ignition Delay

The time of ignition delay, commonly represented with the symbol τ_{ig}, in an experimentally determined parameter that quantifies the elapsed time between the triggering event and the reaction of a mixture of fuel and oxidizer. This parameter is usually measured in shock tube experiments: the traveling shockwave alters the thermodynamic state, putting the mixture in a non-equilibrium state from which the reaction mechanism develops. Sensors are used to collect time-dependent data, whence the time lag between the passage of the shock and the beginning of chemical activity can be quantified using different criteria, as Figure 2.5 shows.

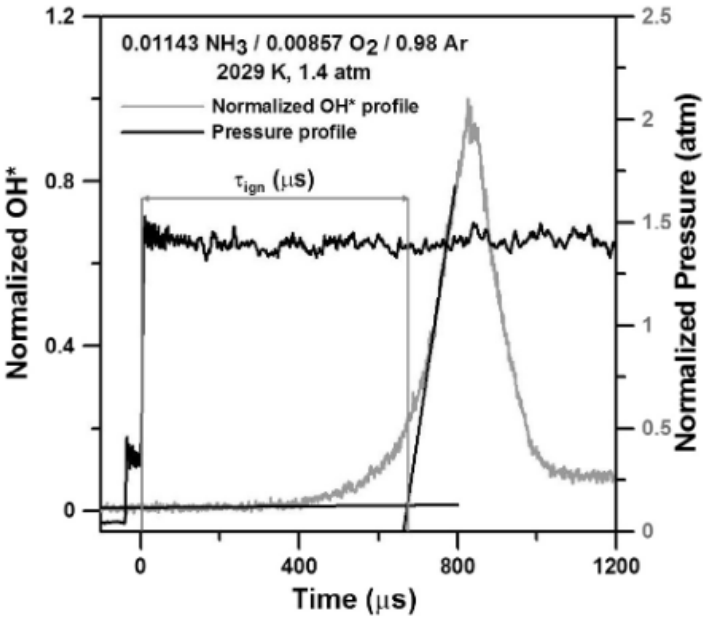

Fig. 2.5 Example of experimental profiles in a shocktube and determination of τ_{ig}, after [23].

This quantity, which usually varies with temperature, pressure, and equivalence ratio, is extremely insightful: for instance, it could be used to estimate the duration of ignition transients and other inherently unsteady phenomena. In addition to that, it is often used to validate chemical kinetics models, since it measures experimentally the reflection of the complex dynamics of the chemical system against its mathematical model. For further details, consult [23].

Laminar Flame Speed

The laminar flame speed is defined as the propagation of the flame front, measured in a reference frame in which the unburned mixture is quiescent, and it is usually marked with the symbol S_u. Just like the time of ignition delay, this property can be determined experimentally: among the standard experimental setups, there are counter-flow twin flames or conical flames [24]. The definition of S_u is not universal, and the literature is populated with several derivations and expressions, both theoretical and semi-empirical. Poinsot and Veynante summarize the most relevant in [13].

Just like the time of ignition delay, a lot about the reactivity, diffusivity, and exothermicity of the mixture - which are the driving factors for laminar flames - can

be discerned using laminar flame speed measurements. In addition to that S_u, as well as τ_{ig}, is a good benchmark for finite-rate chemistry models.

2.1.6 Turbulence and LES Modeling

To give a simple definition of turbulence is far from easy, and despite the vast amount of research and literature on the topic a lot of aspects of this fascinating phenomenon are still not understood. Keeping that in mind, the following section will give an overview of the basic concepts and features of turbulent flows following an intuitive - though maybe not utterly rigorous - path. Later, the focus will shift to more relevant aspects in the context of this work such as LES modeling. The interested reader could find more rigorous and detailed contents in the classic textbook *Turbulent Flows* by S. Pope [25] and in *Large Eddy Simulation for Incompressible Flows* by P. Sagaut [26].

The first, basic question one could ask about turbulence is: what does it actually be? Probably, no concise and thoroughly exact answer to the question exists, but one possible answer would be that:

> Turbulence is a flow feature characterized by **chaotic**, **multi-scale**, **hierarchical** processes involving coherent structures called *eddies*. After breaking down into smaller and smaller eddies, they finally dissipate the kinetic energy they have entrailed from the large-scale flow into heat, by means of diffusive phenomena.

It is clear that the definition above misses a lot of points, but one is particularly important: why does turbulence emerge? And what about the driving factors of the process? In an attempt to answer the first question, we can start with two keywords: **stability** and **bifurcation**. Generally speaking, stability is a property of a system's state in which small disturbances (of whatsoever nature) do not lead to changes in the long term. In certain phenomena, however, sensitivity to some sort of critical parameter utterly change this behavior. In those cases, bifurcative and chaotic features stem from our previously stable system, like in the popular example of the logistic map[5].

[5] https://en.wikipedia.org/wiki/Logistic_map

It was Osborne Reynolds in his pioneering work at the end of the nineteenth century who observed that, in the context of fluid dynamics, the critical parameter affecting the flow regime was the ratio between the scale of inertial forces and the scale of the viscous ones. After him, this similarity factor became known as the Reynolds number:

$$Re = \frac{\text{scale of inertial forces}}{\text{scale of viscous forces}} = \frac{\rho U L}{\mu}$$

When the Reynolds number is low, the dampening effect of viscous forces keeps the flow in a "stable", fairly predictable configuration: we are in the *laminar regime*. Increasing the Reynolds number, however, threatens this stability, and - after the so-called *transitional regime* - we find ourselves in the *turbulent regime*. Here inertial forces are dominant, and the flow is now highly chaotic, **fluctuating** and **unpredictable**. The energy transfer from the large scales to the small ones is established in a statistical sense, with eddies breaking down and taking the energy of their motion with them in what is known as the *energy cascade*. The energy spectrum in the wavelength space is reported in Figure 2.6.

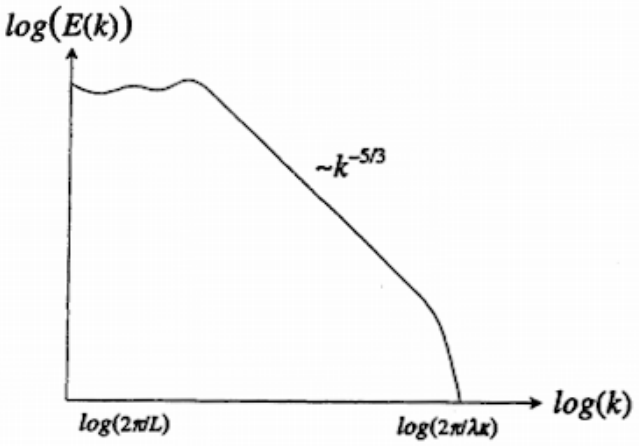

Fig. 2.6 Energy spectrum in the wavelength space, with Kolmogorov's "-5/3" law showing off in the inertial subrange. Image from [27].

How turbulence and the energy cascade can loom from the governing equations of fluid mechanics is still a question of open debate. In a recent article, Carbone and Bragg pointed out the relevance of the non-linear interaction of the strained field with itself (*strain self-amplification*) as a significant contributor to the energy cascade with the mechanism of *vortex stretching* - which has its physical foundations in the

conservation of angular momentum - also playing a crucial role [28]. Whatever the case, the bottom line is that non-linearity in the governing equations causes a laminar flow to develop into a turbulent flow as the Reynolds number is increased. Once turbulence is developed, energy is transferred from the integral, large scale to the so-called Kolmogorov scale (viscous subrange), where the Reynolds number based on the eddies size would be around unity. At this scale, diffusion dissipates energy into heat.

In the preceding, it was accentuated how turbulence is, physically speaking, a *multi-scale* phenomenon: in other words, there is "something happening" both slowly and fast, and both in the large and in the small. The governing equations would be able, in theory, to describe all these scales at once, since they reflect deep physical principles which are unviolated in fluid mechanics. Looking for a moment forward to the computational side of the matter, this is exactly what **direct numerical simulations** (DNS) do. However, their requirements in terms of spatial and temporal resolution - and consequent computational cost - make them inapplicable for practical purposes.

The first attempt to *model* turbulence was proposed by Osborne Reynolds: it consists in the decomposition of flow variables in a mean, time-averaged component and in a fluctuating one, with fluctuations being the manifestation of turbulence:

$$\phi(\mathbf{x},t) = \overline{\phi}(\mathbf{x}) + \phi'(\mathbf{x},t)$$

where the $\overline{\square}$ operator is the time average of the quantity:

$$\overline{\phi}(\mathbf{x}) = \frac{1}{\Delta t}\int_0^{\Delta t} \phi(\mathbf{x},t)\,\mathrm{d}t$$

After applying this decomposition, the governing equations are cast in terms of time-averaged quantities, and terms originating from the Reynolds decomposition are subject to modeling. This method, known as **Reynolds-Averaged Navier-Stokes** (RANS) , is well-known for its range of applicability and low computational cost, making it particularly appealing in industrial contexts. This lower cost, however, comes with lower information about the actual phenomenology of the flow. Indeed, modeling is carried out at every scale of the energy spectrum, and information about the time evolution is lost in the time averaging operation inherent to the Reynolds decomposition.

LES Modeling

A compromise in terms of computational cost/information content between DNS and RANS, **Large Eddies Simulations** (LES) are based on a spatial *filtering operation* that allows to separate the non-linear dynamics of larger eddies from the microscopic dissipation scale. The former is then resolved in its time-dependent evolution, whilst the latter is the target of compact models reflecting the more "universal" nature of smaller eddies.

In the physical space, the (linear) filtering operator is essentially the spatial convolution of a filter kernel $G(\mathbf{x},\mathbf{x}',\Delta)$ over the entire spatial domain:

$$\overline{\phi}(\mathbf{x},t) = \iiint_{-\infty}^{\infty} G(\mathbf{x},\mathbf{x}',\Delta)\phi(\mathbf{x},t)\,\mathrm{d}x_1'\,\mathrm{d}x_2'\,\mathrm{d}x_3'$$

where Δ is the so-called *filter cut-off width*. The filter kernel, or filter function, can have different definitions and it is normalized so that $\iiint_{\mathbb{R}^3} G(\mathbf{x},\mathbf{x}',\Delta)\,\mathrm{d}\mathbf{x}' = 1$. In many applications, the *top-hat* or *box* filter is used; it is defined in [16] as:

$$G(\mathbf{x},\mathbf{x}',\Delta) = \begin{cases} 1/\Delta^3 & \text{for} \quad |\mathbf{x}-\mathbf{x}'| \leq \Delta/2 \\ 0 & \text{for} \quad |\mathbf{x}-\mathbf{x}'| > \Delta/2 \end{cases}$$

at this point, the trick would be to apply the filtering operator to the governing equations 2.10, 2.15, 2.16, 2.17, recasting them in terms of filtered variables and modeling the extra terms rising from the decomposition of flow properties into resolved and unresolved spatial variations. However, in the particular context of compressible, reacting flows, even density is subjected to turbulent fluctuations whose effect on the flow may not be negligible at all. In order to reduce the population of statistical moments appearing in the equations, the so-called *Favre averaging* is introduced:

$$\widetilde{\phi} = \frac{\overline{\rho\phi}}{\overline{\rho}}$$

where the operator $\overline{\square}$ may represent the time averaging or the spatial filtering in the RANS and LES contexts respectively. Variables are therefore decomposed into a resolved, Favre-averaged components and fluctuating ones, which also accounts for

density fluctuations:

$$\phi = \widetilde{\phi} + \phi''$$

The reshaped governing equations, whose full derivation is omitted, are hereby reported in their compressible, reactive, LES formulation:

$$\begin{cases} \dfrac{\partial \overline{\rho}}{\partial t} + \boldsymbol{\nabla} \cdot (\overline{\rho}\widetilde{\mathbf{u}}) = 0 & \text{(2.10, LES)} \\ \dfrac{\partial \overline{\rho}\widetilde{\mathbf{u}}}{\partial t} + \boldsymbol{\nabla} \cdot (\overline{\rho}\widetilde{\mathbf{u}} \otimes \widetilde{\mathbf{u}}) = -\boldsymbol{\nabla}\overline{p} + \boldsymbol{\nabla} \cdot (\widetilde{\boldsymbol{\tau}} - \mathbf{B}) & \text{(2.15, LES)} \\ \dfrac{\partial \overline{\rho}\widetilde{E}}{\partial t} + \boldsymbol{\nabla} \cdot (\overline{\rho}\widetilde{\mathbf{u}}\widetilde{E}) = -\boldsymbol{\nabla} \cdot (\overline{p}\widetilde{\mathbf{u}}) + \boldsymbol{\nabla} \cdot (\widetilde{\boldsymbol{\tau}} \cdot \widetilde{\mathbf{u}}) - \boldsymbol{\nabla} \cdot \widetilde{\mathbf{q}}_\alpha + \overline{\dot{Q}}_c - \boldsymbol{\nabla} \cdot \mathbf{b}_\mathbf{E} & \text{(2.16, LES)} \\ \dfrac{\partial \overline{\rho}\widetilde{Y_k}}{\partial t} + \boldsymbol{\nabla} \cdot (\overline{\rho}\widetilde{\mathbf{u}}\widetilde{Y_k}) = -\boldsymbol{\nabla} \cdot \widetilde{\mathbf{j}}_k + \overline{\omega}_k - \boldsymbol{\nabla} \cdot \mathbf{b}_\mathbf{k} & \text{(2.17, LES)} \end{cases}$$

If we neglect the contributions of the subgrid scale to the consitutive equations - which is equivalent to using filtered quantities when computing $\overline{\boldsymbol{\tau}}$, $\overline{\mathbf{q}}_\alpha$, $\overline{\mathbf{j}}_k$ - the additional terms, emerging from the decomposition, appear in the form:

$$\mathbf{B} = \overline{\rho}\left(\widetilde{\mathbf{u} \otimes \mathbf{u}} - \widetilde{\mathbf{u}} \otimes \widetilde{\mathbf{u}}\right) : \text{subgrid stress tensor} \tag{2.32}$$

$$\mathbf{b}_\mathbf{E} = \overline{\rho}\left(\widetilde{\mathbf{u}E} - \widetilde{\mathbf{u}}\widetilde{E}\right) : \text{subgrid energy flux} \tag{2.33}$$

$$\mathbf{b}_\mathbf{k} = \overline{\rho}\left(\widetilde{\mathbf{u}Y_k} - \widetilde{\mathbf{u}}\widetilde{Y_k}\right) : \text{subgrid mass flux} \tag{2.34}$$

Those terms play a crucial role: the filtering operation and the reduction of the degrees of freedom destroyed information about the higher wavenumbers in the spectrum; this, however, is regained in an efficient way thanks to a variety of models, each with its range of applicability and advantages/drawbacks. A deep and extended treatise on the topic can be found in [26].

Generally speaking, subgrid[6] models can be classified into *functional* and *structural*, the difference being whether the closure aims to reproduce the energy cascade

[6]In this work, the concepts of *subgrid* scale and *unresolved* scale are used interchangeably, although the filtering operation does not necessarily require the presence of a grid (spatial discretization).

from the large to the small scales (former) or if its purpose is to fill the entries of the unresolved stress tensor (latter). In this work, the **One-Equation Eddy Viscosity Model** (OEEVM), which is classified as a functional model, has been adopted. The subgrid terms are defined by introducing the unresolved turbulent kinetic energy k and the kinematic eddy viscosity $\nu_k = C_k\sqrt{k}\Delta$, with a gradient diffusion assumption for unresolved fluxes:

$$\mathbf{B} \approx 2\overline{\rho}\left(\frac{1}{3}k\mathbf{I} - \nu_k\widetilde{\mathbf{D}}\right)$$

$$\mathbf{b_E} \approx -\overline{\rho}\frac{\nu_k}{Pr_t}\boldsymbol{\nabla}\widetilde{E}$$

$$\mathbf{b_i} \approx -\overline{\rho}\frac{\nu_k}{Sc_{t,i}}\boldsymbol{\nabla}\widetilde{Y_i}$$

Notice that the index has been changed in the unresolved diffusion term for $\widetilde{Y_k}$ in order to avoid ambiguity with turbulent kinetic energy. The model is then closed with an additional transport equation for the subgrid turbulent kinetic energy [29]:

$$\frac{\partial\overline{\rho}k}{\partial t} + \boldsymbol{\nabla}\cdot\overline{\rho}k\widetilde{\mathbf{u}} = \boldsymbol{\nabla}\cdot(\overline{\rho}(\overline{\nu}+\nu_k)\boldsymbol{\nabla}k) + \overline{\rho}\nu_k\mathbf{D}:\mathbf{E} - \frac{2}{3}\overline{\rho}k\boldsymbol{\nabla}\cdot\widetilde{\mathbf{u}} - C_\varepsilon\frac{\overline{\rho}k^{3/2}}{\Delta} \quad (2.35)$$

If we then find a way to relate C_k and C_ε to local flow properties - instead of assuming them as constants - we obtain the so-called “dynamic” OEEVM.

Wall Modeling for LES

When a viscous fluid interacts with a solid surface, i.e. a wall, it exchanges momentum with it. Under the continuum hypothesis and from a statistical point of view, the velocity of the infinitesimal fluid volume near the fluid-solid interface would be characterized by the so-called *no-slip condition* $\mathbf{u}|_w = \mathbf{0}$. There exists, therefore, a thin region of flow near the wall - known as *boundary layer* - where the velocity field changes rapidly (i.e. intense velocity gradients) from zero to a value “close enough” to $\mathbf{u_e}$, namely the velocity value of the flow unaffected by viscous interaction with the wall.

The turbulent flow near a wall is dominated by viscosity, and the boundary layer is an area of intense production and dissipation of turbulent kinetic energy. Legitimate scale segregation in this region would be difficult and trying to capture

the energy-containing structures, their interactions and the energy dissipation at the Kolmogorov scale (Wall Resolved LES, WRLES) would increase the computational cost dramatically.

On the other hand, it is well known from experimental observations that the velocity profile close to the wall - reported in Figure 2.7 - is nearly universal. Relying on this information it is possible to model the near-wall features without the need for fully resolving structures and gradients; instead, so-called *wall functions* are used in the computation of turbulent quantities near the wall.

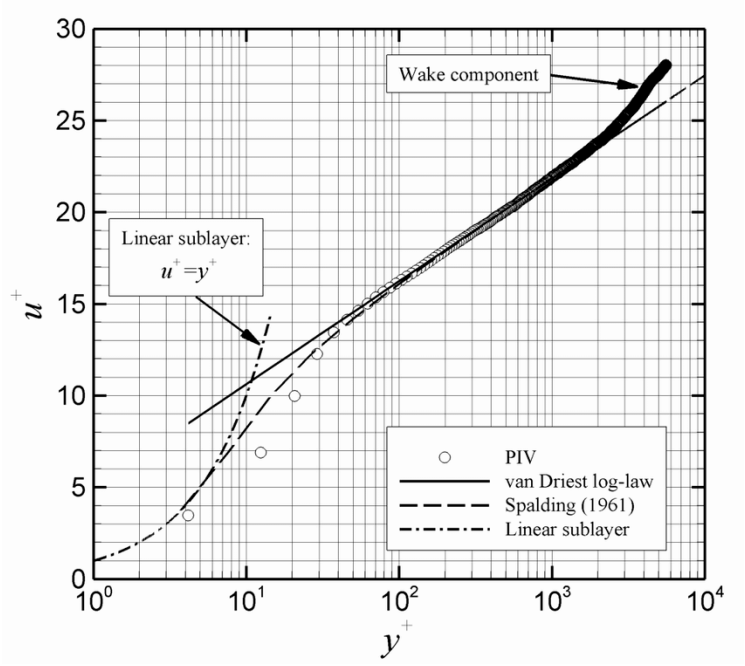

Fig. 2.7 The velocity profile near the wall, in wall variables $y^+ = u_\tau y/\nu_w$, $u^+ = u/u_\tau$, $u_\tau = \sqrt{\tau_w/\rho}$. Notice the linear viscous sublayer, the buffer layer and the logarithmic layer showing off. Picture from [30].

An example of this approach is the `nutkWallFunction` implemented in OpenFOAM [31] and used in this work. Here, turbulent viscosity in the logarithmic region is given by:

$$\nu_t = \nu_w \left(\frac{y^+ \kappa}{\log(E y^+)} - 1 \right) \quad \text{with} \quad y^+ = C_\mu^{1/4} y \frac{\sqrt{k}}{\nu_w}$$

where $\kappa = 0.41$, $E = 9.8$ and C_μ are empirically derived constants. A similar philosophy is adopted for the *thermal boundary layer*, modeling α_t and k with wall functions as well.

2.2 Numerical Aspects

The set of models presented in Section 2.1 can describe a continuous reality adopting mathematical objects called *fields*, which are governed by a set of differential equations and closures. Looking for analytical solutions works well for simple cases such as the Taylor-Couette flow; yet, for the general case, the proof of existence and smoothness of an analytical solution to the Navier-Stokes equations is still something that eludes mathematicians. Moreover, from the pragmatic, engineering perspective, dealing with the infinitely fine-grained information of fields and differential equations isn't necessary at all: these two factors have been, in the last decades, the main driver for the development of methods based on the *numerical solution* of the *discretized governing equations*. Figure 2.8 highlights the main "philosophical differences" between the world of continuous mathematical models and the discrete, computational world.

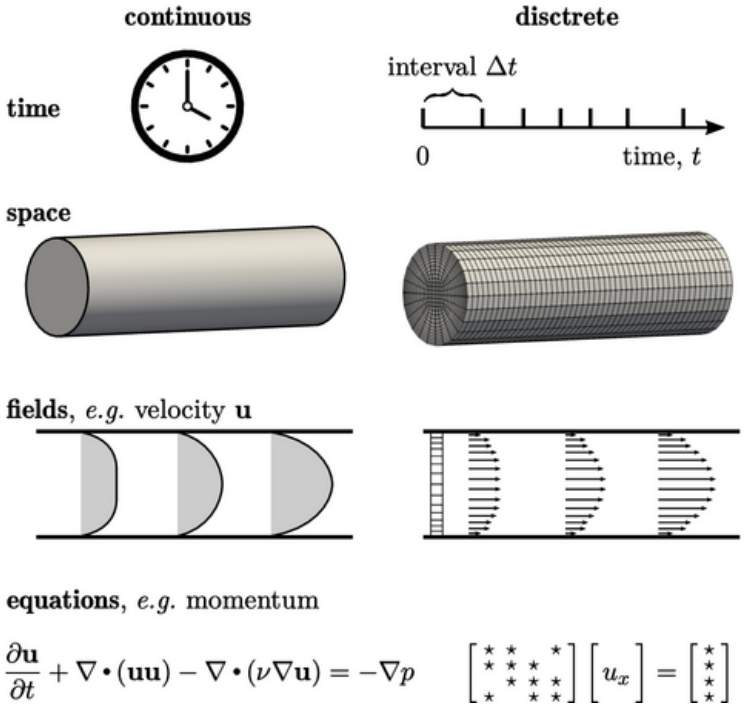

Fig. 2.8 When continuous space and time are discretized, the fine-grained information of the fields is reduced to a finite set of *numbers*, and the field equations are translated into *algebraic equations*. Image credits: [32]

2.2.1 The Finite Volume Method

In recent years, the **Finite Volume Method** (FVM) has been achieving increasing popularity thanks to its flexibility, ease of implementation and promisingly improving accuracy, and motivated by the availability of better and better hardware capable of handling its computational requirements.

Speaking about its top-level features, the FVM relies on a spatial discretization (a.k.a. computational grid, or mesh) to solve the governing equations in their integral, *conservative* form. A fundamental aspect of the method is the evaluation of discrete *fluxes* from previously stored information about the discrete fields (from previous timesteps, or initial conditions). These terms, along with *geometric information* about the mesh, are used to make the solution *march in time*, satisfying the (discrete algebraic) conservation law for each finite volume.

As it has already been mentioned, the starting point is the general transport equation 2.5, here reported for convenience:

$$\frac{\partial}{\partial t}\int_V \rho\phi \,\mathrm{d}V + \oint_{\partial V} \rho\phi\mathbf{u}\cdot\hat{\mathbf{n}}\,\mathrm{d}S = \oint_{\partial V} \rho\Gamma_\phi(\boldsymbol{\nabla}\phi)\cdot\hat{\mathbf{n}}\,\mathrm{d}S + \int_V S_\phi(\phi)\,\mathrm{d}V \tag{2.5}$$

Introducing a more compact notation, we can define:

$$\begin{aligned}
\mathbf{U} &= [\rho\phi]^T && : \text{conserved quantities vector}\\
\mathbf{F^C} &= [\rho\phi\,\mathbf{u}]^T && : \text{convective fluxes vector}\\
\mathbf{F^D} &= [\rho\Gamma_\phi\boldsymbol{\nabla}\phi]^T && : \text{diffusive fluxes vector}\\
\mathbf{Q} &= [S_\phi]^T && : \text{source terms vector}
\end{aligned}$$

where the elements of the vector are defined after adopting the contingent definitions of ϕ cited in 2.1, which allowed to specialize the transport equation to different flow properties. We then introduce the notion of *cell average* over a finite volume V_P, and we approximate the integrals of the flux terms with a sum of *uniform fluxes* crossing the planar faces of the *polygonal* finite volume:

$$\mathbf{U_P} = \frac{1}{V_P}\int_{V_P}\mathbf{U}\,\mathrm{d}V \quad ; \quad \mathbf{Q_P} = \frac{1}{V_P}\int_{V_P}\mathbf{Q}\,\mathrm{d}V$$

$$\oint_{\partial V_P} \mathbf{F}^{\square} \cdot \hat{\mathbf{n}} \, \mathrm{d}S \approx \sum_{faces} \mathbf{F}^{\square}{}_{\boldsymbol{f}} \cdot \mathbf{S}_{\boldsymbol{f}}$$

where the subscript **P** is used to emphasize the fact information about cell averages is stored in the centroid of the finite volume. In general, $\mathbf{F}^{\mathbf{C}}$, $\mathbf{F}^{\mathbf{D}}$ and **Q** are a function of the conserved quantities **U**. After some substitutions we obtain:

$$\frac{\partial \mathbf{U_P}}{\partial t} + \frac{1}{V_P} \sum_{faces} \left[\mathbf{S}_{\boldsymbol{f}} \cdot \mathbf{F}^{\mathbf{C}}(\mathbf{U}) - \mathbf{S}_{\boldsymbol{f}} \cdot \mathbf{F}^{\mathbf{D}}(\mathbf{U}) \right] = \mathbf{Q_P}(\mathbf{U}) \tag{2.36}$$

Equation 2.36 is also known as the *semi-discrete* form of the governing equations: space is treated as a discrete entity, but time is still represented by a continuum. It is important to point out that the discussion in the preceding of this section has been carried on from the general conservation law, before any filtering or time-averaging operation. Nevertheless, the compact semi-discrete notation used in 2.36 can be successfully applied to the compressible, reactive, LES formulation of the governing equations presented in Section 2.1.6.

At this point, a wide variety of methods and techniques exists to construct convective and diffusive fluxes, solve the algebraic systems of equations and integrate the solution in time. Giving a comprehensive overview of all this diversity - which is where the flexibility of the FVM resides - is undoubtedly not in the scope of the present work: the interested reader is referred to [16] for an introductory overview of the topic. Nevertheless, the next section will be devoted to a brief overview of the methods chosen in the context of this study.

2.2.2 Solvers and High-Resolution Central Scheme

The numerical investigation of supersonic, reacting flows poses interesting challenges inherently related to their peculiar phenomenology. As a matter of fact, they are characterized by large gradients (e.g., shockwaves and flame fronts), wave propagation and coalescence, strong non-linear interactions, and so on. All these features influence the choice of the numerical methods one should adopt in an attempt to simulate this complex class of phenomena. As a good practice, the scheme should be at least second-order accurate in space, and able to capture sharp gradients and discontinuities. Numerical diffusivity needs to be kept in the proper range so that the scheme is neither too diffusive nor unstable.

The solvers used in the work are `rhoCentralFoam` and `rhoCentralTurbReactingFoam`[7], part of the open source C++ platform OpenFOAM. Both the solvers are density-based and built upon the high-resolution central scheme by Kurganov and Tadmor (KT), presented for the first time by the authors in [33].

Extending the basic ideas beyond the celebrated Lax-Friedrichs (LxF) scheme and its natural extension, the Nessyahu-Tadmor (NT) scheme, the KT uses a piece-wise linear reconstruction to estimate the interface values of the conserved quantity. After that, local propagation speed is estimated and approximate integration is performed over smooth and non-smooth regions, with the non-smooth region being centered at the interface between the cells, and determined by the local propagation speed and by the finite timestep Δt. In the end, a second piece-wise linear reconstruction is performed - obtaining values that can be stored in the original grid again. A schematic overview of the process in a canonical 1D case is reported in Figure 2.9; more information about the scheme and its implementation in the CFD tool can be found in the reference article, in the source code [34] and in the academic article by the authors of the solver [35].

The scheme is relatively easy to implement and does not rely on the solution of local Riemann problems for the determination of fluxes; accuracy is second order in space, and dissipation is considerably lower than in the LxF and NT cases. In addition to that, the scheme shows total variation diminishing (TVD) properties, making it highly accurate, efficient, and robust.

2.2.3 Interpolation Schemes

The reconstruction of fluxes at the basis of high order numerical schemes relies on the *interpolated* values of the conserved quantity at the center of the interfaces between finite volumes, given a discretized field ϕ in one-to-one correspondence with the set of centroids' coordinates.

The numerical setup adopted in this work exploits the *Van Leer* limited slope scheme for the extrapolation of face values. This method evaluates the ratio of

[7] Result of the hybridation between `rhoCentralFoam` and `reactingFoam` with effects of turbulence-combustion interaction included.

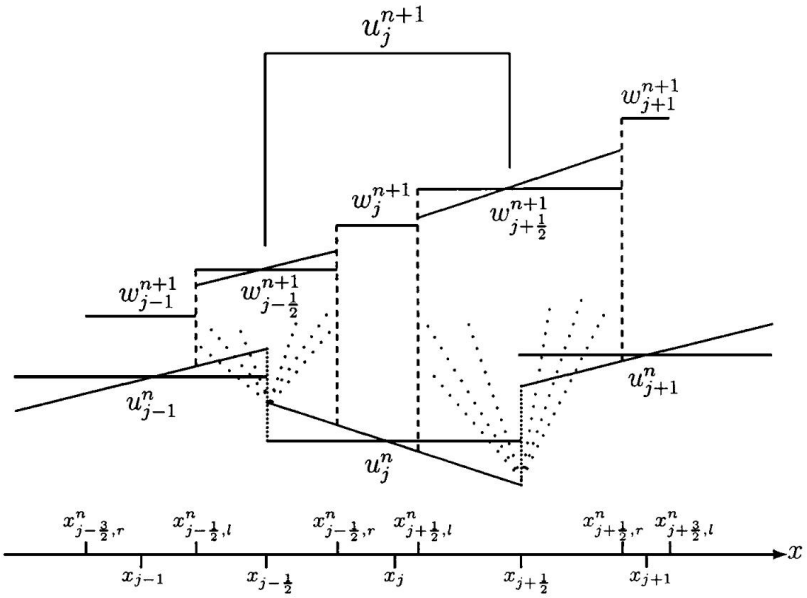

Fig. 2.9 Schematic overview of the Kurganov-Tadmor central difference scheme. First, cell values are used to linearly reconstruct the interface values; the local finite speed of propagation is then estimated and integration is approximated separately over smooth and non-smooth regions. Piece-wise linear reconstruction is then performed to obtain evolved values which can then be put in one-to-one correspondence with the original spatial discretization. Image from [33].

successive gradients r using information from neighbor cells:

$$r = \max\left(2\frac{\boldsymbol{\Delta d}\cdot\boldsymbol{\nabla}\phi}{|\boldsymbol{\Delta d}|\boldsymbol{\nabla}_n\phi_f} - 1, 0\right)$$

where $\boldsymbol{\nabla}\phi$ is estimated using the gradient scheme and the surface normal gradient $\boldsymbol{\nabla}_n\phi_f$ is obtained after a non-orthogonal correction (see 2.2.4).

The limiter function is given by [36]:

$$\beta(r) = \frac{r+|r|}{1+|r|}$$

and the interpolated value is obtained using:

$$\phi_f = \beta\phi_L + (1-\beta)\phi_U$$

where ϕ_L and ϕ_U represent values obtained with linear and upwind interpolation respectively.

2.2.4 Gradient Schemes

Generally speaking, the gradient of a scalar field ϕ is a vector containing the derivatives of the field in each spatial dimension, and it is obtained from the field $\phi(x,y,z)$ after applying of the $\boldsymbol{\nabla}$ operator:

$$\boldsymbol{\nabla} = \frac{\partial}{\partial x}\hat{\mathbf{i}} + \frac{\partial}{\partial y}\hat{\mathbf{j}} + \frac{\partial}{\partial z}\hat{\mathbf{k}}$$

Clearly, the gradient is a differential operator, related to the concept of "continuity". In the context of discrete numerical analysis, a way to discretize this operator must be found. Fortunately *Gauss' theorem*, one of the fundamental theorems in calculus, provides a useful way to approximate the gradient by means of:

$$\int_V \boldsymbol{\nabla}\phi \, \mathrm{d}V = \int_{\partial V} \phi \hat{\mathbf{n}} \, \mathrm{d}S \approx V\boldsymbol{\nabla}\phi \longrightarrow (\boldsymbol{\nabla}\phi)_P \approx \frac{1}{V_P}\sum_{faces} \phi_f \mathbf{S_f} \tag{2.37}$$

Notice that equation 2.37 involves the elaboration of geometric information (i.e. V_P and $\mathbf{S_f}$) and extrapolated field values at interfaces, ϕ_f. While the former is known once the computational grid has been generated, interface values need to be extrapolated starting from cell values. In this work, *linear interpolation* has been involved in the gradient terms discretization. At the interface between the current cell P and a neighbor cell N, the value of the scalar field ϕ_f is given by:

$$\phi_f = w\phi_P + (1-w)\phi_N$$

where w is a weighting term defined in 2.38 using geometric information about the face orientation and relative position of the cells' and faces' centroids; Figure 2.10 reports a graphical representation of the setup.

$$w = \frac{\hat{\mathbf{n}} \cdot \boldsymbol{d_N}}{\hat{\mathbf{n}} \cdot (\boldsymbol{d_N} + \boldsymbol{d_P})} \tag{2.38}$$

When the surface normal gradient $\boldsymbol{\nabla_n}\phi_f$ is desired, a *non-orthogonality correction* is performed. As it will be later displayed, the computational grid has been obtained using a block mesher and hexahedral cells; this allowed for a rather low average non-orthogonality and good quality metrics. However, to increase stability

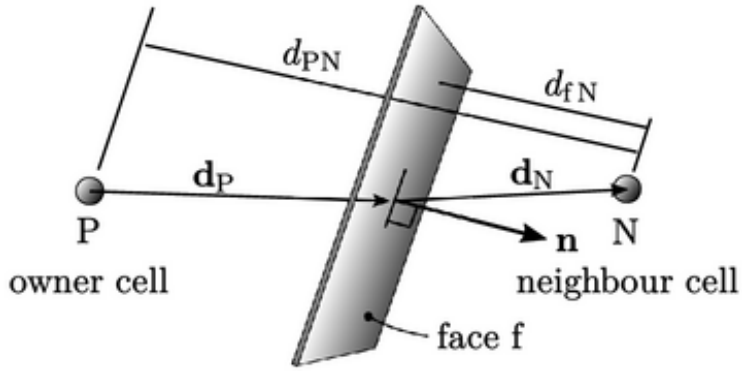

Fig. 2.10 Linear interpolation at the interface between current cell P and neighbor cell N. Image credits go to [32].

and accuracy in localized areas of non-orthogonal cells, the correction has been turned on.

Following [32], the normal component is evaluated as the combination of an implicitly computed orthogonal component:

$$\nabla_{\boldsymbol{n}}\phi_f^{orth} = C_\Delta^{corr}(\phi_N - \phi_P) \text{ where } C_\Delta^{corr} := \frac{1}{\hat{\mathbf{n}} \cdot \boldsymbol{\Delta d}}$$

and an explicitly computed correction term, where $(\nabla\phi)_f$ is obtained after interpolation of known cell gradients $(\nabla\phi)_P$ and $(\nabla\phi)_N$:

$$\nabla_{\boldsymbol{n}}\phi_f^{corr} = (\hat{\mathbf{n}} - C_\Delta^{corr}\boldsymbol{\Delta d}) \cdot (\nabla\phi)_f$$

Combining the two contributions leads to:

$$\nabla_{\boldsymbol{n}}\phi_f = C_\Delta^{corr}(\phi_N - \phi_P) + (\hat{\mathbf{n}} - C_\Delta^{corr}\boldsymbol{\Delta d}) \cdot (\nabla\phi)_f \tag{2.39}$$

2.2.5 Divergence Schemes

The general conservation equation incorporates the so-called *convective term* (see equation 2.2), which physically represents the contribution to the total balance given by convection/advection phenomena. In differential terms, it is represented by the

divergence operator, defined for a generic vector field $\boldsymbol{\psi} = [\psi_x \ \psi_y \ \psi_z]^T$ as:

$$\boldsymbol{\nabla} \cdot \boldsymbol{\psi} = \frac{\partial \psi_x}{\partial x} + \frac{\partial \psi_y}{\partial y} + \frac{\partial \psi_z}{\partial z}$$

When stepping into the realm of the discrete, the divergence operator is approximated - as for the gradient operator - using *Gauss' theorem*; see 2.40.

$$\int_V \boldsymbol{\nabla} \cdot \boldsymbol{\psi} \, \mathrm{d}V = \int_{\partial V} \boldsymbol{\psi} \cdot \hat{\mathbf{n}} \, \mathrm{d}S \approx V \boldsymbol{\nabla} \cdot \boldsymbol{\psi} \longrightarrow (\boldsymbol{\nabla} \cdot \boldsymbol{\psi})_P \approx \frac{1}{V_P} \sum_{faces} \boldsymbol{\psi_f} \cdot \mathbf{S_f} = \frac{1}{V_P} \sum_{faces} F \phi_f \tag{2.40}$$

In the canonical transport equation, $\boldsymbol{\psi_f} \coloneqq (\rho \, \mathbf{u})_f \phi_f$ and $F \coloneqq (\rho \, \mathbf{u})_f \cdot \mathbf{S_f}$.

As in Section 2.2.4, information involved in 2.40 has a double nature: geometric and stemming from interpolation. For the second one, a wide variety of techniques are implemented in the OpenFOAM package [37]. In the present work the term F is computed after interpolation of ρ and $\mathbf{u}$ is performed using the VanLeer TVD interpolation scheme from Section 2.2.3. Face values of the conserved quantity ϕ_f are then evaluated using `linear` and `limitedLinear 0.25` schemes.

In particular, `limitedLinear 0.25` has been adopted for turbulent kinetic energy k, and for species mass fraction Y_k and h. The rationale has been to increase numeric diffusion and boundedness in areas of large gradients, thus avoiding non-physical values and oscillations typical of the linear scheme which on the other hand is adopted elsewhere. As reported in the source code [38], the limiter is in the form:

$$\beta(r) = \max\left(\min\left(\frac{2}{\kappa} r, 1\right), 0\right) \text{ where } \kappa = 0.25$$

Low values of r make the scheme's "behavior" more similar to that of the upwind scheme (diffusive and stable), and since β is inherently limited to 1 the discretization scheme is robust enough for practical applications.

2.2.6 Laplacian Schemes

Another differential operator appearing in 2.6 is the Laplace operator. For a generic scalar field ψ, it is defined as the divergence of the gradient of the aforementioned

field. It can be written in cartesian coordinates as it follows:

$$\nabla^2\psi := \boldsymbol{\nabla}\cdot\boldsymbol{\nabla}\psi = \frac{\partial^2\psi}{\partial x^2} + \frac{\partial^2\psi}{\partial y^2} + \frac{\partial^2\psi}{\partial z^2}$$

This operator appears in the governing equations when modeling diffusive terms under the assumption of gradient diffusion (Fickian mass diffusion, Newtonian fluid, Fourier's law). In that case, the term appears in the form $\boldsymbol{\nabla}\cdot(\Gamma_\phi\boldsymbol{\nabla}\phi)$, where Γ_ϕ is the diffusion coefficient for property ϕ and is not considered constant.

Gauss' theorem is again adopted in the discretization. In particular:

$$\int_V \boldsymbol{\nabla}\cdot(\Gamma_\phi\boldsymbol{\nabla}\phi)\,\mathrm{d}V = \int_{\partial V}\Gamma_\phi\boldsymbol{\nabla}\phi\cdot\hat{\mathbf{n}}\,\mathrm{d}S \longrightarrow \boldsymbol{\nabla}\cdot(\Gamma_\phi\boldsymbol{\nabla}\phi)_P \approx \frac{1}{V_P}\sum_{faces}\Gamma_{\phi,f}\left\|\mathbf{S_f}\right\|\boldsymbol{\nabla_n}\phi_f \tag{2.41}$$

At this point, `linear` interpolation scheme is used to obtain face values of the diffusion coefficient $\Gamma_{\phi,f}$, and the non-orthogonality correction described in Section 2.2.4 is applied in the estimation of the surface normal face gradient $\boldsymbol{\nabla_n}\phi_f$.

2.2.7 Temporal Discretisation and Solution

After the equations have been discretized in space and the proper initial and boundary conditions have been assigned, the time-history is obtained by making the state of the system *discretely march in time*. We start from the semi-discrete compact form of the governing equations (equation 2.36) and write the time derivative using, for instance, a forward finite difference in time:

$$\frac{\mathbf{U_P}^{n+1} - \mathbf{U_P}^{n}}{\Delta t} + \frac{1}{V_P}\sum_{faces}\left[\mathbf{S_f}\cdot\mathbf{F^C}(\mathbf{U}) - \mathbf{S_f}\cdot\mathbf{F^D}(\mathbf{U})\right] = \mathbf{Q_P}(\mathbf{U}) \tag{2.42}$$

The $\mathbf{U}$ involved in the construction of fluxes and source terms can come from timestep t^n or t^{n+1}. This makes a big practical difference, marking the contrast between *explicit* and *implicit* methods. Both the approaches have advantages and disadvantages and they have been scrupulously compared in the latest decades, with implicit methods becoming increasingly popular in general-purpose CFD applications. The reason for that lies in their *stability*.

Implicit Approach

It is clear that for an implicit method the state variables vector for volume P and time t^{n+1} - namely $\mathbf{U_P}^{n+1}$ - depends not only on the state at the previous timestep t^n, but also on the unknown $\mathbf{U_N}^{n+1}$, where subscript N represents a generic neighbor cell. On its turn, $\mathbf{U_N}^{n+1}$ depends on the value of the state vector for volume N at timestep t^n, and also on the value of $\mathbf{U}$ at t^{n+1} for all the neighbors of cell N. Confusing as it may sound, if we think about the so-called *domain of dependence* of each point of the grid at t^{n+1} in discrete space-time, we observe that the solution is influenced by information stored in every point at t^n, and therefore by the whole chronological evolution. This has important consequences: the unsteady governing equations belong to the class of hyperbolic PDEs, and signals run along characteristic lines in the direction of increasing time. The fact that the domain of dependence of each point at t^{n+1} always contains all the characteristics coming from previous times - regardless of the Δt adopted in the temporal discretization - is the key physical explanation of the stability of these methods. It is necessary to point out that Δt is nonetheless limited by considerations about the truncation error in the Taylor expansion; in addition to that, we should remember that satisfying the CFL requirement is a necessary, but not sufficient condition for stability.

From an implementation standpoint, the stability of implicit methods comes at a cost: to get $\mathbf{U_j}^{n+1}$ everywhere on the grid, huge linear systems of equations need to be solved - a task that may result in a computational nightmare. The approximate solution for each system is sought with the help of iterative algorithms, e.g. the well-known Gauss-Seidel and descent methods. Solution algorithms (e.g. PISO, PIMPLE) are adopted to ensure that the approximate solution of each discretized governing equation reflects the inherent coupling between them. See [16] for further information.

Explicit Approach

Thanks to the increasing availability of computational power and the advancements in parallel computing, explicit methods have been gaining a new wave of interest in recent years. When accessible information is used to calculate fluxes and source terms in 2.42 (i.e. $\mathbf{U} \coloneqq \mathbf{U}^n$), each discretized algebraic equation for each finite volume is uncoupled from all the other ones. The resulting matrices have a diagonal

structure and, when distributing computation over several processing units, this translates into a reduced amount of information exchanged between interfaces of the decomposed parameters. The practical advantage is a better *scalability* of the solver.

A drawback of this approach is the limit posed by its *conditional stability*. As discussed above, the *computational* domain of dependence - determined by the local geometry of the spatial grid and by the timestep Δt - must include the *physical* one for the computation to be stable (i.e. errors amplitude not being amplified). As long as the time step is small enough, physical characteristic lines from previous times are part of the computational domain of dependence, hence the scheme is in its region of stability. However, for greater values of Δt, the (physical) solution would be influenced by information coming from regions outside the computational domain of dependence, and therefore not involved in the computation. This "mismatch" between physics and numerics is - broadly speaking - what causes the instability of explicit methods for large Δt. For an explicit scheme to be stable, the so-called **Courant–Friedrichs–Lewy** condition must be satisfied:

$$(Co)_{max} = 0.5 \max \left(\frac{\sum_{faces} (a_{max} S_f)}{V} \Delta t \right) < 1 \tag{2.43}$$

where Co is the Courant number as commonly defined in the context of central differencing for compressible flow and a_{max} is the maximum local propagation speed of information along characteristic lines, defined at every face of the finite volume. Equation 2.43 is implemented in the solvers `rhoCentralFoam` and `rhoCentralTurbReactingFoam`, see [39]. In many other applications, the Courant number can be defined using the local advection speed.

In the present work, *explicit* time integration with a first order accurate Euler method (as presented in 2.42) is utilized to solve the inviscid conservation equations for ρ, $\rho \mathbf{u}$ and ρE; diffusion corrections for both momentum and energy are introduced semi-implicitly in order to avoid excessive timestep limitations. The solution algorithm for `rhoCentralFoam` is reported in reference [35].

As far as the species mass fraction equations are concerned, a similar approach to the one used in `reactingFoam` [40] is adopted in `rhoCentralTurbReactingFoam`, with some differences in the treatment of Fickian and turbulent diffusion. The implementation exploits the chemistry's inherent stiffness (see 2.1.4.1) introducing

a splitting of the operators. To cut the story short: using the dynamic model based on the Arrhenius closure provided by the reaction mechanism, for each iteration the reaction rates are computed starting from the current state of the system. After that, the transport equations for species mass fractions are solved using the previously computed reaction rates.

From a practical perspective, the `diagonal` solver implemented in OpenFOAM has been used for the explicitly computed terms; diffusivity corrections and reacting flow equations (i.e. species concentration) have been solved iteratively using the Gauss-Seidel algorithm. The stiff system of ODEs modeling the chemistry - built upon the Z66 reaction mechanism for ethylene-air [41] - is integrated using the `rodas23` solver.

2.3 The HIFiRE Program

An example of fruitful, international collaboration between the United States Air Force Research Lab (AFRL), NASA, the Australian Defence Science and Technology Organization (DSTO), Boeing, and the University of Queensland, the HIFiRE program has the aim of accelerating the progress of science and technology of hypersonic flight.

The program was arranged in 2006, in a period when computational models and predictive tools in different disciplines - e.g. aerothermodynamics, propulsion, and thermal management - did not satisfy the necessary accuracy for the design of a practical hypersonic system. Moreover, ground test facilities had - and still have - the reputation of limited capabilities, and flight testing can result in a considerable economic effort. Indeed, among the goals of the program was the establishment of a money-efficient, fast and low-risk testing methodology; the key factors were a collaboration between the actors, and a careful combination of modeling, ground testing, and flight testing. The collected experimental data would then have been used to extract useful information and in the development of new models, as well as a validation bench for the available ones. The HIFiRE program schedule involved nine research projects, each focusing on different critical aspects along the whole pipeline, from modeling to flight testing. More general information about the program can be found in [42].

2.3.1 The HIFiRE 2 Experiment

As mentioned in Section 1.2, hypersonic vehicles would dramatically benefit from an air-breathing propulsion system, in which combustion involves atmospheric oxygen; this increases by a lot the specific impulse of the engine if we compare it, for instance, to the rocket engine (see Figure 1.7). Such a system has been identified in the ramjet-based engine family, whose family the ramjet and the scramjet are part. However, the physics and operating principles of those machines are not completely clear, and both predictive analysis and ground testing seldom succeed in finding the answers to the many questions. This is the area the HIFiRE 2 experiment purposed to give a contribution.

	Flight Experiment	**Research Objectives**
Primary	Inward turning, 2-dimensional hydrocarbon fueled scramjet combustor flowpath	**Primary Objectives** • Evaluate combustor performance and operability through dual-mode to scramjet-mode transition • Demonstrate Mach 8 combustion performance at $\phi_B \geq 0.7$ using a hydrocarbon fuel (Figure 2) **Secondary Objectives** • Evaluate a gaseous bi-component fuel mixture as a surrogate for a cracked liquid hydrocarbon fuel • Validate existing design tools for scramjet inlet, isolator, combustor, and nozzle components
Secondary	Tunable diode-laser absorption spectroscopy (TDLAS) system	• Acquire high-fidelity temporal and spatial core-flow measurements of combustion products (water) in a scramjet operating environment through Mach 8 flight conditions

Fig. 2.11 HIFiRE 2 experiments' objectives. The primary flight experiment, investigating the combustor flowpath, was intended to provide research objectives with different priorities. The test flight also carried a secondary optical measurement experiment named TDLAS, with the aim of getting a better know-how about non-intrusive diagnostic techniques. Table from reference [43].

As reported in Figure 2.11, the initial requirements included a planar configuration and the usage of a hydrocarbon gaseous fuel. The rationale beyond those requisites was that, from a broader perspective, planar configurations are better suited for engine-airframe integration. Hydrocarbon gaseous fuels have been extensively studied in the context of scramjet engines; they show high energy volumetric density in their condensed phase and discrete cooling capabilities. After being used as a coolant fluid, the hydrocarbon fuel undergoes endothermal cracking and a phase change, transforming into a gaseous mixture of lighter hydrocarbons which is then burned in the combustor.

Concerning the research objectives, two are the paramount keywords: *operability* and *performance*. A necessary condition for a propulsion system to be operable is its

ability to provide satisfactory functionality (i.e. produce thrust) under a prescribed set of flight conditions. To widen the range of operational flight Mach numbers, the design team proposed the flow path of Figure 2.12

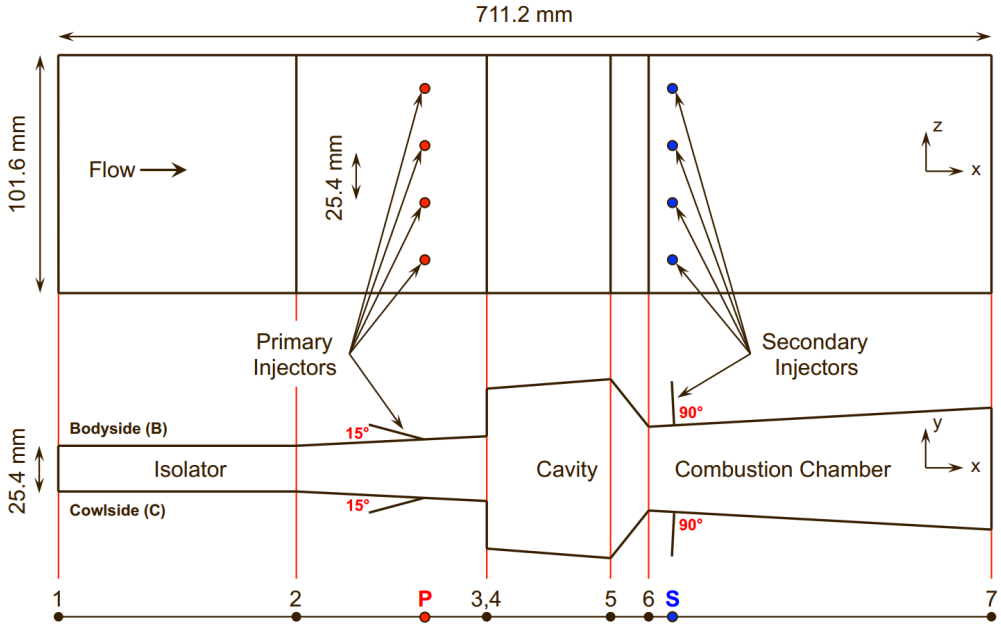

Fig. 2.12 HIFiRE 2 geometric layout after the modifications from the original AFRL configuration. The isolator, the two injection zones (P1 and S1), the cavity and the combustor are represented. The transversal length at the isolator entrance is 25.4 mm, while stream-wise and span-wise lengths are respectively 711 mm and 101.6 mm. The whole 3D configuration can be represented as the repetition in the span-wise direction of four 25.4 mm wide units (each with two pairs of injectors at P1 and S1, whose diameter is respectively $d_{P1} = 3.175$ mm and $d_{S1} = 2.388$ mm). The lower and upper walls have been arbitrarily marked "cowl" side and "body" side respectively. Schematic not in scale. Image credits go to [44].

An outgrowth of previous research conducted at the AFRL [45], the HIFiRE 2 combustor flow path has been conceived to work in a Mach number range of approximately 5.5 to 8.5; during the mission, the transition from *dual-mode* operation to pure *scramjet* was intended to be achieved thanks to the acceleration of the vehicle in the 2-σ-constant dynamic pressure mission corridor. The main features of these two different operational modes are hereby reported:

- **dual-mode**: this working regime is characterized by two key peculiarities. The former is the presence of *areas of subsonic* flow near the cavity region. Strong recirculating structures emerge in the cavity resulting in areas of locally subsonic flow; the one-dimensional Mach number would drop below one

as well. High temperature and pressure in the low-Mach cavity region are linked with the latter trait: the presence of a *shocktrain in the isolator*, which manifests itself through intense pressure gradients adjusting the pressure level to that of the cavity region.

- **pure scramjet**: this regime, typical of higher speeds, is characterized by a supersonic one-dimensional Mach number distribution along the whole flow path, and by the absence of the shock train in the isolator.

These definitions, though not particularly "quantitative", are commonplace in the cavity-stabilized scramjets literature and are reported in [5], too. It is important to highlight that transition between these two modes can also be obtained through different fuel injection splitting between injection zones. The effects of this extra degree of freedom on operability, performance, and safety has been parametrically studied in [46] through ground testing. For more general information about the flight experiment and its development, the reader is referred to [43][45][1][47].

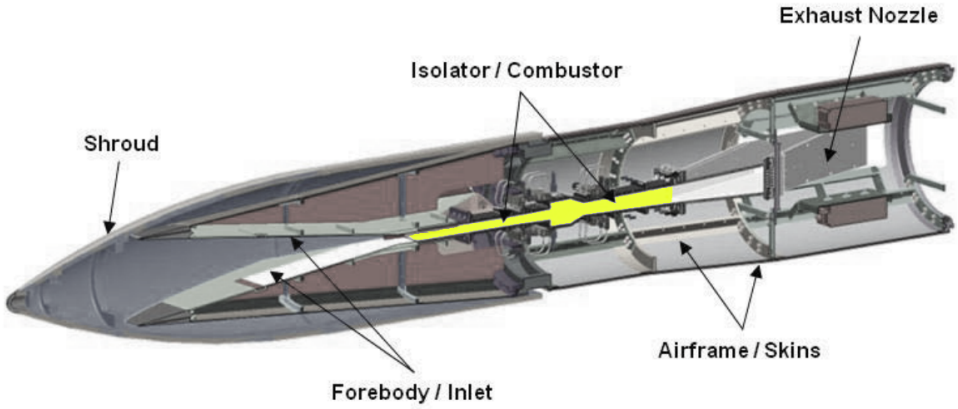

Fig. 2.13 Cutaway representation of the HIFiRE2 flight vehicle from [43]; highlighted, the isolator/combustor assembly.

A conceptual representation of the combustor as integrated into the flight vehicle is represented in Figure 2.13. The flight payload was designed to be installed on the top of an off-the-shelf sounding rocket which had the task of bringing it to the entrance of the mission corridor. This approach to FASTT (Freeflight Atmospheric Scramjet Test Technique) was used in the HIFiRE program to reduce costs. However, this resulted in some design compromises such as the unusual (and sub-optimal) shape of the nozzle, designed to avoid the plume damaging the rest of the stack.

2.3.2 The HDCR Ground Experiment

Before actual flight testing, a ground-based experimental campaign had been carried on to explore different fuel injection configurations and collect pressure, temperature, and heat transfer data along the combustor. Flight test data are often noisy and difficult to interpret, and among the goals of the ground tests was the collection of a cleaner data-set for further comparison with real environment data and predictive CFD results.

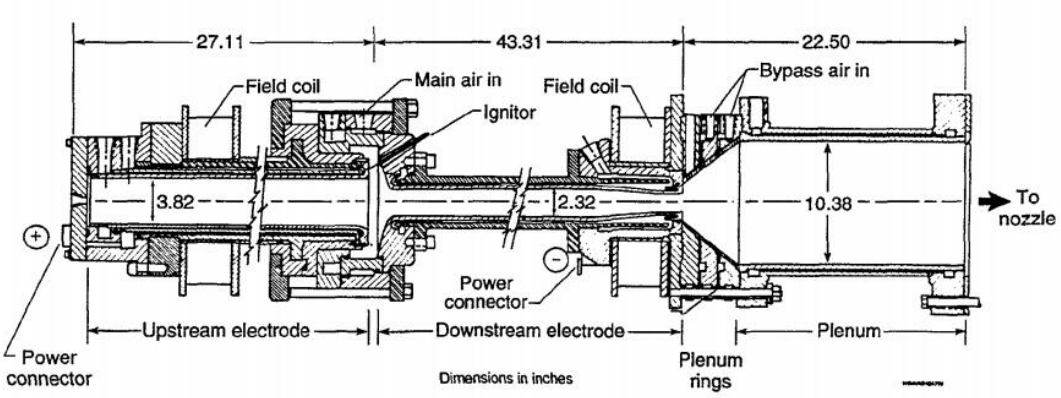

Fig. 2.14 Representation of the AHSTF. Image from [48].

The tests were performed in the Arc-Heated Scramjet Test Facility (AHSTF), part of the NASA Langley Scramjet Test Complex, partially represented in Figure 2.14. This wind tunnel adopts a voltaic arc between two electrodes to provide heat to the air stream. Later, the heated stream is mixed with colder by-pass air in the plenum chamber, getting the desired stagnation properties (h^o and p^o). Through the expansion of the high enthalpy flow in a purposely designed nozzle, supersonic flow with a satisfactory static temperature and pressure can be obtained. The facility can reproduce flow properties analogous to the one resulting from the aerothermodynamic processing of ram air through the inlet, but only in the one-dimensional sense. Other features such as distortion and disturbances from the inlet, accurate boundary layer thickness, surface temperature distribution, and air composition cannot be meticulously mimicked. More information about the flight envelope and test capabilities of this facility can be found in references [46] and [48].

A full-scale, direct connection rig had been built, identified with the acronym HIFiRE Direct Connect Rig (HDCR). This model replicates the isolator, cavity and combustor regions, highlighted in Figure 2.13. For exploratory purposes, additional

injection sites were introduced and tested in the model, for a total of five sites: two upstream, two downstream, and one in the cavity region. However, most of the experimental data had been obtained for the most promising configuration, using P1 and S1, reported in Figure 2.12. The flush-wall injectors, in the so-called 4×4-C configuration, had been made working under chocked condition, with an as even as possible fuel splitting between injectors of the same district. The flight vehicle had been designed to use a gaseous mixture of light hydrocarbons, the product of the endothermic cracking of the liquid JP7 fuel used to cool down critical components of the flight vehicle. After the work of Pellett et al. [49], a mixture of:

$$\chi(\mathbf{C_2H_4}) = \mathbf{0.64} \quad \text{and} \quad \chi(\mathbf{CH_4}) = \mathbf{0.36}$$

emerged as a good candidate for the ground tests, since it showed similar characteristics to the endothermically cracked JP7 in terms of time of ignition delay, kinetics (S_u) and flame holding.

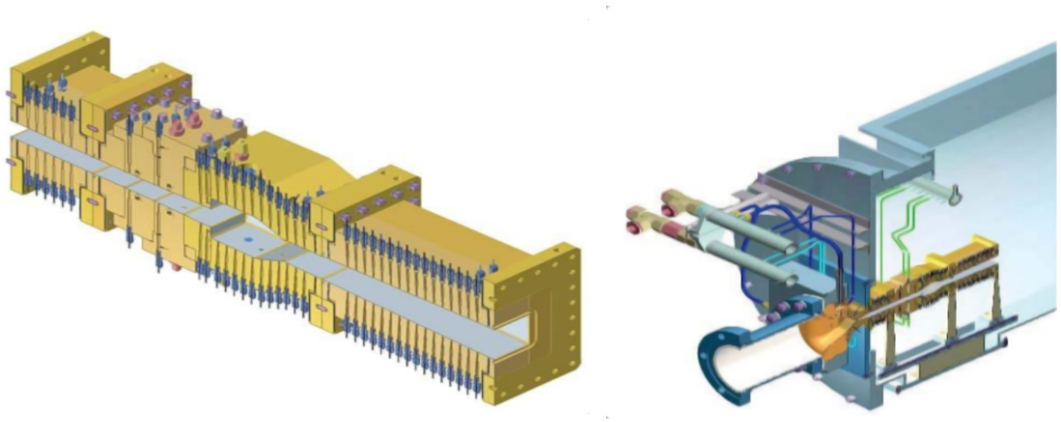

Fig. 2.15 Cutaway representation of the HDCR, and the rig as installed in the AHSTF. Notice the fuel injection sites and the instrumentation's general layout (pressure taps in blue). The image is given by [46].

From the instrumentation standpoint, a set of pressure taps, thermocouples, and heat flux gauges had been used to achieve pressure distribution and local values of temperature and heat flux. In particular, pressure ports had been mainly distributed in the streamwise direction along the centerplane, on both the cowl and body sides. Notably interesting districts, such as the isolator inlet, the P1 injection zone, and the combustor outlet have been instrumented with an array of four pressure taps in the

spanwise direction. More comprehensive information about the instrumentation and the acquisition system can be found in reference [46], as well as a detailed layout of the sensors.

Emulating the dual-to-scram mode transition due to the acceleration of the vehicle was beyond the limits of the AHSTF, which could only provide a constant Mach number due to the fixed geometrical expansion ratio of the nozzle. To widen the analysis, two different nozzles were built and tested to separately capture the two different operational modes along the mission profile. First, Hass, Cabell, and Storch [46] focused on a parametric study varying fuel distribution and evaluating its effects on operability (i.e. avoiding the presence of shocks too upstream in the isolator, to keep a safety margin from inlet unstart events). After phase one Storch, Bynum et al. selected four interesting cases which are analyzed in more detail in [1]; see Table 2.1.

Table 2.1 Cases reported by [1].

Run #; time slice	M_∞	M_i	T^o [K]	p^o [MPa]	ϕ_{tot} [-]	ϕ_{P1} [-]	ϕ_{S1} [-]
123.1; 7.5 s	5.84	2.51	1550	1.482	0.65	0.15	0.50
125.1; 12.0 s	6.5	2.51	1848	1.496	1.00	0.40	0.60
135.6; 19.0 s	7.5	3.46	2387	4.371	1.00	0.30	0.70
136.3; 18.0 s	8.0	3.46	2569	4.275	1.00	0.40	0.60

The present work focuses on the modeling and analysis of two of the cases listed in Table 2.1, namely **125.1** and **136.3**. These two cases are particularly interesting: in the experiments, the dual-mode and the scramjet mode were observed respectively in the former and the latter, using the same fuel distribution scheme. The results will be presented and discussed later, contextually to the analysis of the results of the simulations.

Chapter 3

Numerical Simulations

In Chapter 2, all the necessary background information has been reviewed. Now, some practical aspects regarding the numerical simulations, e.g. the meshing technique, the boundary conditions, and the general methodology will be discussed.

3.1 Hexahedral Mesh

For both cases, the computational grid has been obtained using the OpenFOAM native meshing utility `blockMesh`. When the geometry of interest is particularly simple, it can be decomposed into a set of three-dimensional hexahedra, each defined by eight vertices and by the edges connecting them, which are then "split" in a structured grid using a user-defined number of discretization intervals. The mesher also allows for more advanced manipulations, for instance, curvilinear edges, degenerate hexahedra, and grading functions. The result of the meshing procedure is represented in Figure 3.1. From the figure, it can be seen that the computational domain includes one-quarter of the HDCR in the streamwise direction (thus exploiting symmetry in the spanwise direction), and does not exploit symmetry in the transversal one. In other words, the fields are not assumed to be symmetric about the $x-y$ plane.

The grid could be in principle treated as a structured one and does not suffer from continuity issues at the interfaces between the fifty-one blocks building the geometry. It shows good overall global quality parameters, e.g. low average non-orthogonality, skewness, and aspect ratio. This allowed a rather satisfactory numerical stability of the simulations. Coordinates of curved edges - which are necessary to represent

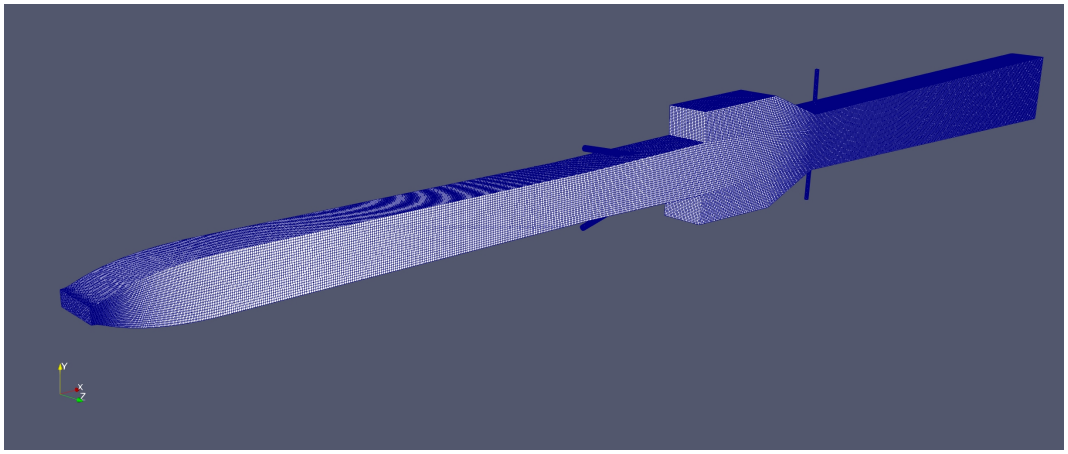

Fig. 3.1 Overall view of the mesh built by the author in `blockMesh`, in its base version. A reconstructed nozzle and O-grid meshed injectors were also included. A single "unit" of the geometry, which constitutes the domain of interest of this study, is composed by fifty-one blocks.

the pipes' O-grid mesh and the nozzle - are generated using MATLAB® scripting. Figure 3.2 shows a detail of the P1 injector mesh, with the cavity region visible in the background.

As visible in figure 3.2, the injection districts are where the mesh quality is lower. Non-orthogonality and skewness are way more pronounced here than in the rest of the domain: this is the reason why the non-orthogonal correction for surface normal gradients (see Section 2.2.4) has been turned on. In addition to that, meshing the injectors' core required a smaller volume characteristic dimension than the rest of the mesh, and this fact widened the gap between the average and maximum local Courant numbers (with the latter limited by the CFL condition). However, parametrizing the grid generation in those areas of interest (e.g. aspect ratio and length of the enveloping rectangular area visible in Figure 3.2), the mesh anisotropy was kept at a low level and this matter didn't represent an obstacle during the runs.

Three different mesh resolution levels were tested, defined by the resolution parameter N:

$$\mathrm{N} = \frac{L_{y,2}}{\Delta}$$

where $L_{y,2}$ is the transversal dimension at the isolator entrance, $L_{y,2} = 1\,\text{inch}$, and Δ is the characteristic mesh size in the y direction. Additionally, a locally refined grid (in the primary injection area) has been included in the study; a detail of it is reported in Figure 3.3.

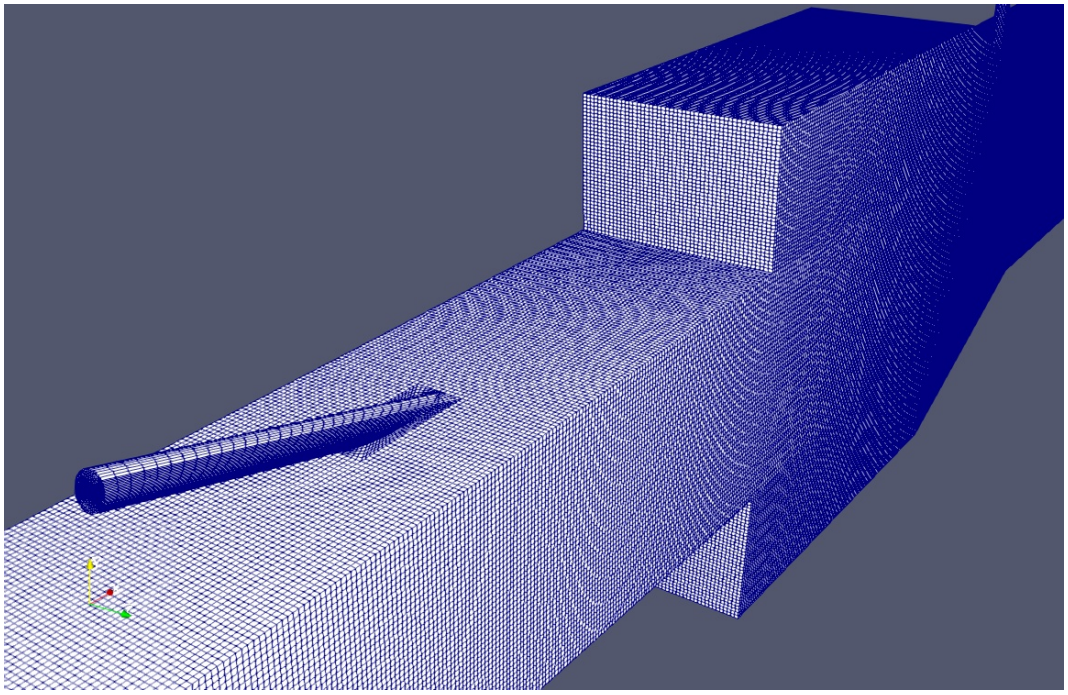

Fig. 3.2 Detail of the mesh in the P1 and cavity region. The base version of the mesh - defined by the parameter N=48, is shown.

Table 3.1 Grid resolution levels. Four different resolution levels were adopted, during the initialization process, as explained in Section 3.4.

	coarse mesh	**base** mesh	**P1-refined** mesh	**refined** mesh
N	24	48	-	64
Δ[mm]	1.06	0.53	-	0.40
# of cells [mln]	≈ 0.8	≈ 7	≈ 10.5	≈ 16

Once N is chosen, the determination of the mesh characteristic length in the isolator region is straightforward, and it is reported in Table 3.1. Notice that due to the peculiar topology of the region and the requirement of matching nodes at the block interfaces, the Δ in the isolator region spontaneously defines the low-end in terms of spatial resolution. Coarser grids were used to rapidly get rid of large-scale, slow-evolving transients, and computationally demanding jobs on finer grids were run using initial conditions from coarser grids.

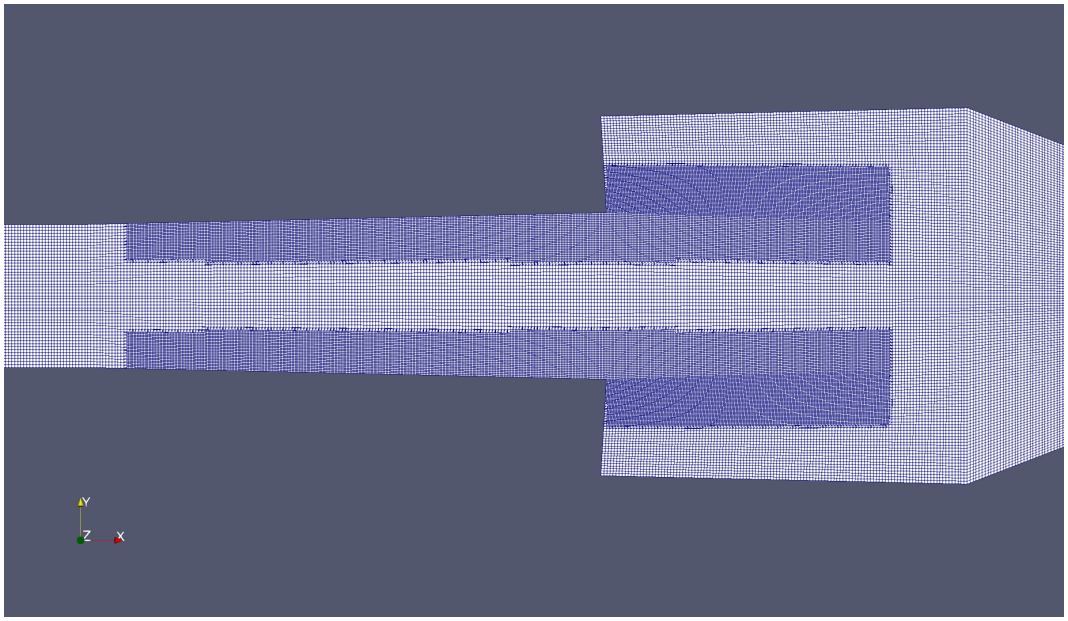

Fig. 3.3 Detail of the locally refined mesh in the P1 and cavity region. The background is characterized by the base value N=48.

3.2 Estimate of Nozzles Geometry

During the simulations' setup phase, the question about how to deal with the inflow boundary conditions emerged, as it will later be explained in Section 3.3. A survey of the literature emphasized how among previous CFD studies of the HIFiRE 2 and the HDCR, this topic has been treated with several different approaches. In the LES framework, Bermejo-Moreno et al in [50] considered a nominal boundary layer thickness of approximately 1 mm, synthetically generated via digital filtering technique and superimposed at the isolator entrance; a similar approach was followed by Lacaze, Vane and Oefelein in their 2016 paper [44]. Saghafian et al. in [21] again followed a similar strategy, using rescaled profiles from DNS data and digital filtering, and included a reduced portion of the isolator in their finest grid. Other authors, like Yentsch and Gaitonde in [51], included the wind tunnel nozzle in their exploratory simulations, which on the other hand relied on RANS turbulence modeling.

In the present work, the wind tunnel nozzle geometry was mimicked starting from the isolator entrance Mach number reported in Table 2.1. The author relied on the Supersonic Nozzle Design Tool [52], written by Cory Dodson using MATLAB®

coding; the script employs the inviscid, two-dimensional method of characteristic lines as presented by Anderson in [6], and produces as an output the diverging section of a nozzle satisfying the input design parameters, i.e. the exit section Mach number and the ratio of the specific heats of the fluid. The following algorithmic procedure was followed:

1. From the stagnation temperature of Table 2.1, the throat and isolator entrance static temperatures are calculated accounting for the variation of specific heats ratio with temperature [53];
2. An average value for the ratio of specific heats $\overline{\gamma} = 0.5(\gamma^* + \gamma_2)$ is obtained using known information after step 1.;
3. The Supersonic Nozzle Design Tool is used to get the first iteration of the geometry;
4. Two-dimensional finite volume RANS simulations are used to evaluate the effect of viscosity, namely the reduction of the effective exit area caused by the boundary layer displacement thickness and the consequent reduction in M_2;
5. A corrective factor, simply defined as the ratio between the design M_2 and the one obtained after the RANS simulation (> 1), is applied to the input Mach number of the Supersonic Design Tool;
6. A new iteration of the geometry is obtained, and steps 4. to 6. are repeated until a "satisfactory" geometry is obtained.

Due to the many approximations, the relative tolerance after which the procedure's output was considered "satisfactory" was kept quite loose, and the method didn't require more than two or three loops. The nozzle obtained for the 125.1 case is reported in Figure 3.4 as an example.

3.3 Boundary Conditions

The data reported in Table 2.1 were used as a starting point in the determination of the boundary conditions. Due to the gargantuan physical complexity of scramjet

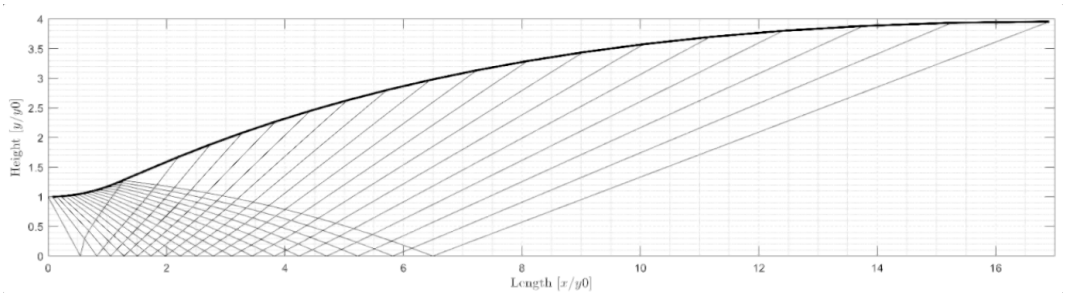

Fig. 3.4 Output of the method of characteristic lines implemented in [52] and used in the algorithmic procedure presented in the chapter. As reported by the author of the code, the script has trouble dealing with a high number of characteristic lines for greater Mach numbers. This factor limited the resolution of the polyline in the downstream region of the nozzle, especially in the 136.3 case.

engine experiments, it is often difficult to keep them under controlled and prescribed conditions. The inherently high enthalpy of the flow, heat transfer, real gas effects (e.g. air contamination with high-temperature species like nitric oxide), and structural and operational limits of the instruments are among the limiting factors for this extreme kind of wind tunnel tests, as reported in [5]. For the reasons listed above, scramjet engine tests are often characterized by remarkable uncertainty. Although much progress has been made in the last decade, building a "quiet" hypersonic test facility is still among the research objectives of many governmental institutions, who see it as a valuable strategic asset.

In this study, the first practical difficulty emerged while looking for inflow values of p, T, and U. Storch, Bynum, et al. in [1] reported experimental pressure distribution for all the cases reported in Table 2.1; however, no value for the inlet mass flow rate was reported in the dataset. On the other hand, Bermejo-Moreno et al. report values of mass flow for both the dual-mode and scramjet cases, labeling them as ground test data.

$$\dot{m} = \frac{p^o A_2}{\sqrt{RT^o}} f(\gamma_2, M_2) \tag{3.1}$$

For comparison, the theoretical mass flow rate was computed with quantities reported by [1] for each case using stagnation properties and the geometrical features of the HDCR into equation 3.1, where subscript "2" denotes the isolator entrance. This highlighted a discrepancy of $\approx$ **10**% for the **125.1** case, a figure that was observed to be even higher ($\approx$ **25**%) in the **136.3** case, with the values reported by [50] always

being lower than the theoretical prediction. Among the possible causes of this mismatch, there are:

- Total pressure losses due to the non-isentropic evolution of the airflow through the converging-diverging nozzle. The plenum chamber has a circular cross-section, which is driven into a rectangular throat section of aspect ratio AR=4; dissipative phenomena such as boundary layer, secondary flow features, and shockwaves could justify the estimated pneumatic efficiency of about 0.9 and 0.8 for the $M_2 = 2.51$ and $M_2 = 3.46$ cases respectively;
- Uncertainty about the reference value of p^o and the actual one;
- Uncertainty about run-to-run and during-run p^o variations - see [46];
- Uncertainty about the geometry of the AHSTF nozzle throat section, which is reported to have experienced sever thermal distress during the experiments - see [1];

The experimental data reported in the references are characterized by the equivalence ratios ϕ_{tot}, ϕ_{P1} and ϕ_{S1} as test parameters. For the sake of the maximum control over known experimental parameters, the boundary conditions for U were given in terms of mass flow rate, with the values provided by [50]. Using the assumption of adiabatic, non-isentropic flow (i.e. conservation of stagnation enthalpy), the inflow boundary conditions for temperature were specified in terms of plenum total temperature; on the other hand, the throat pressure values were chosen so that the physical constraint $M \approx 1$ in the nozzle throat was satisfied.

Concerning the fuel injectors, little or no information is given in the experimental reports. It is known from Hass, Cabell et al. [46, p. 10] that the fuel injectors were designed to operate in chocked conditions. Unfortunately, the flight vehicle's air intake required a modification after the HDCR's manufacturing phase; this led to the unchoked operation of the primary injectors under the design air mass flow, equivalence ratio, and fuel splitting. To keep and even fuel distribution, choking orifices were introduced upstream in the fueling system. In the context of this work, the stoichiometric air-to-fuel ratio was obtained after considering the following

balanced combustion reaction:

$$(0.36\mathrm{CH4} + 0.64\mathrm{C2H4}) + 2.64(\mathrm{O2} + 3.76\mathrm{N2}) \rightarrow 1.64\mathrm{CO2} + 2\mathrm{H2O} + 9.9264\mathrm{N2} \tag{3.2}$$

which after some manipulation gives:

$$\alpha_{st} = 15.31\,\mathrm{kgs}^{-1}/\mathrm{kgs}^{-1}$$

At this point, the values of $\dot{m}_{P1}$ and $\dot{m}_{S1}$ depend on $\dot{m}_{air}$ - which is given as a boundary condition - and on the experimental parameters ϕ_{P1} and ϕ_{S1}. Assuming fuel injection at 300 K and critical ($M = 1$) conditions, the boundary values for the fuel temperature were assigned constraining total temperature at the injector pipe inlet, and relaxing pressure with a zero gradient boundary condition. This allowed the fuel stream to adapt spontaneously to the subsonic near-wall environment, satisfying fairly well all the experimental constraints.

An arbitrary low value was given for the turbulent kinetic energy k, while homogeneous von Neumann boundary conditions were provided for both eddy diffusivities ν_t and α_t. A summary of the inflow properties is given in Table 3.2.

Table 3.2 Inflow boundary conditions. The experimental traits of the sonic throat (for the wind tunnel nozzle, as estimated - see Section 3.2) and chocked injectors with $T_{inj} \approx 300\,\mathrm{K}$, as well the global equivalence ratio and fuel splitting, were consistently satisfied. Fixed values for species mass fractions were assigned according to the balanced chemical reaction reported in 3.2.

Field		type	value; 125.1		value; 136.3	
Nozzle Throat Section						
p	[Pa]	fixedValue	0.956×10^6		2.33×10^6	
T	[K]	totalTemperature	T0 1848	gamma 1.308	T0 2569	gamma 1.299
U	[kg/s]	flowRateInletVelocity	0.284		0.228	
PI Injectors						
p	[Pa]	zeroGradient	-		-	
T	[K]	totalTemperature	T0 350	gamma 1.26	T0 350	gamma 1.26
U	[kg/s]	flowRateInletVelocity	0.00371		0.00298	
SI Injectors						
p	[Pa]	zeroGradient	-		-	
T	[K]	totalTemperature	T0 350	gamma 1.26	T0 350	gamma 1.26
U	[kg/s]	flowRateInletVelocity	0.00556		0.00447	
All Inlets						
k	[m^2/s^2]	fixedValue	1×10^{-8}		1.25×10^{-8}	
ν_t	[m^2/s]	zeroGradient	-		-	
α_t	[kg/m/s]	zeroGradient	-		-	

The solid walls, sidewalls, and outlet were treated as in Table 3.3. No-slip conditions for velocity and `zeroGradient` for non-turbulent scalar fields were employed, while k, ν_t and α_t were treated using wall functions. The two sidewalls were assigned a double `simmetryPlane` boundary condition; this, *de facto*, is equivalent to neglecting the boundary effects caused by solid sidewalls, e.g. the presence of

a boundary layer. The outlet has been investigated using both `zeroGradient` and `waveTransmissive` boundaries during the study, showing little or no sensitivity.

Table 3.3 Solid walls, outlet, and sidewalls boundary conditions. A no-slip condition was applied to the solid walls - i.e. the cowl and body sides, the nozzle contour, and the walls of the circular pipes - which were considered **adiabatic**. Turbulent quantities were treated using wall functions, keeping the default coefficients. In the outflow section, homogeneous von Neumann boundary conditions have been selected. The effect of `waveTransissive` outlet for pressure was tested with $l_\infty = 0.711\,\text{m}$, $p_\infty = 57\,\text{kPa}$, $\gamma = 1.35$, without bringing dramatic changes in the solution. On both sides, the sidewalls were considered symmetry planes.

Field		`type`	`value`; 125.1	`value`; 136.3
Solid Walls				
p	[Pa]			
T	[K]	`zeroGradient`	-	-
Y_k	[-]			
U	[m/s]	`fixedValue`	**0**	**0**
k	[m^2/s^2]	`kqRWallFunction`		
ν_t	[m^2/s]	`nutkWallFunction`	-	-
α_t	[kg/m/s]	`alphatWallFunction`[1]		
Outlet				
Generic		`zeroGradient`	-	-
p	[Pa]	`zeroGradient`	-	-
		`waveTransmissive`	see caption	
Sidewalls				
Generic		`symmetryPlane`	-	-

[1] OpenFOAM uses an unconventional definition of α_t, defining it as the product of the diffusivity coefficient and density (as can be deduced from the measurement unit). This requires boundary condition for α_t to be part of the specific class of wall functions for compressible flows.

3.4 Initial Conditions and Methodology

It is well known that the mathematical problem of solving a system of hyperbolic PDEs - e.g. the turbulent, reacting Navier-Stokes equations in their LES formulation - can't be solved without a set of initial conditions, from which the system's evolving state is determined making the solution *march in time*.

As it was discussed in Section 2.2.7, the solver used in this study implemented explicit time integration, which requires the CFL stability condition to be satisfied. Recalling the definition of the Courant number given in equation 2.43 and analyzing the terms involved, it is clear where the challenge of high-speed, high-enthalpy flows is: relatively high local propagation speeds and grid resolution requirements - necessary to capture shocks and large gradients - could severely limit the rate at which the solution advances in time. For instance, in both the cases presented, the timestep was limited at $\Delta t \approx 3 \times 10^{-8}$ s using a Co_{max} limitation $Co_{max} = 0.8$.

Given the intrinsic time-dependent nature of LES, the severe limitations on the timestep, and the computational cost of the setup, there is no doubt that an *initialization strategy*, rather than simple initial conditions, should be followed. The underlying idea is to make the *physical transient* extinguish with the lowest computation effort possible, choosing initial conditions fairly close to the expected statistically stationary state of the system. For the sake of this, initialization with coarser grids and cheaper models (e.g. unreacting RANS) is necessary before switching to more and more computationally expansive - and physically complex - models.

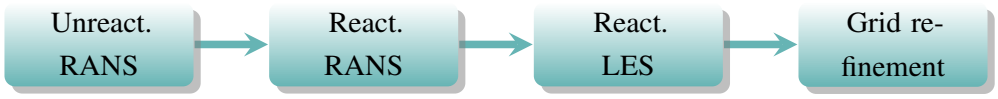

The procedure followed involved four main steps. First, the thermophysical fields of the three-dimensional domain were settled using the unsteady RANS equations closed with the Menter's $k-\omega$ SST turbulence model and chemical species as passive scalars. Once the flowfield was established, the combustion properties of the system were activated, and all the fields went through a new transient again. Once even this second transient reached a "steady" behavior, the computed solution was used as the initial condition for the most expansive model, reacting LES. However, it is well known that RANS and LES have different requirements in terms of grid

resolution: later in the process, the solution from the coarse mesh was mapped on the base, P1-refined, and refined mesh. It is important to emphasize that, in this particular case, the range of mesh resolutions adopted is not sufficient to consider the successive refinements as a grid-independence study, but rather part of the initialization procedure. Results from the initializing, "simplified" simulations are omitted for brevity.

3.5 Numerical Schemes

The numerical schemes employed in the present work have already been discussed in Section 2.2. However, Listing 3.1 reports an overview of the input file.

```
fluxScheme      Kurganov;

ddtSchemes
{
    default         Euler;
}

gradSchemes
{
    default         Gauss linear;
}

divSchemes
{
    default         none;
    div(tauMC)      Gauss linear;

    div(phi,k)            Gauss limitedLinear 0.25;
    div(phi,Yi_h)         Gauss limitedLinear 0.25;
    div(((rho*nuEff)*dev2(T(grad(U))))) Gauss linear;
}

laplacianSchemes
{
    default         Gauss linear corrected;
}

interpolationSchemes
{
    default          linear;
    reconstruct(rho)    vanLeer;
    reconstruct(U)   vanLeerV;
    reconstruct(T)   vanLeer;
    reconstruct(k)   vanLeer;
}

snGradSchemes
{
    default         corrected;
}
```

Listing 3.1 Numerical schemes

Chapter 4

Discussion of the Results

The following section will be dedicated to the discussion of the results emerging from the modeling effort. Time-averaged pressure distributions and instantaneous snapshots will be presented, highlighting differences and analogies with the experimental results and with akin models.

In the preceding chapters, the modeling framework has been extensively described. The following results are the output of *wall-modeled LES*, closed with the set of constitutive equations reported in Section 2.1.2. More precisely, the *dynamic one-equation eddy viscosity model* was used, while the thermophysical properties of the mixture were provided in the JANAF format. Finite-rate modified *Arrhenius chemistry* was used, and turbulence-chemistry interaction was modeled with *PaSR* and *laminar combustion models*; results will be reported only for the latter. The *Z66 reaction mechanism* by Zettervall, Fureby, and Nilsson [41] was selected. The work was performed using the open-source CFD toolbox OpenFOAM, employing a monotonicity-preserving flux reconstruction scheme based on central differencing and flux limiters. The modeling philosophy is tested and validated; it had been successfully applied by Fureby et al. on the Waidmann [54], Micka & Driscoll [55] and HyShot II [56] combustors. In addition to that, the modeling framework has been recently validated against the experimental results of the LAPCAT II supersonic combustor [57], showing admirable prediction capabilities.

The HIFiRE 2, however, turned out to be extremely difficult to investigate without further tuning of the numerical setup. Insufficient burning, lower-than-nominal pressure levels, and delayed combustion manifested themselves in both the

dual-mode and pure scramjet cases. Interestingly, the same symptoms showed up in past studies by Bermejo-Moreno et al. [50], Saghafian et al. [21] and Lacaze et al. [44]. The rest of the chapter will be devoted to the discussion of the most relevant results.

4.1 Dual-mode Operation (case #125.1)

The reacting, LES simulation of the dual-mode operation began after the initialization procedure described in Section 3.4, using the inflow boundary conditions of Table 3.2. In the first stages, good agreement with the experimental results was found for the RANS simulation of the cold flow on the coarse (N=24) mesh, as shown in Figure 4.1 (circles and dashed line). The $k-\omega$ SST turbulence model managed to capture the pressure drop in the cavity; on the other hand, the simulation overpredicts the pressure drop around the expansion corner formed by the ramp and the combustor ($x \approx 0.4\,\mathrm{m}$). A recirculating region characterizes the flow in this area, followed by a second pressure peak ($x \approx 0.5\,\mathrm{m}$) caused by the reattachment of the shear layer. The pressure level is satisfactorily predicted, while the peak appears in a slightly more downstream position. Pressure then decreases with a trend similar to the experimental one.

The solid line in Figure 4.1 represents the final result of interest, i.e. the pressure distribution for the reacting LES case. The model is not capable of reproducing the pressure distribution observed in the experiments. Exothermicity is delayed downstream of the secondary injection zone, while pressure and heat release in the cavity region are way lower than in the AHSTF measurements. This last fact leads to an insufficient back-pressure in the isolator and, as a consequence, to the absence of any pre-injection shock train (one of the characteristic flow features of the dual-mode operation).

It is interesting to point out that similar behavior has been previously experienced in two previous studies: [50] and [21]. In both these two examples, the authors used a flamelet/progress variable approach; a good agreement was obtained in both cases after introducing a correction to the model. In the former case, Bermejo-Moreno limited the flamelet library only to its fully-reacted portion ($\widetilde{C} = 1$), which is equivalent to assuming infinitely fast chemistry. Saghafian introduced a compressibility correction whose details can be found in a previous article from the same author

et al. [58]. In the present work, combustion enhancement was sought by selecting the *laminar* combustion model. This is equivalent to considering a limit case of the PaSR in which the reacting volume fraction $\kappa \approx \tau_c/(\tau^* + \tau_c) = 1$ everywhere in the domain. In other words, the mixing timescale in each finite volume is considered negligible compared to the chemical timescale, and the unresolved reacting fine structures behave like well-stirred reactors. This countermeasure, however, did not produce the desired effects.

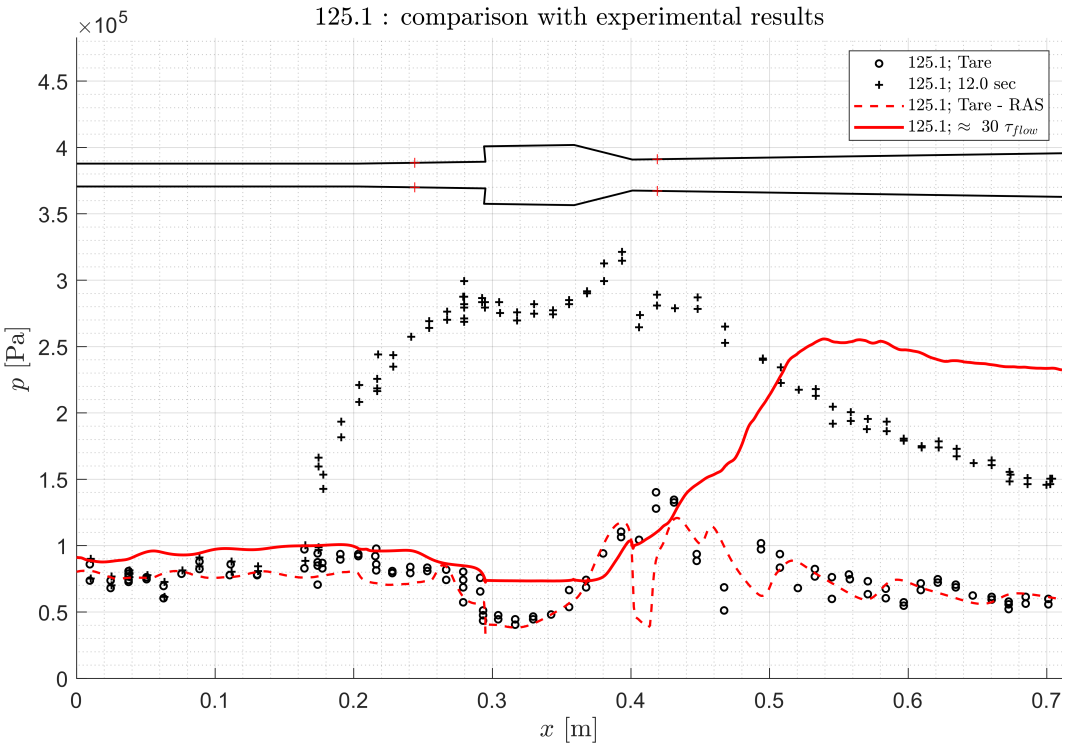

Fig. 4.1 Time-averaged pressure distribution at the centerline between two injectors, after approximately thirty flow-through characteristic times. Experimental results are indicated with black symbols; circles and plus signs represent tare (unreactive) and combusting conditions, respectively. The dashed line represents the RAS simulation of the cold flow on the coarse N=24 mesh (intermediate step in the initialization procedure), while the solid red line represents the final output of the simulation. Pressure is overestimated in the isolator region, and the pre-injection pressure rise is not captured. Pressure and exothermicity in the cavity region are strongly underestimated, and combustion appears to be "delayed" downstream in the combustor region. The geometry and the position of the injection sites are reported for reference.

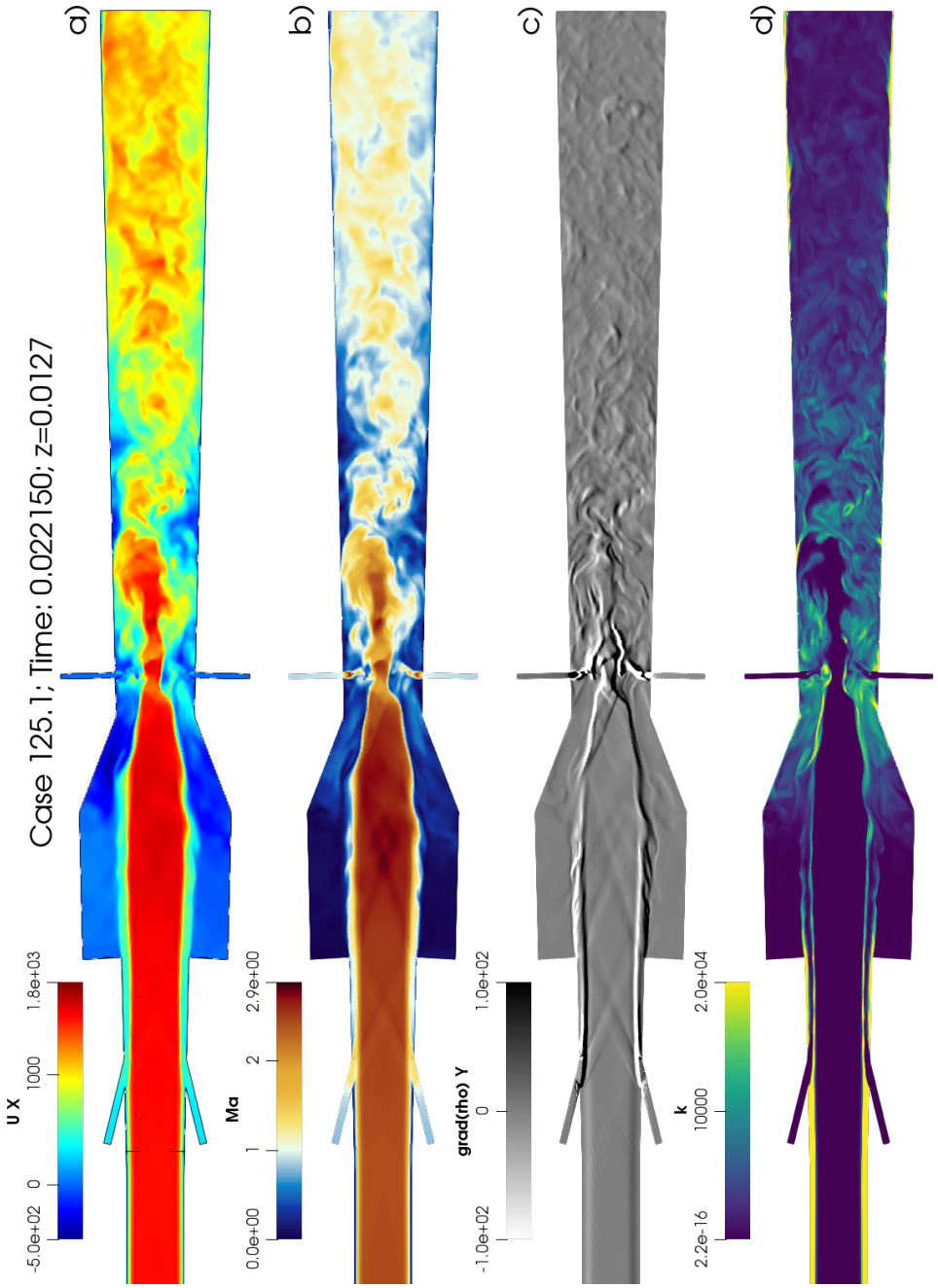

Fig. 4.2 Instantaneous **a)** filtered axial velocity (m/s); **b)** Mach number; **c)** vertical component of the density gradient $(\nabla\rho)_y$; **d)** turbulent kinetic energy k. Final instant of the 125.1 case, $z = 0.0127$ m, N=48 with cavity refinement.

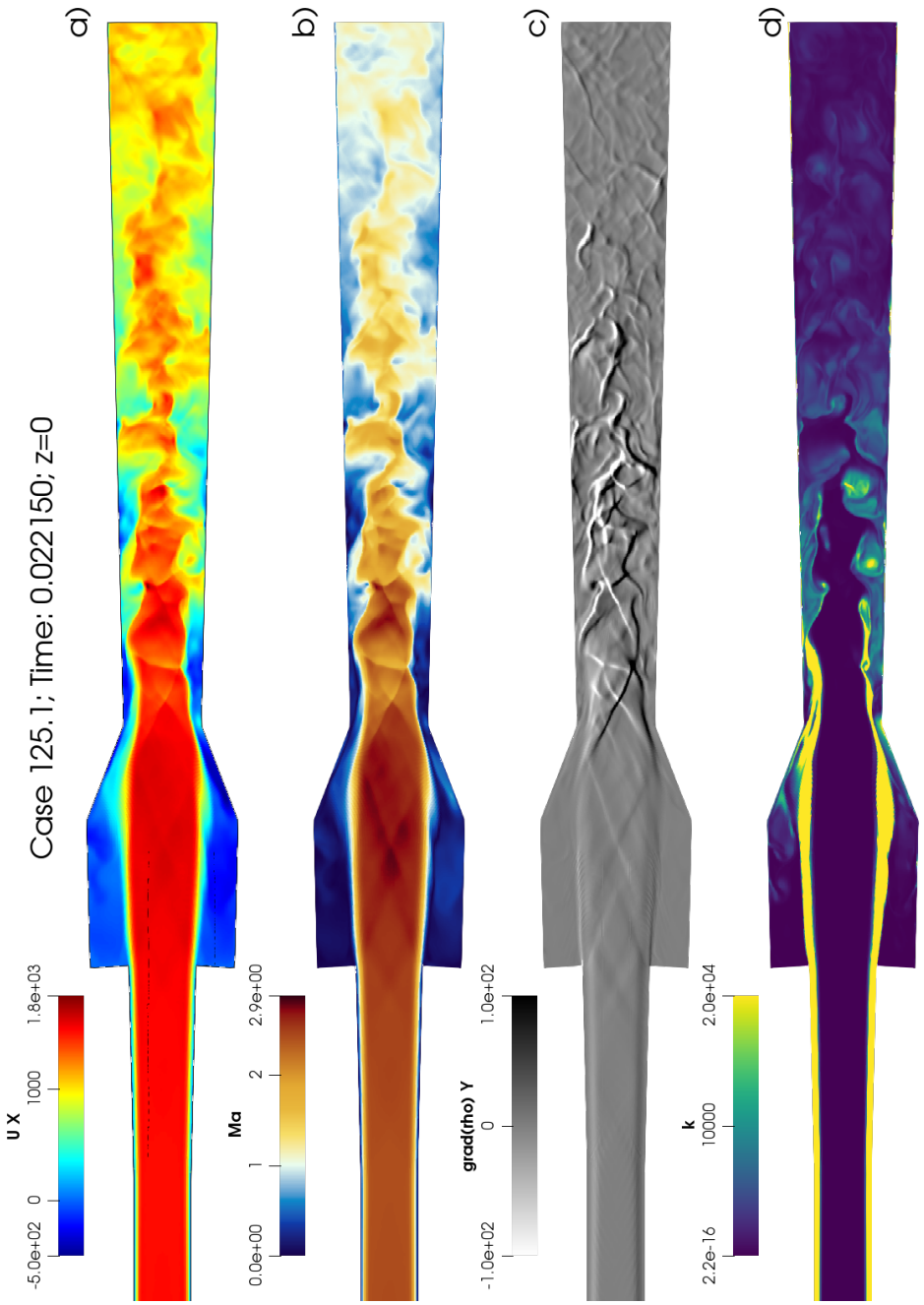

Fig. 4.3 Instantaneous **a)** filtered axial velocity (m/s); **b)** Mach number; **c)** vertical component of the density gradient $(\nabla\rho)_y$; **d)** turbulent kinetic energy k. Final instant of the 125.1 case, $z = 0$ m, N=48 with cavity refinement.

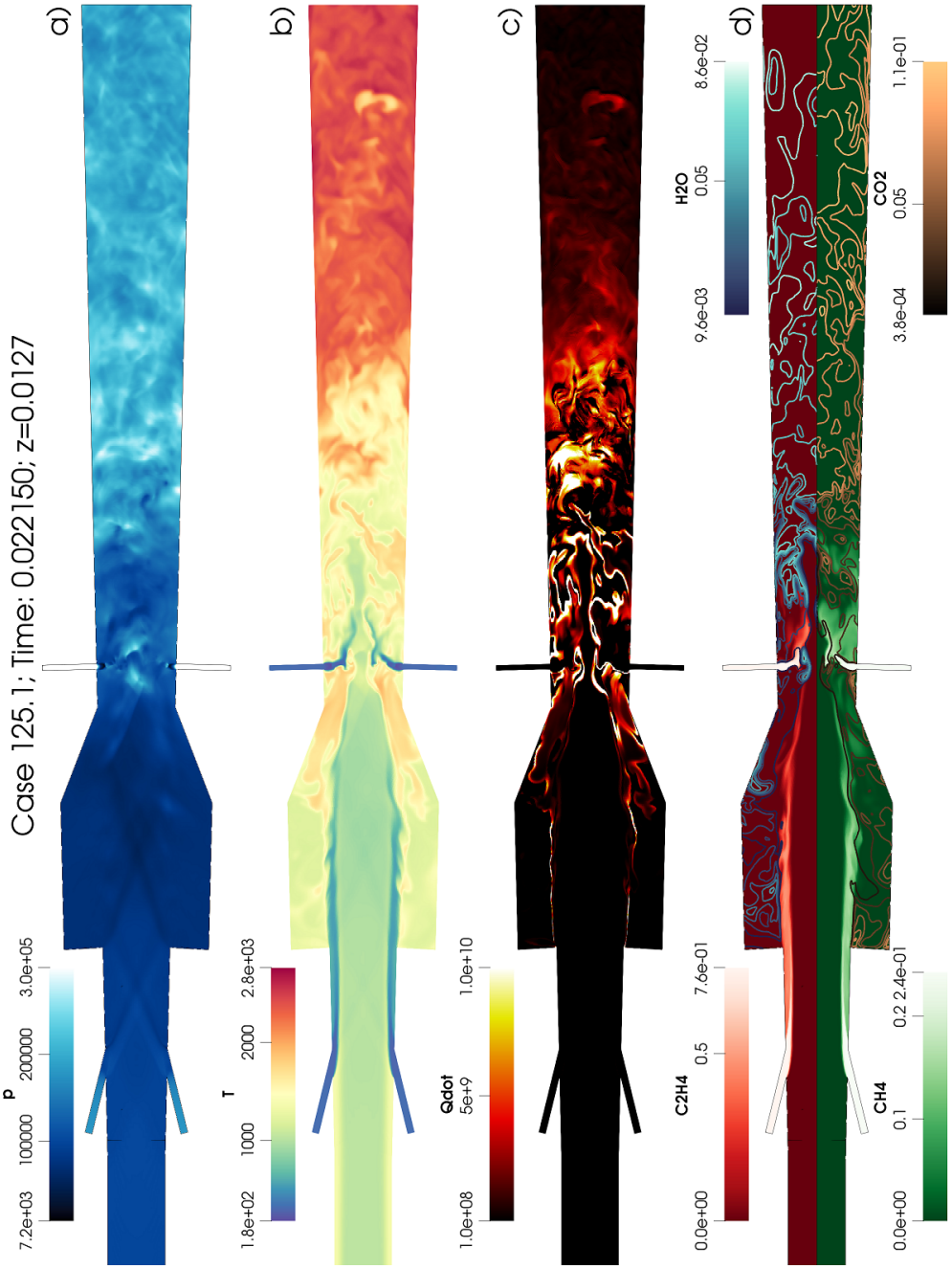

Fig. 4.4 Instantaneous **a)** pressure ([Pa]); **b)** temperature ([K]); **c)** heat release ([W/m^3]); **d)** fuels/products mass fractions ([−]). Final instant of the 125.1 case, $z = 0.0127$ m, N=48 with cavity refinement.

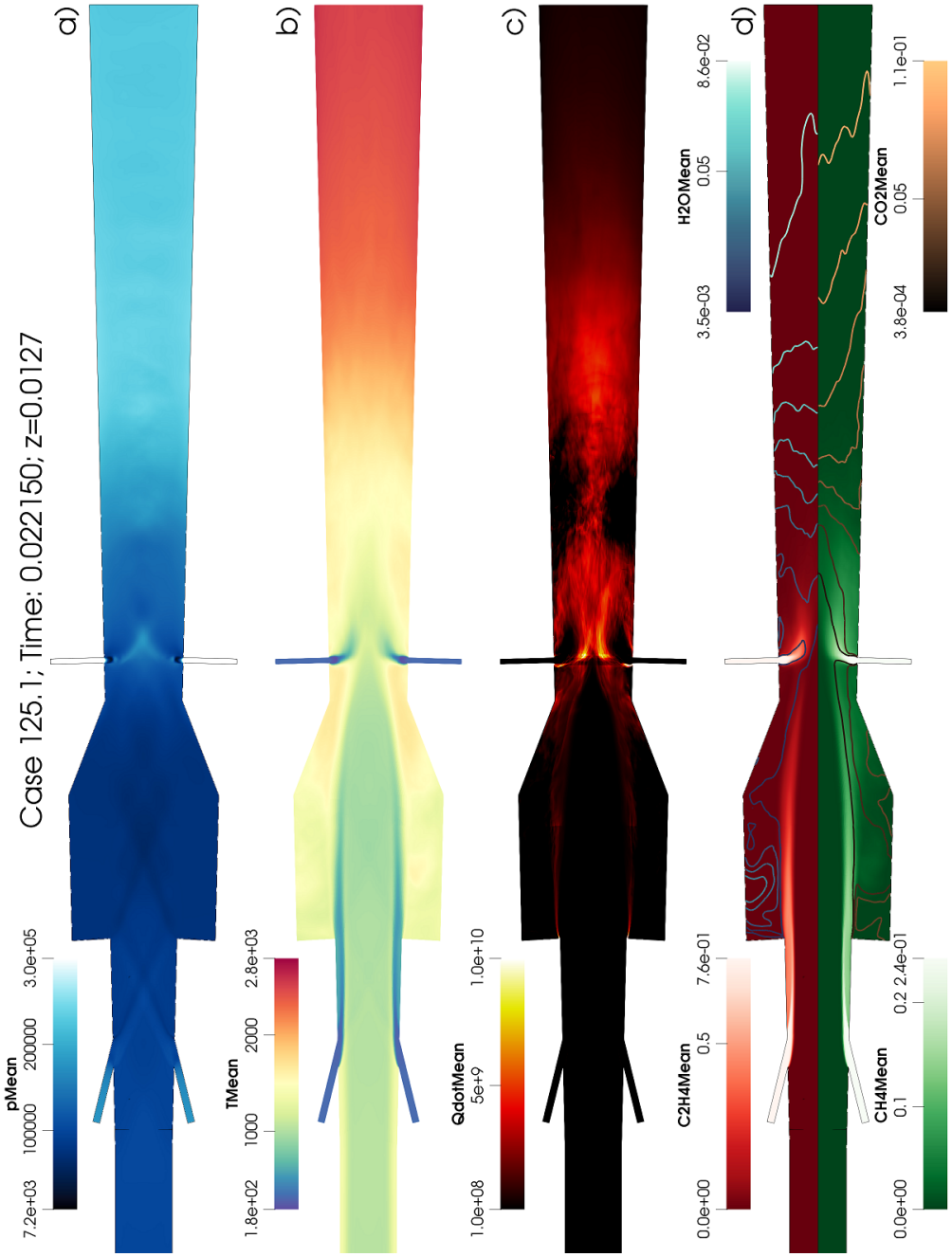

Fig. 4.5 Time-averaged **a)** pressure ([Pa]); **b)** temperature ([K]); **c)** heat release ([W/m^3]); **d)** fuels/products mass fractions ([−]). Final instant of the 125.1 case, $z = 0.0127$ m, N=48 with cavity refinement.

4.1.1 Instantaneous and Mean Flow Features

In this section, some of the most interesting flow features from the final instant of the 125.1 case will be explored: this is approximately thirty flow residence times after the start of the simulation. Despite the unsatisfactory agreement with the experimental results in terms of pressure distribution, the obtained data can be analyzed and commented, on to better understand the key fluid-dynamics phenomena involved.

From the "kinematic" point of view, the flow appears complex and inherently three-dimensional. Figure 4.2 and 4.3 compare the filtered axial velocity, Mach number, transverse component of the density gradient, and subgrid turbulent kinetic energy on the plane of the injectors and on the center plane, respectively. Notice that this plane is, in fact, the boundary of the computational domain treated with symmetric boundary conditions for every field; due to this approximation, the influence of solid sidewalls is neglected. The flow is turbulent, showing eddies of different sizes, especially in the combustor region. These coherent structures emerge from the interaction of the supersonic core flow with the ramp, the secondary injectors, and the cowl and body sides. The adverse pressure gradient in the ramp region, with the presence of discontinuities (see Figure 4.1 and 4.3 c), together with the blockage effect of fuel injection and exothermicity, cause instability of the boundary layer and localized areas of high turbulent kinetic energy production (figure 4.3 d). It can be observed that while the penetration of the secondary fuel flow noticeably spoils the core flow (Figure 4.2 a,b), the primary fuel flow alone - i.e. in the absence of adequate combustion and exothermicity in the cavity - is not capable of provoking a shock upstream the injection site: therefore, the presence of a pre-injection shock train (with increased temperature and pressure before fuel injection) and exothermicity in the cavity (with consequent pressure increase and backpressure) are supposed to be inherently coupled. In the simulation's scenario, the main mixing factor for the primary injector jets are weak horseshoe vortex pairings and the Kelvin-Helmholtz instability observed in both Figure 4.2 and 4.4 b,d.

Figure 4.4 and 4.5 report instantaneous and mean filtered p, T, $\dot{Q}$, fuels and products mass fractions in the plane of the injectors. As it can be directly observed, the recirculating flow in the cavity is hotter than the core flow. Thanks to the longer residence time of fluid particles entrailed in the cavity, reaction products - namely H2O and CO2 - populate the regions closer to the back-facing wall, as in figures 4.4 d, 4.5 d and 4.6 a. The shear layer instability mixes the hot, recirculating gas

with fuel from the primary injectors, stabilizing a thin reacting interface. However, despite this fact, the majority of the heat release is reported downstream of the secondary injector zone, i.e. in the combustor region. Here pressure, temperature, and reaction products mass fractions abruptly increase, bringing the flow close to a thermal chocking condition. From a different perspective, this is translated in the pressure distribution observed in Figure 4.1.

Figure 4.6 further investigates some properties of the combustion regime. Using Bilger's definition of the mixture fraction (equation 2.29) and the filtered species mass fractions, $\widetilde{Z}$ was calculated as a post process quantity. Panel **c)** of Figure 4.6 shows the instantaneous $\widetilde{Z}$ field in the upper half, with the solid black line representing the stoichiometric contour:

$$Z_{st} = \frac{Y_{O2}}{s + Y_{O2}} = \frac{0.22}{2.64 \mathscr{M}_{O2}/\mathscr{M}_{fu} + 0.22} = 0.0582$$

In the same figure, the progress variable $\widetilde{C}$, defined as $\widetilde{C} := \widetilde{Y}_{CO2} + \widetilde{Y}_{H2O} + \widetilde{Y}_{CO} + \widetilde{Y}_{OH}$, is shown. Figure 4.6 b reports the filtered scalar dissipation rate ($\propto \nu_t \left\| \boldsymbol{\nabla} \widetilde{Z} \right\|^2$) in logarithmic scale, obtained in the post-processing of the definition of equation 2.28 from de Bruyn Kops [20].

The presence of large scalar dissipation rate values in the cavity shear layer is related to the position of the stoichiometric contour: here, the mixing characteristic time is fast enough to guarantee that the reacting interface falls in the premixed regime, as shown in Figure 4.6 d. On the other hand, the dominant combustion regime in the combustor region is the non-premixed one. The Takeno Flame Index, G_{FO}, was used to differentiate between areas of premixed and non-premixed combustion. Its definition is:

$$G_{FO} = \frac{\boldsymbol{\nabla} \widetilde{Y}_{fu} \cdot \boldsymbol{\nabla} \widetilde{Y}_{O2}}{\left\| \boldsymbol{\nabla} \widetilde{Y}_{fu} \right\| \left\| \boldsymbol{\nabla} \widetilde{Y}_{O2} \right\|}$$

with the indexed heat release being defined as $\Upsilon = \left| \dot{Q} \right| G_{FO}$.

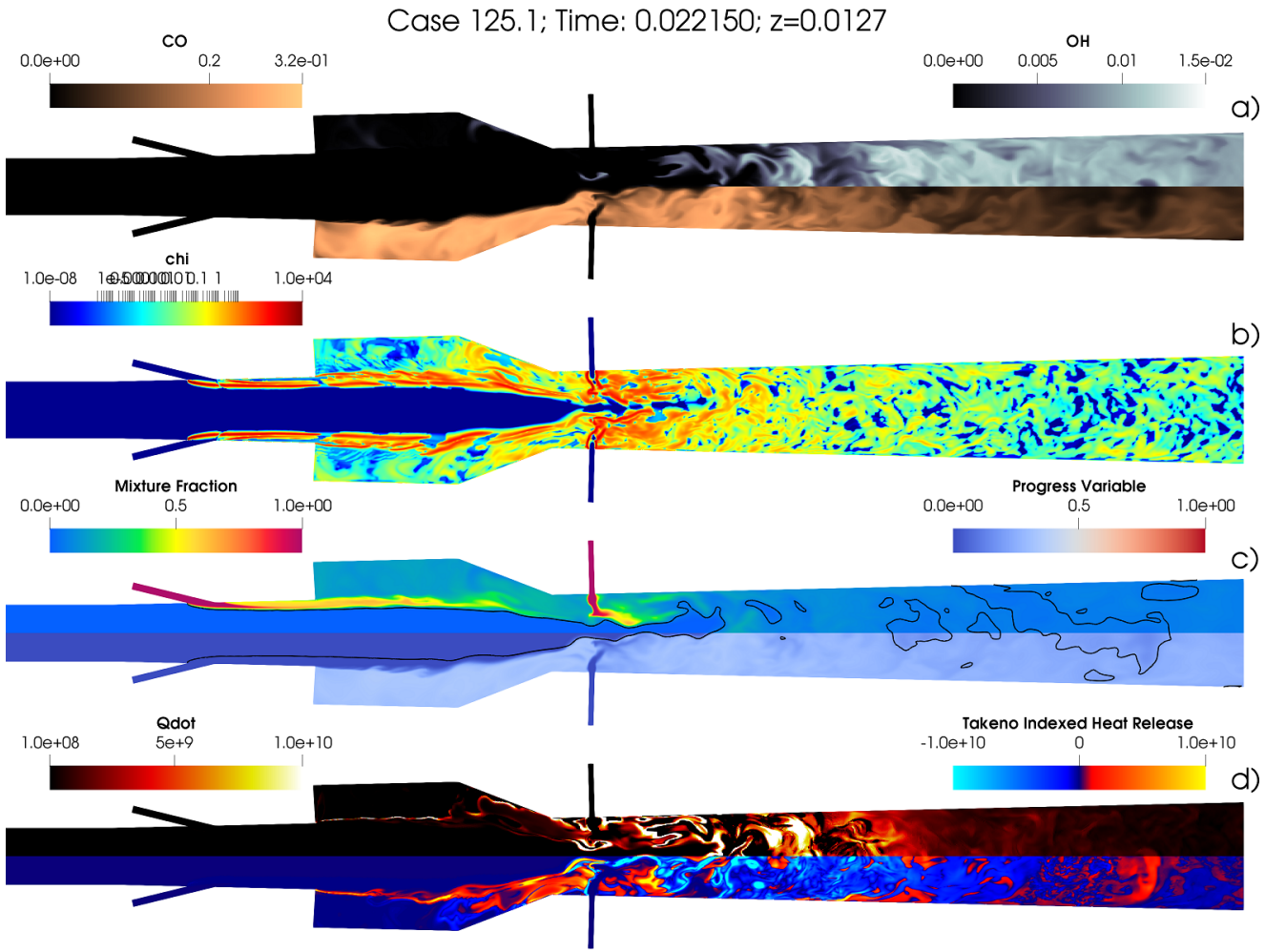

Fig. 4.6 **a)**: $\widetilde{Y}_{CO}$ and $\widetilde{Y}_{OH}$; **b)** scalar dissipation rate χ $[1/\mathrm{s}]$; **c)** mixture fraction $\widetilde{Z}$ and progress variable $\widetilde{C}$, $[-]$, with stoichiometric contour $Z_{st} = 0.0582$ **d)** comparison between $\dot{Q}$ and Takeno indexed heat release, $[\mathrm{W/m^3}]$. Final time-slice of the 125.1 case, $z = 0.0127\,\mathrm{m}$, N=48 with cavity refinement.

During the simulation, interesting unsteady phenomena have been observed. For instance, a low-frequency longitudinal mode emerged showing the following features. Areas of unburned fuel ignited near the combustor exit, creating spots of intense exothermicity and recirculation bubbles that "propagated" upstream, towards the cavity region. Here, these spots interacted with the secondary injectors, enhancing combustion in the immediate nearness of the jet. Enhanced combustion increased the backpressure experienced by the cavity flow and this consequently increased pressure in the cavity region. An adverse pressure gradient in the region between the primary injectors and the cavity showed off, causing flow separation before the cavity dump section and temporarily increasing mixing and combustion efficiency, as shown in Figure 4.7. Nevertheless, these events were not sufficiently intense to "attract" the system towards a stable configuration similar to the one observed in the experiments (high pressure and exothermicity in the cavity, with the presence of a pre-injection shock train). The afterimage of these events is still visible in the time-averaged heat release field, represented in Figure 4.5 c. It is interesting to point out that during these transient phenomena spontaneous **vertical symmetry breaking** was observed.

When the pressure increased in the ramp/secondary injection regions, the shear layer dynamics became richer; shear layer flapping modes in the $x-y$ plane emerged, with a frequency close to the first Rossiter's mode (feedback loop between shear layer dynamics and propagation of acoustic waves in the cavity - see [59]). The vertical oscillation of the core flow resulted in a sinusoidal-shaped wake (Figure 4.7 a and b) in the combustor region which, interacting with the solid walls, enhanced mixing. Due to the instantaneous breaking of symmetry, this kind of intermediate frequency mode can not be observed but by relaxing the assumption of vertical symmetry. However, due to the quasi-harmonic nature of these oscillations, symmetry is recovered after time-averaging, as Figure 4.5 shows. The interaction between acoustic phenomena and supersonic, turbulent combustion in scramjet engines is not completely well understood; however, according to some authors, understanding the key coupling features of these phenomena could lead to steadier and more controllable combustion, improving the operability of the current systems and helping in the design of better facilities and experiments.

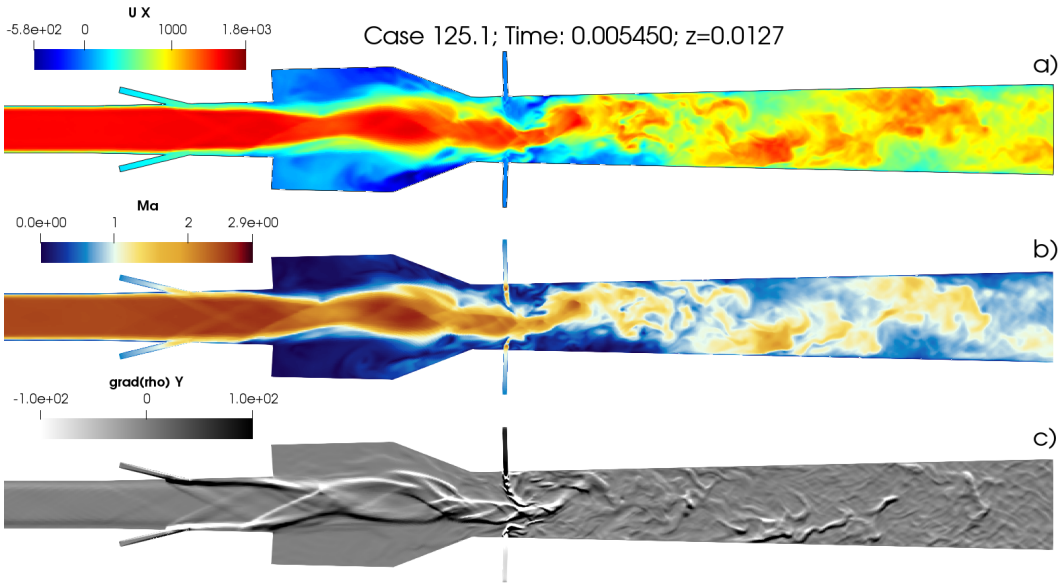

Fig. 4.7 Snapshot showing the breaking of symmetry observed during the simulation (notice the sinusoidal trace in the wake), along with the flow separation upstream of the cavity dump section. These events enhanced combustion and increased the integrated heat release level; however, the cavity backpressure was not sufficient to trigger the experimentally observed pre-injection shock train, i.e. one of the flow features of the dual-mode operation.

4.2 Pure Scramjet Operation (case #136.3)

Analogously to the the dual-mode operation case, the pure-scramjet operation case, labeled 136.3 in Table 2.1, followed the initialization procedure of Section 3.4 using the boundary conditions reported in Table 3.2.

In this case, modeling the pure-scramjet operation proved to be even more difficult to model than the dual-mode one. First of all, the case is affected by a wider discrepancy about the value of the inflow mass rate, as was reported in Section 3.3 of this work. The theoretical value of the mass flow rate - obtained using stagnation properties from Table 2.1 and the one-dimensional compressible flow relation for $\dot{m}$ - differs from the value targeted by other authors by approximately 25%. In addition to that, the elevated stagnation temperature and the narrow height of the $M_2 = 3.46$ nozzle's throat - which Storch et al. in [1] report to have experienced severe thermal distress during the experiments - also added experimental uncertainty to the values of $\dot{m}$ and M_2. Finally, as mentioned in Section 3.2, the nozzle design algorithm, when applied to this set of boundary conditions, produced a less accurate agreement

with the target value of M_2. This was due to a limit in the geometric resolution of the method of the characteristic lines for greater expansion ratios, which resulted in an excessively coarse point-wise definition of the contour near the exit section. The effect of this issue is an underestimated value of M_2; on the other hand, the core Mach number value was safely kept inside the 10% discrepancy range from the target value; this was considered inside the uncertainty range of the experiment.

Another severe difficulty that arose during the simulation of the 136.3 case was its remarkable dependence on the grid resolution. When moving from the N=48 to the N=64 grid, the solution experienced a noticeable increase in heat release and mixing. However, a complete run on the N=64 grid was not carried on, mainly because of time constraints: with the models employed, the solution could evolve by only 0.1 ms per day, using 256 cores of the SNIC Dardel HPC. This case ran for approximately **thirteen flow-through times**, which is a shorter amount of physical time compared to the 125.1 one. For this reason, only qualitative results and trends will be presented for this case, mainly in comparison with the 125.1 case.

Analogously to the dual-mode case, severe underestimation of combustion and heat release was observed throughout the simulation, as shown in Figure 4.8. The morphology of the flowfield appeared similar to the 125.1 case: no pre-injection shock train was reported, and the supersonic core kept the one-dimensional Mach number to a value greater than unity. Sharper discontinuities were observed ahead of the secondary injector, as an effect of the increased compressibility effects. The secondary injectors' jets showed a slightly different configuration. Due to the lower pressure level inside the experimental domain for the 136.3 case, the secondary fuel jets were severely underexpanded. This fact led to the presence of an underexpansion barrel, and the consequent Mach disk shock. The interaction of this flow structure with the core flow is supposed to influence mixing and combustion in the combustor area.

A curious fact emerged during the post-processing of the results of the pure-scramjet simulation. Even though the heat release was tremendously underestimated, Figure 4.9 d shows regions of premixed combustion in the combustor region, contrarily to previous results from Saghafian who proved that combustion mainly occurred in non-premixed regime at a moderate Damköhler number (about 67 % of total exothermicity). The presence of Ω-shaped structures in the secondary injectors wake - well visible in the CO field, Figure 4.9 a - may be responsible for this phenomenon.

The interface between the boundary layer instability and the core flow is characterized by a nearly-stoichiometric mixture fraction and high values of $\widetilde{\chi}$. Heat release is localized near this interface and a thick layer of hot gas forms in the wall proximity. In a real-world environment, this phenomenon is not the only contributor to mixing and combustion, and the fact that it was here observed in a fairly isolated way needs to be considered when pondering the reliability of these results. However, we can conclude that, due to the paramount role of wall-fluid interactions in mixing, an adequate wall model and near-wall mesh resolution could make the difference in this context.

In their article about cavity-based flame holding [59] Barnes and Segal report how experiments suggest a decoupling of shear layer dynamics and cavity acoustics as compressibility effects become more pronounced (i.e. the Mach number increases). Unalmis et al. [60] in their article explain how the disparity between the acoustic impedance of the cavity-recirculating fluid and that of the core stream is an increasing function of the core Mach number:

$$\frac{Z_{core}}{Z_{cav}} = \frac{(\rho a)_{core}}{(\rho a)_{cav}} \approx \sqrt{1 + \frac{r_T(\gamma-1)}{2} M_{core}^2}$$

where r_T is the temperature recovery factor of the cavity fluid. Due to this fact, the shear-layer large-scale dynamics (the "flapping" mode observed in the 125.1 case) is now uncoupled from the propagation of acoustic disturbances in the cavity, and unsteadiness is less prone to show. This fact was confirmed in the numerical investigation: the 136.3 case did not manifest appreciable large-scale, low-frequency unsteadiness.

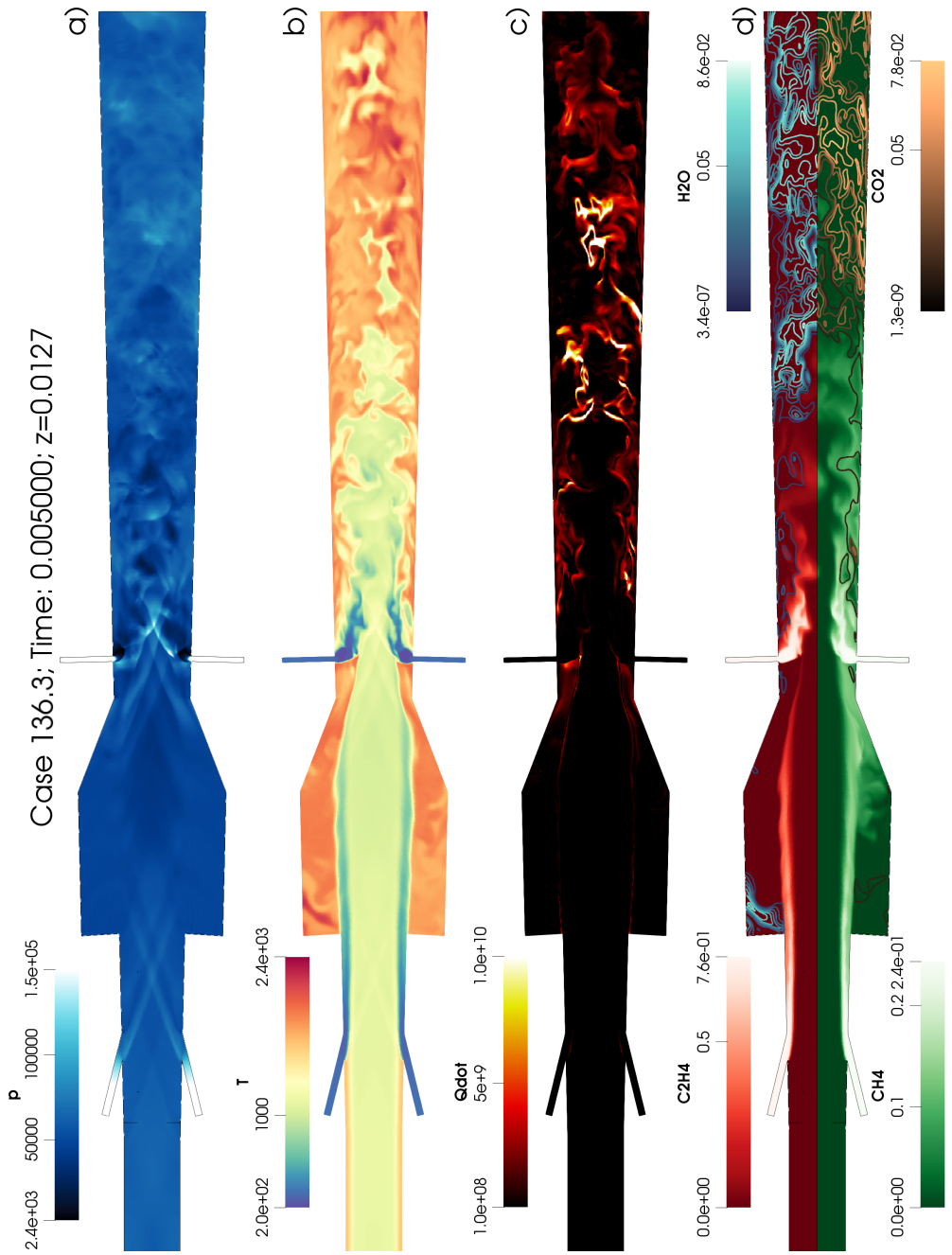

Fig. 4.8 Instantaneous **a)** pressure ([Pa]); **b)** temperature ([K]); **c)** heat release ([W/m^3]); **d)** fuels/products mass fractions ([−]). Final instant of the 136.3 case, $z = 0.0127$ m, N=48 with cavity refinement.

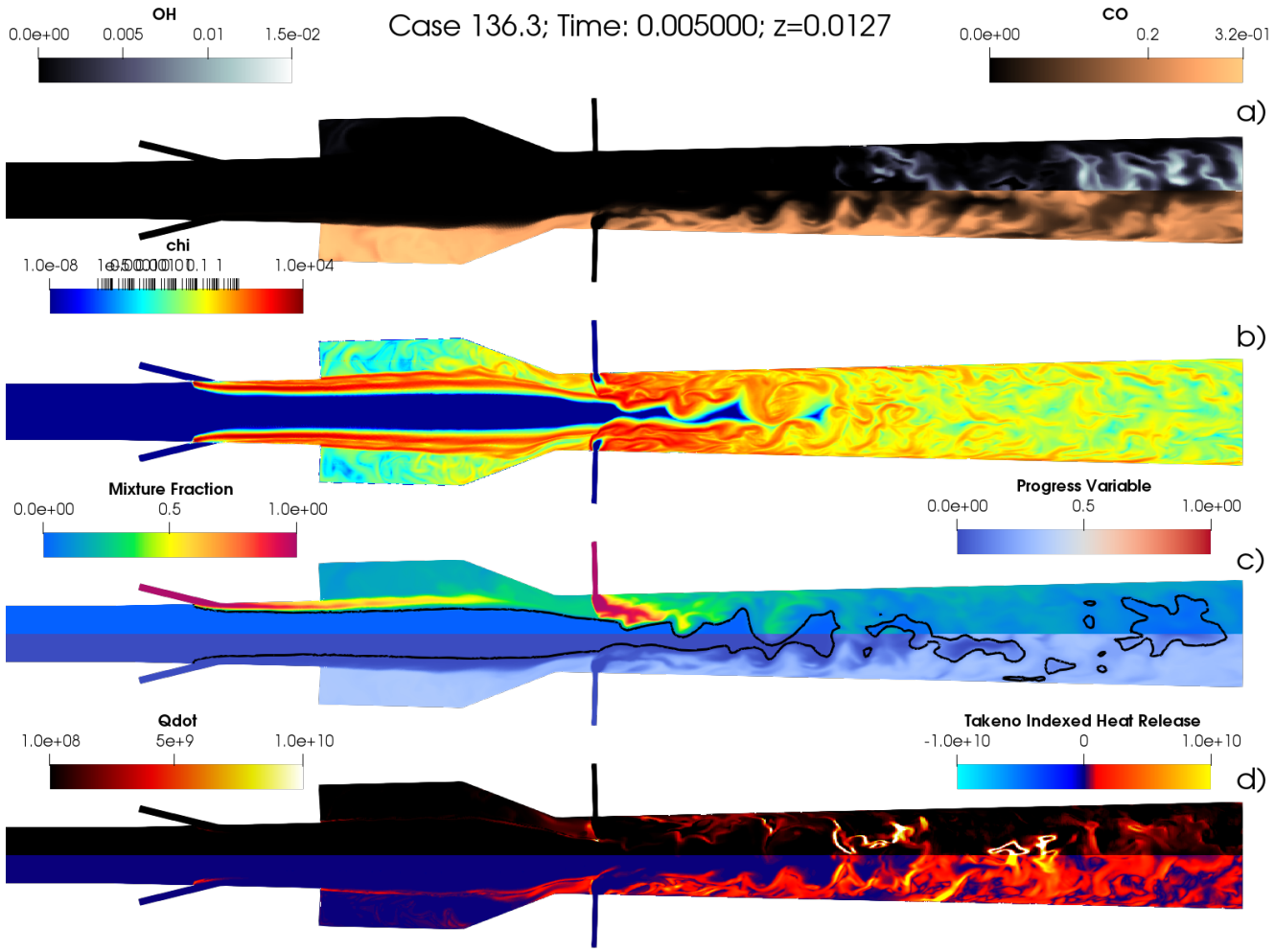

Fig. 4.9 **a)**: $\widetilde{Y}_{CO}$ and $\widetilde{Y}_{OH}$; **b)** scalar dissipation rate χ $[1/\mathrm{s}]$; **c)** mixture fraction $\widetilde{Z}$ and progress variable $\widetilde{C}$, $[-]$, with stoichiometric contour $Z_{st} = 0.0582$ **d)** comparison between $\dot{Q}$ and Takeno indexed heat release, $[\mathrm{W/m^3}]$. Latest time-slice of the 136.3 case, $z = 0.0127\,\mathrm{m}$, N=48 with cavity refinement.

Chapter 5

Conclusions and Future Work

In this work, Large Eddy Simulations were performed, aiming at the replication of the HIFiRE Direct Connect Rig experiment conducted at the Arc-Heated Scramjet Test Facility of the NASA Langley Research Center between 2010 and 2011. As part of the HIFiRE program, the technological demonstration was intended to prove the operability and performance of a cavity-stabilized, hydrocarbon-fueled scramjet engine, focusing on combustion efficiency and stability. Different operating modes were analyzed by changing the inflow conditions and using different wind tunnel nozzles in direct connection with the test rig.

In this work, the modeling approach employed wall-modeled LES of reacting, turbulent flows using the density-based, central difference OpenFOAM solver `rhoCentralTurbReactingFoam`, provided by the supervisor. Chemical reactions were incorporated using in-run calculated reaction rates based on the modified Arrhenius closure of the skeletal Z66 reaction mechanism. The hexahedral computational grid was built using the `blockMesh` utility by the author. The well-tested and validated modeling strategy was applied to two of the most interesting experimental configuration: the dual-mode case labeled 125.1, imitated a $M_\infty = 6.5$ flight condition while the pure scramjet case, indicated with 136.3, was representative of a high-speed $M_\infty = 8.0$ flight. The two different scenarios were previously targeted in the same experimental facility, using two different wind tunnel nozzles.

Analysis of the results showed systematic under-prediction of the pressure levels in the combustion chamber, with reduced combustion and exothermicity. For the dual-mode case, this fact translated into a completely different flowfield configuration.

Indeed, no pre-injection shock train was observed in the simulation. The pre-injection shock train is a rather complex flow feature involving boundary layer separation and shockwave reflection; this phenomenon is observed in dual-mode scramjet engines, and it allows pressure levels in the isolator region to gradually adapt to the higher cavity levels. The correlation between reduced combustion and the absence of the pre-injection shock train confirms how these two phenomena are inherently coupled.

As far as the pure scramjet mode is concerned, the disagreement between the experimental results and the simulation was even wider. As an exploratory step, the 136.3 case was tested on a refined N=64 (approximately sixteen million cells) mesh. This proved the great sensitivity of the results on mesh resolution, suggesting that the results were far from being grid-converged. The computational cost, however, was considered too high, and a complete analysis using the finer mesh was not carried on. In conclusion, the stricter mesh requirements for the 136.3 case - probably related to its higher Reynolds number and smaller mixing length scale - were the reason for the lower amount of simulated physical time.

Flowfield data from the two cases suggested that mixing occurred mainly thanks to the interaction between the core flow and the secondary injector jets, which injected 60% of the total fuel amount and had a remarkable penetration and spoiling effect on the incoming air stream. Shear layer instabilities in the cavity region and the presence of Ω-shaped near-wall instabilities in the combustor region played a role in enhancing mixing in the two cases. Interestingly, the two cases appeared to be characterized by two different combustion regimes. While the majority of combustion in the dual-mode operation turned out to occur in a non-premixed regime, the opposite was found for the scramjet operating mode, where heat release was localized in near-wall regions in correspondence to boundary layer instabilities. From this fact, it emerges how wall-modeling and near-wall grid resolution both might play a key role in the predictive capability of LES of supersonic reacting flows. Anyway, it is important to point out that due to the high levels of uncertainty in both the model and the experiment, these quantitative results need to be regarded as purely speculative.

The unsteady nature of the dual-mode operation was reflected in the simulation. A large-scale longitudinal unsteadiness was observed, which also led to the spontaneous breaking of vertical symmetry of the cavity flow. During the simulation, “flapping” of the shear layer with a frequency close to the first Rossiter mode was observed.

These modes are caused by the positive feedback between shear layer dynamics and the propagation of acoustic disturbances in the cavity. The observation of these rich dynamics was made possible thanks to the fact that vertical symmetry was not assumed when building the computational domain; the quasi-harmonic nature of these modes, however, is reflected in the almost-ideal symmetry of the time-averaged fields. The propagation and reflection of acoustic waves in scramjet engines are supposed to play a non-negligible role, contributing to both hydrodynamic-acoustic and heat release-acoustic coupling phenomena.

Further investigation of the model will be carried on to debunk the cause of the bad agreement in terms of pressure distributions. As reported by several authors, the HDCR experiment has been affected by wide degrees of experimental uncertainty. Huan et al. in [61] performed a global sensitivity analysis on the HDCR experiments, showing great sensitivity to some computational and experimental parameters. This, in addition to the incredibly complex physics of supersonic combustion experiments, suggests that future modeling efforts would benefit from the application of an uncertainty quantification framework.

In future works, the true wind tunnel nozzles geometry will hopefully be introduced. This will drastically reduce the uncertainty about the boundary conditions, narrowing down the parameters space.

Once all the aforementioned aspects are figured out, the effort will move towards increasing the quality of the results by experimenting with different near-wall, subgrid-scale, and turbulence-chemistry interaction models. The exploration of different reaction mechanisms would probably produce interesting results as well.

After having obtained a decent agreement with the experimental results and grid convergence on the reduced computational domain, secondary effects such as the presence of the sidewalls, jet-jet spanwise interaction and thermal radiation will be, if possible, studied. The model could then be extensively post-processed to get quantitative information. One particularly interesting application of the massive amount of data produced by high-resolution simulations is the possibility of "condensing" all the useful information in reduced-order models (ROM) for different kinds of systems, using the appropriate mathematical tools. Efforts in this direction will probably be part of future work on this and other models.

References

[1] Andrea Storch, Michael Bynum, Jiwen Liu, and Mark Gruber. Combustor operability and performance verification for HIFiRE flight 2. In *17th AIAA International Space Planes and Hypersonic Systems and Technologies Conference*, page 2249, 2011.

[2] John J. Bertin and Russell M. Cummings. Fifty years of hypersonics: where we've been, where we're going. *Progress in Aerospace Sciences*, 39(6):511–536, 2003.

[3] Earl H. Andrews and Ernest A. Mackley. Nasa's hypersonic research engine project: A review. 1994.

[4] NASA's Hypersonic Research Engine (HRE) Project: A review. https://ntrs.nasa.gov/citations/19950006447. Accessed: 05-04-2022.

[5] Corin Segal. *The Scramjet Engine: Processes and Characteristics*. Cambridge Aerospace Series. Cambridge University Press, 2009.

[6] John D. Jr Anderson. *Modern compressible flow : with historical perspective*. McGraw-Hill series in aeronautical and aerospace engineering. McGraw-Hill, Boston, 3rd rev. ed edition, 2004.

[7] John D. Jr Anderson. *Hypersonic and High-Temperature Gas Dynamics; Second Edition*. American Institute of Aeronautics and Astronautics, 2000.

[8] ESA Technology Readiness Levels (TRL). https://www.esa.int/Enabling_Support/Space_Engineering_Technology/Shaping_the_Future/Technology_Readiness_Levels_TRL. Accessed: 03-04-2022.

[9] Nicole Viola, Roberta Fusaro, Bayindir Saracoglu, Christophe Schram, Grewe Volker, Jan Martinez, Marco Marini, Santiago Hernandez, Karel Lammers, Axel Vincent-Randonnier, Didier Hauglustaine, Bernd Liebhardt, Florian Linke, and Christer Fureby. Main challenges and goals of the H2020 STRATOFLY Project. *Aerotecnica Missili & Spazio*, 100, 05 2021.

[10] Daniel Daley William Heiser, David Pratt and Unmeel Mehta. *Hypersonic Airbreathing Propulsion*. AIAA Education Series, 2 edition, 1994.

[11] Laurie Marshall, Catherine Bahm, Griffin Corpening, and Robert Sherrill. *Overview With Results and Lessons Learned of the X-43A Mach 10 Flight*. 2005.

[12] Piotr Wolański. Detonative propulsion. *Proceedings of the Combustion Institute*, 34(1):125–158, 2013.

[13] Thierry Poinsot and Denis Veynante. *Theoretical and Numerical Combustion*. Edwards, 2005.

[14] `janafThermoI.H` - openfoam implementation. https://www.openfoam.com/documentation/guides/latest/api/janafThermoI_8H_source.html. Accessed: 23-04-2022.

[15] Guido Buresti. A note on Stokes' hypothesis. *Acta Mechanica*, 226:3555–3559, 2015.

[16] H.K. Versteeg and W. Malalasekera. *An Introduction to Computational Fluid Dynamics*. Pearson, 2007.

[17] J. O. Hirschfelder, Charles F. Curtiss, and R. Byron Bird. *Molecular Theory Of Gases And Liquids*. Wiley, 1954.

[18] `sutherlandTransportI.H` - OpenFOAM implementation. https://cpp.openfoam.org/v7/sutherlandTransportI_8H_source.html. Accessed: 26-04-2022.

[19] CEA: Chemical Equilibrium with Applications. https://cearun.grc.nasa.gov/. Accessed: 28-04-2022.

[20] S.M. de Bruyn Kops, J.J. Riley, G. Kosaly, and A.W. Cook. Investigation of modeling for non-premixed turbulent combustion. *Flow, Turbulence and combustion*, 60(1):105–122, 1998.

[21] Amirreza Saghafian, Lee Shunn, David A. Philips, and Frank Ham. Large eddy simulations of the HIFiRE scramjet using a compressible flamelet/progress variable approach. *Proceedings of the Combustion Institute*, 35(2):2163–2172, 2015.

[22] Stiff systems - web resource. http://www.scholarpedia.org/article/Stiff_systems. Accessed: 29-04-2022.

[23] Ignition Delay Time - web resource. https://petersengroup.tamu.edu/research-2/gas-dynamics-chemical-kinetics/shock-tube-kinetics/idt/. Accessed: 29-04-2022.

[24] Philippe Dagaut. Chapter 8 - experiments for kinetic mechanism assessment. In Tiziano Faravelli, Flavio Manenti, and Eliseo Ranzi, editors, *Mathematical Modelling of Gas-Phase Complex Reaction Systems: Pyrolysis and Combustion*, volume 45 of *Computer Aided Chemical Engineering*, pages 445–471. Elsevier, 2019.

[25] S. B. Pope. *Turbulent Flows*. Cambridge University Press, 2000.

[26] Pierre Sagaut. *Large Eddy Simulation for Incompressible Flows: an Introduction*. Springer Science & Business Media, 2006.

[27] Charles R. Doering and J. D. Gibbon. *Applied Analysis of the Navier-Stokes Equations*. Cambridge Texts in Applied Mathematics. Cambridge University Press, 1995.

[28] M. Carbone and A. D. Bragg. Is vortex stretching the main cause of the turbulent energy cascade? *Journal of Fluid Mechanics*, 883:R2, 2020.

[29] `kEqn.H` - OpenFOAM implementation. https://caefn.com/openfoam/keqn-sgs-model. Accessed: 03-05-2022.

[30] R.A. Humble, F. Scarano, B.W. Van Oudheusden, and M. Tuinstra. PIV measurements of a shock wave/turbulent boundary layer interaction. In *Thirteenth Intl Symp. on Laser Techniques to Fluid Mechanics, Lisbon, Portugal, Paper*, volume 14, 2006.

[31] `nutkWallFunction.H` - OpenFOAM implementation. https://www.openfoam.com/documentation/guides/latest/doc/guide-bcs-wall-turbulence-nutkWallFunction.html. Accessed: 04-05-2022.

[32] Christopher Greenshields and Henry Weller. *Notes on Computational Fluid Dynamics: General Principles*. CFD Direct Ltd, Reading, UK, 2022. https://doc.cfd.direct/notes/cfd-general-principles/.

[33] Alexander Kurganov and Eitan Tadmor. New high-resolution central schemes for nonlinear conservation laws and convection-diffusion equations. *Journal of Computational Physics*, 160(1):241–282, 2000.

[34] `rhoCentralFoam.C` solver - source code. https://develop.openfoam.com/Development/openfoam/-/blob/master/applications/solvers/compressible/rhoCentralFoam/rhoCentralFoam.C. Accessed: 11-05-2022.

[35] Jason M. Reese, Luca Gasparini, and Henry G. et al Weller. Implementation of semi-discrete, non-staggered central schemes in a colocated, polyhedral, finite volume framework, for high-speed viscous flows. *International Journal for Numerical Methods in Fluids*, 2009.

[36] Bram Van Leer. Towards the ultimate conservative difference scheme. V. A second-order sequel to Godunov's method. *Journal of computational Physics*, 32(1):101–136, 1979.

[37] Divergence schemes in OpenFOAM. https://www.openfoam.com/documentation/guides/latest/doc/guide-schemes-divergence.html. Accessed: 14-05-2022.

[38] `limitedLinear.H` - OpenFOAM implementation. https://develop.openfoam.com/Development/openfoam/blob/OpenFOAM-v2112/src/finiteVolume/interpolation/surfaceInterpolation/limitedSchemes/limitedLinear/limitedLinear.H. Accessed: 14-05-2022.

[39] `centralCourant.H` - OpenFOAM implementation. https://www.openfoam.com/documentation/guides/latest/api/centralCourantNo_8H_source.html. Accessed: 16-05-2022.

[40] `YEqn.H` - reactingFoam implementation. https://www.openfoam.com/documentation/guides/latest/api/combustion_2reactingFoam_2YEqn_8H_source.html. Accessed: 16-05-2022.

[41] Niklas Zettervall, Christer Fureby, and Elna J. K. Nilsson. Small Skeletal Kinetic Reaction Mechanism for Ethylene–Air Combustion. *Energy & Fuels*, 31(12):14138–14149, 2017.

[42] Kevin Bowcutt and Alan et al. Paull. HIFiRE: an international collaboration to advance the science and technology of hypersonic flight. ICAS, 2012. http://www.icas.org/ICAS_ARCHIVE/ICAS2012/PAPERS/998.PDF.

[43] Kevin Jackson, Mark Gruber, and Todd Barhorst. The HIFiRE flight 2 experiment: an overview and status update. In *45th AIAA/ASME/SAE/ASEE Joint Propulsion Conference & Exhibit*, page 5029, 2009.

[44] Guilhem Lacaze, Zachary Vane, and Joseph C. Oefelein. Large Eddy Simulation of the HIFiRE Direct Connect Rig scramjet combustor. In *55th AIAA Aerospace Sciences Meeting*, page 0142, 2017.

[45] Mark R. Gruber, Kevin Jackson, and Jiwen Liu. Hydrocarbon-Fueled Scramjet Combustor Flowpath Development for Mach 6-8 HIFire Flight Experiments (Preprint). Technical report, Air Force Research Lab Wright-Patterson AFB OH Propulsion Directorate, 2008.

[46] Neal Hass, Karen Cabell, Andrea Storch, and Mark Gruber. HIFiRE direct-connect rig (HDCR) phase I scramjet test results from the NASA Langley arc-heated scramjet test facility. In *17th AIAA International Space Planes and Hypersonic Systems and Technologies Conference*, page 2248, 2011.

[47] Mark Gruber, Kevin Jackson, Dean Eklund, Todd Barhorst, Neal Hass, Andrea Storch, and Jiwen Liu. Instrumentation and performance analysis plans for the HIFiRE flight 2 experiment. In *45th AIAA/ASME/SAE/ASEE Joint Propulsion Conference & Exhibit*, page 5032, 2009.

[48] R. Guy, R. Rogers, Richard Puster, Kenneth Rock, and Glenn Diskin. *The NASA Langley Scramjet Test Complex*.

[49] Gerald L Pellett, Sarah N Vaden, and Lloyd G Wilson. Gaseous surrogate hydrocarbons for a HIFiRE scramjet that mimic opposed jet extinction limits for cracked JP fuels. In *55th JANNAF Propulsion Meeting*, 2008.

[50] Ivan Bermejo-Moreno, J. Larsson, Julien Bodart, and Ronan Vicquelin. Wall-Modeled Large-Eddy Simulations of the HIFiRE-2 Scramjet. *HAL Open Science*, 01 2013.

[51] Robert Yentsch and Datta Gaitonde. Exploratory simulations of the HIFiRE 2 scramjet flowpath. In *48th AIAA/ASME/SAE/ASEE Joint Propulsion Conference & Exhibit*, page 3772, 2012.

[52] Cory Dodson. Supersonic nozzle design tool, 2022. Available at https://se.mathworks.com/matlabcentral/fileexchange/43212-supersonic-nozzle-design-tool. Retrieved May 22,2022.

[53] Ames Research Staff. Equations, tables and charts for compressible flow. 1953. Available online at https://www.grc.nasa.gov/www/BGH/Images/naca1135.pdf.

[54] C. Fureby, E. Fedina, and J. Tegnér. A computational study of supersonic combustion behind a wedge-shaped flameholder. *Shock Waves*, 24(1):41–50, 2014.

[55] Niklas Zettervall and Christer Fureby. A computational study of ramjet, scramjet and dual-mode ramjet combustion in combustor with a cavity flameholder. In *2018 AIAA Aerospace Sciences Meeting*, page 1146, 2018.

[56] C. Fureby, M. Chapuis, E. Fedina, and Sebastian Karl. CFD analysis of the HyShot II scramjet combustor. *Proceedings of the Combustion Institute*, 33(2):2399–2405, 2011.

[57] A. Vincent-Randonnier, V. Sabelnikov, A. Ristori, N. Zettervall, and C. Fureby. An experimental and computational study of hydrogen–air combustion in the LAPCAT II supersonic combustor. *Proceedings of the combustion institute*, 37(3):3703–3711, 2019.

[58] Amirreza Saghafian, Vincent E. Terrapon, and Heinz Pitsch. An efficient flamelet-based combustion model for compressible flows. *Combustion and Flame*, 162(3):652–667, 2015.

[59] Frank W. Barnes and Corin Segal. Cavity-based flameholding for chemically-reacting supersonic flows. *Progress in Aerospace Sciences*, 76:24–41, 2015.

[60] O. Haldun Unalmis, N.T. Clemens, and D.S. Dolling. Cavity oscillation mechanisms in high-speed flows. *AIAA journal*, 42(10):2035–2041, 2004.

[61] Xun Huan, Cosmin Safta, Khachik Sargsyan, Gianluca Geraci, Michael S Eldred, Zachary P Vane, Guilhem Lacaze, Joseph C Oefelein, and Habib N Najm. Global sensitivity analysis and estimation of model error, toward uncertainty quantification in scramjet computations. *AIAA Journal*, 56(3):1170–1184, 2018.